http://researchcommons.waikato.ac.nz/

Research Commons at the University of Waikato

Copyright Statement:

The digital copy of this thesis is protected by the Copyright Act 1994 (New Zealand).

The thesis may be consulted by you, provided you comply with the provisions of the Act and the following conditions of use:

- Any use you make of these documents or images must be for research or private study purposes only, and you may not make them available to any other person.
- Authors control the copyright of their thesis. You will recognise the author's right to be identified as the author of the thesis, and due acknowledgement will be made to the author where appropriate.
- You will obtain the author's permission before publishing any material from the thesis.

The interaction of buoyant river plumes with vegetation and consequences for sediment transport and deposition in coastal regions

A thesis

submitted in fulfilment

of the requirements for the Degree

of

Doctor of Philosophy in Earth Sciences

at

The University of Waikato

by

Hemanth V. S. S. R. Vundavilli

THE UNIVERSITY OF
WAIKATO
Te Whare Wānanga o Waikato

2023

Abstract

Mangrove forests are one of the most prominent vegetated coastal habits in tropical and subtropical areas. These wetland ecosystems typically inhabit estuaries and tidally influenced river banks. The presence of trees helps to protect coastal regions through the dissipation of tidal currents and wave energy, forming an essential barrier against coastal erosion. River plumes are the primary mechanism of sediment delivery to these vegetated coastlines. As the buoyant freshwater merges with saline ocean waters, horizontal advection of the freshwater establishes the shape of the river plume and influences the distribution of sediments along the coast. In this thesis, I investigate the principal dynamics associated with the interaction of buoyant river plumes with vegetation. In particular, we investigate the interplay between mangrove vegetation, hydrodynamics, and sediment dynamics, specifically: (1) the principal drivers of sediment deposition within a mangrove-lined river delta, (2) the influence of river forcing and winds on the sediment transport, and (3) sediment dynamics of two adjacent and interacting coastal river plumes.

Understanding the hydro-morphodynamics of a river plume in a mangrove environment

We developed a 3-D idealized Delft3D morphological model to explore the effects of vegetation on the river plumes and associated sediment transport patterns. Using an idealized model based on the Firth of Thames (FoT) mangrove forest located on the North Island of Aotearoa-New Zealand, we observed that, while sediment deposition occurred in the forest and tidal flats region of the model domain, the fringe region (between the vegetation and mudflat) ex-

perienced erosion. Compared to the eastern side, sediment deposition in the western side of the model domain was more prominent owing to the influence of Coriolis (Southern hemisphere). By examining the momentum balances on the surface and bottom layers in different regions of the river plume, we found that the principal balance between the bottom shear stress (enhanced by the presence of vegetation) and baroclinic pressure gradient largely controlled the sediment deposition in the riverine sections of the domain. Additionally, we found that vertical advection and diffusion during flood tide enhanced erosion in the fringe region of the mangrove forest. The advection of suspended sediment into the forest was controlled by factors including longer duration of high water slack at the forest fringe region, pressure gradients, and inertial acceleration. In the near-field region (close to the river mouth) of the river plume, during ebb tide, the barotropic and baroclinic pressure gradients coupled with Coriolis accelerations deliver sediments into the forest and mudflat regions. In the mid-field regions of the river plume, the magnitude of changes in the bed elevation was smaller due to larger Coriolis acceleration which arrested the spreading of the river plume. Furthermore, the far-field region (away from the river mouth) of the river plume experienced erosion due to more substantial tidal influence. Conversely, in the shallow forested regions, reduced movement of sediment in the offshore direction leads to an overall flood dominance.

Linking sediment transport within river plumes to varying river flows and winds

Subsequent modeling experiments were carried out to investigate how the forcing factors of riverine discharge and wind velocities influence sediment transport within an idealized moderate-sized freshwater river plume. We assessed total sediment transport along with the relative contributions of riverine and bed-sourced sediment into a mangrove forest. Instantaneous and tidally averaged sediment fluxes were evaluated to investigate the critical linkages between the riverine flows, tidal influence, and winds in the presence of vegetation. In

the near-field region of the river plume, riverine and bed-sourced sediment were dominant and found to be directed into the forest, indicative of an accretionary environment. In the mid- and far-field regions of the river plume, bed-sourced sediment was found to be the dominant contributor to total sediment transport and was directed out of the forest, indicative of sediment erosion. While the mass loads (directed into the mangrove forest) increased with an increase in riverine discharge, mass loads were relatively similar for large flow events. The river sediment delivered into the mangrove-forested regions was found to push into and through the forest front for large river discharges. The presence of $5\,\mathrm{m.s^{-1}}$ wind velocities could alter the sediment deposition patterns in the mid- and far-field regions of the river plume. Despite the significant river momentum, strong winds ($10\,\mathrm{m.s^{-1}}$) were also able to alter the sediment transport in the near-field region of the river plume. Moreover, results showed that in the far-field region of the river plume, strong winds combined with the effects of riverine discharge, Coriolis, and bed-shear stress affected the overall mass movement of sediment. In the case of easterly winds, a combination of tidal effects and wind stress controlled the sediment deposition into the forest. In the case of westerly winds, as the plume was pushed away from the forest, tidal effects controlled the total sediment transport.

Understanding the effects of coalescing buoyant river plumes on sediment transport

We investigated how the interaction between plumes from two mangrove-lined rivers in close proximity affected coastal sediment transport patterns. In particular, I examined the links between the river plume coalescence and the trapping of sediment by mangroves, using an idealized 3-dimensional numerical. Sediment fluxes and relative contributions of riverine- and bed-sourced sediments were quantified along the western, central (located between the rivers), and eastern mangrove forests. The two river plumes coalesced into a single river plume that flowed along the edge of the central mangrove forest. As the

river plumes were deflected to the left by Coriolis (Southern hemisphere), the total sediment fluxes were largest for the central and the western forest, with only modest sediment deposition along the eastern mangrove forest. Also, modeled transport fluxes along the central mangrove forest were the largest close to the rivers, consistent with the satellite imagery of the FoT field site. Flow variations through either river resulted in changes to the sediment transport patterns into the mangrove forests. In particular, an increase in flow discharge through the western river resulted in reduced contributions of the eastern river towards the total sediment transport fluxes. Conversely, an increase in flow discharge through the eastern river inhibited the contribution of western river-associated sediment towards the total sediment transport flux through the central, eastern, and western mangrove forests. Furthermore, this study revealed that $5\,\mathrm{m.s^{-1}}$ wind velocities altered the expansion, coalescence, and overall sediment transport fluxes of the river plumes. The total sediment fluxes through the central and western mangrove forests were greatest for easterly winds. However, the total transport into the eastern mangrove forest was largest for the southerly winds, as the bulge of the eastern river plume was pushed into mangrove forests.

These modeling experiments help elucidate the interaction of river plumes with mangrove vegetation. The work presented in this thesis highlights the complex non-linear interactions of hydro-morphodynamics, sediment transport, the effects of river flows and winds within mangrove environments, and the fate of riverine sediments in the bay of the Firth of Thames. Finally, the results presented here provide insights into the sediment trapping capabilities of mangroves under variable conditions and thus may help to predict their ability to function as a coastal defense mechanism under future sea-level rise and sediment supply scenarios.

Acknowledgements

I owe the completion of this thesis to many. I am very fortunate to have worked under the chief supervision of Associate Professor Julia Mullarney, whose unwavering support, invaluable mentoring, enormous patience, and giving me intellectual freedom have made my doctoral journey a rewarding experience. I also want to extend my sincere thanks to Dr. Iain MacDonald from NIWA, whose valuable inputs throughout this project and occasional banter about my football club made this journey a fun and excellent learning experience. An enormous thanks also go to Prof. Karin Bryan for her fantastic support throughout this project. Working and learning from all of you helped me grow professionally and personally, for which I will forever be grateful.

I am also thankful to funding agencies, the donors of the American Chemical Society Petroleum Research Fund (Grant number: PRF #56786-ND8), and the Broad Memorial Fund award for the support of this research.

While this thesis has my name on the cover, it would be a sheer injustice not to acknowledge the unsung heroes. The road to a doctorate is usually an arduous and lonely journey, further worsening due to the repercussions of COVID-19 in my personal and professional life. However, I could weather the stormy days due to the helpful support and encouragement from my incredible family. My mom and dad, who have been the rock of my life and the most incredible twin brother one can have, who was always around for lively conversations pertinent to science and spirituality, are one of the primary reasons

this thesis came to a completion.

I would also like to thank all the past and present members of the Coastal Marine Group, particularly Dr. Ben Norris, Dr. Ben Stewart, Zhanchao, Vinay, Shahab, Amin, Bérengère, and Peter, for great chats and some great memories.

Last but not least, having made New Zealand my home away from home over the past few years, I have to thank my closest friends, especially David Tibshraeny, Rajan Munisami, Arjun Kodavoor, Dhiraj Shetty, and Shashank Yathindranath, whose support during my lowest points and the best company to laugh during the best of times, have made this journey an amazing one.

Dedication

To my parents, Rohini Sundari and Srinivas Vundavilli, and my twin brother, Haswanth Vundavilli.

Table of Contents

List of Figures

List of Tables

Chapter 1

Introduction

Waihou river meeting mangrove vegetation in the Firth of Thames (Source: New Zealand Geographic)

1.1 Background and introduction

Freshwater systems such as rivers are interdependent with the landscapes they are a part of and play an essential role in shaping the development of human civilizations (Everard and Powell, 2002). Over the globe, approximately one-third of land precipitation is transported into the ocean via rivers (Trenberth et al., 2007). Due to high nutrient input, rivers form biologically productive systems by shaping the adjacent shelves into essential fishing grounds. However, river systems worldwide are compromised due to external pressures such as the human population and the patterns of human influence on the climate (Walling, 2006). As regions of river interactions with oceans are highly dynamic and involve complex mixing and transport processes, understanding these interactions is pivotal for maintaining coastal ecosystems and their resources. The fundamental driver of continental sedimentation is the transport of sediments from rivers to the ocean, which has consequences for land use planning, carbon burial, and unraveling global climate change (Nittrouer, 1999; Paola, 2000). River mouths form a critical source-to-sink transfer zone where fluvial sediment is transported offshore. Previous studies such as Bates (1953) and Rajaratnam (1976) have found that the boundary conditions at a river's mouth significantly impact the fluid dynamics and sedimentation patterns of river plumes far offshore. Frontal zones trap sediment in estuaries and on the inner shelf, leading to significantly larger sediment concentrations relative to the riverine source. At large concentrations, the sediment density anomaly aids in vertical flow stability and, in many cases, improves the capacity of the frontal zone to capture particles (Geyer et al., 2001). It has also been proposed that, as rivers remain in a perpetual state of morphodynamic adjustment (Chatanantavet and Lamb, 2014), it is essential to consider river plumes under various flow outputs to understand the fluvio-deltaic morphodynamics.

Aquatic vegetation often thrives at the land-sea interface, forming essential habitats for fish and animal species and contributing to biodiversity. One such vegetative environment is salt-tolerant mangroves, which have a wide range of uses for humans, such as providing raw building materials, sources of medicine, and food for local communities (Saenger, 2002). Furthermore, by creating a buffer zone along coastlines, mangroves also serve as filters to terrestrial runoff by reducing the amount of material and chemical waste that would otherwise end up in the coastal ocean (Temmerman et al., 2013), stabilizing sediments to prevent erosion (Mazda et al., 2005), and protecting communities from coastal hazards (Lin and Dushoff, 2004).

Mangrove forests are mainly found in lower latitude temperate, tropical, and subtropical regions of the world (between 30°N and 30°S) limited by a sea-water isotherm of 20°C. Across the world, mangrove forests account for 0.7% of tropical forests in the area ($\sim$ 1.3 x 10^5 km^2 in 118 countries), with the largest extents in Asia covering nearly 42% (Giri et al., 2011). Studies such as Richards and Friess (2016) previously used high-resolution datasets to provide information on the mangrove loss in South East Asia, attributing the decline to anthropogenic land conversion and aquaculture. It is thought that nearly 35% of the world's mangrove coverage was lost between 1980 - 2000 (Valiela et al., 2001). Mangrove forest degradation is primarily a result of coastal regions being converted to agriculture, aquaculture, and urban expansion (Alongi, 2002; Giri et al., 2008). As a result, mangrove vegetation worldwide has been in a steep decline (1% - 2% per year) owing to human pressures such as urbanization and industrial developments along the coastal regions (Duke et al., 2007). Climate change directly affects mangroves' structure and function by impacting the physical, chemical, biological, and geomorphological features of the ecosystem (Gilman et al., 2008).

A direct consequence of climate change on mangrove ecosystems is the ris-

ing sea levels. Within mangrove environments, the relative sea level change is more influential than the absolute sea-level rise (Woodroffe, 1990). Mangrove forest development and zonation are influenced by long-term changes in net surface elevation caused by the interplay of surface and sub-surface processes (Fagherazzi et al., 2017). Subsurface processes, such as mangrove root development and decomposition, can be the primary regulator of mangrove sediment surface elevation (Saintilan et al., 2022) and, by extension, local-scale changes in relative sea-level rise (SLR) within a given mangrove site in specific areas and situations. The current and projected SLR rates are likely to significantly influence mangrove forests, raising concerns that wetlands are prone to drowning and coastal squeeze (Phan et al., 2015). These long-term processes influence the short-term processes by changing the bio-geomorphic landscape, which in turn influences the inundation period, sediment supply, and sediment transport capability of mangroves (McIvor et al., 2013). The morphology in mangrove environments is controlled by non-linear feedbacks between the hydrodynamics and sediment transport, with sediment transport and deposition patterns (Mullarney and Henderson, 2018). The study of these non-linear feedbacks between tides, vegetation, river flow, and sediment supply, along with the morphology, forms the central theme of this thesis.

One of the principal governing mechanisms through which the shape and extent of a river plume are the river discharge and the geometry of the river mouth (Hetland, 2010). Discharge in a river system can vary by at least one order of magnitude seasonally (Allison et al., 2014). For instance, in the case of small plume systems such as the River Teign (located in England, average annual discharge of nearly $5\,\mathrm{m}^3.\mathrm{s}^{-1}$), the plume, which extends a few hundred meters, disappears after each ebb tide and forms a new one after each tide (Pritchard and Huntley, 2006). However, large river systems such as the Columbia river (Hickey et al., 1998) form a buoyant layer near the river mouth, creating a spatially and temporally complex region and a strong

gravity current propagating seaward during each ebb tide. In the case of very large river plume systems such as the Mississippi river, which has an annual average discharge of nearly 30,000 $m^3.s^{-1}$, the freshwater discharge forms a persistent plume near the river mouth with very little influence by the tides (Zhang et al., 2012).

1.2 River plume dynamics

A typical river plume system can be classified into three distinct dynamic regions as shown in Figure 1.1: (1) Near-field region, (2) Mid-field region, and (3) Far-field region.

Near-field region When river water enters a coastal water body, a plume is formed with dynamics controlled by the strong offshore momentum at the river mouth. This jet-like region, termed the near-field region of the plume, is a region of intense mixing and significant changes in densities caused by the horizontal barotropic and baroclinic pressure gradients (Jones et al., 2007). The presence of barotropic and baroclinic pressure gradients, interfacial stresses, and accelerations dominate momentum in the near-field region of the river plume, with minimal to the modest influence of wind stress, Earth's rotation, and ambient shelf conditions (McCabe et al., 2009). With the presence of high energy in the near-field zone, the shear-mixing of the region is enhanced and leads to entrainment of the high-density ambient waters into the buoyant river plume. The lateral spreading of the river plume is sensitive to the tidal discharge and is often characterized by the outflow Froude number (Horner-Devine et al., 2009; Kilcher et al., 2012).

Mid-field region The plume volume increases as it spreads due to the entrainment of the ambient water. The resulting deceleration of the plume leads to sub-critical conditions, and the plume forms a re-circulating bulge (due to Earth's rotation). This bulge region, termed the mid-field region, forms the

transition zone between the near-field and far-field region of the river plume and is highly sensitive to external factors such as the wind. The presence of Coriolis renders a two-part structure in the mid-field region of the river plume, wherein the river plume forms an anti-cyclonic bulge near the river mouth and a coastal current propagating downstream. Notable examples of such a bulge circulation include the Pearl River plume (e.g Chen et al., 2017), Columbia River plume (e.g Kilcher and Nash, 2010), and Mississippi River plumes (e.g. Schiller et al., 2011). Within the mid-field region, the effect of wind becomes important in response to longer time-scale Ekman dynamics (Horner-Devine, 2009).

Far-field region Farther in the downstream direction, the river plume enters the far-field region, in which the plume transport is primarily alongshore (Horner-Devine et al., 2015), and the dynamics become controlled by external factors such as winds (e.g. Choi and Wilkin, 2007), tides (e.g. Wu et al., 2011), Coriolis (e.g. Kasai et al., 2000), and slope of the shelf (e.g. Avicola and Huq, 2002).

Multiple previous studies have explored the influence of external forces on river plume dynamics. For example, Chao and Boicourt (1986) investigated the effects of bathymetry and wind on plume circulation. Using a model consisting of an estuary and shelf, they found that the response of a plume highly depends on the wind direction, in that upwelling-favorable winds parallel to the coast would result in plume transport towards the direction of the Ekman drift. Alternatively, a downwelling favorable wind would enhance the plume transport in the alongshore direction due to the build-up of a downwind coastal jet. Mixing within the mid- and far-field regions of the river plume is primarily driven by enhanced mixing of plume waters from the surface to depth due to external effects such as winds. Using dye release experiments in the far-field region, Houghton et al. (2004) showed that wind stress, while acting over

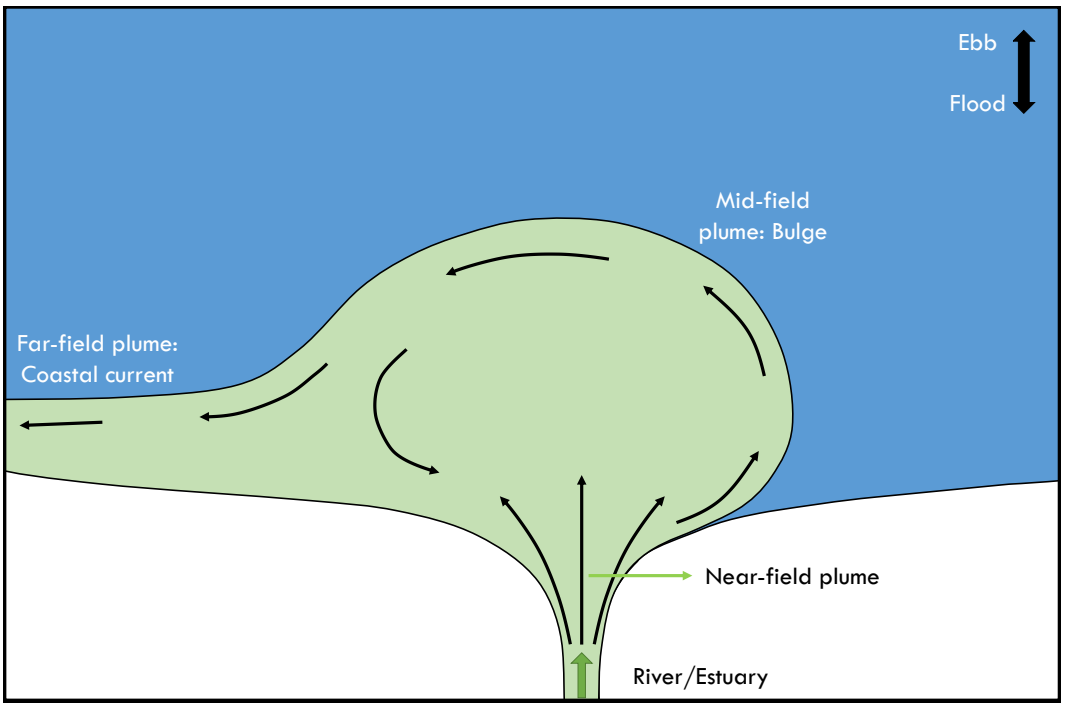

Figure 1.1: Conceptual model showing the dynamical regions of an idealized river plume in the Southern Hemisphere. Figure modified from Horner-Devine et al. (2015).

large spatial scales, produces lower dissipation rates of turbulent kinetic energy (TKE) in the far-field regions in comparison to the strongly energetic regions such as the near-field region or the plume front. Tides play a crucial role in the mixing processes within a river plume. In particular, tides can alter the frontal propagation speeds and direction, thus modifying frontal mixing (Rijnsburger et al., 2018).

Within estuaries, tidal influence is governed by factors such as estuarine morphology, tide range, water and sediment discharge, winds, and shelf processes, resulting in tide-dominated and river-dominated estuaries. In the case of tide-dominant estuaries, tidal currents play a dominant role in controlling the fate of riverine sediment: Marine water extends farther upstream, often resulting in the formation of subaqueous flood deltas (Wells, 1995). The interaction between tides and the river flow results in the upstream transport of bedload sediment and inhibition of density-driven circulation. Alternatively,

when the river discharge becomes sufficiently large, the tidal effects become negligible, resulting in a transition to river-dominant estuaries, wherein the flow becomes unidirectional. This unidirectional flow during ebb tides aids in establishing seaward-directed Eulerian residual currents at the river mouth, often amplifying tidal velocities (Leonardi et al., 2015).

1.3 Hydrodynamics and sediment transport within mangrove environments

Flow within mangrove environments is influenced at different scales by the drag induced by the vegetation. Mangrove environments typically constitute wide intertidal zones, terrestrial at low tides, and aquatic at high tides, wherein the ecological processes interact with hydrodynamic and morphodynamic processes. In mangrove forests, the vegetative drag slows the ebb tide and improves channel flow via creeks (Mazda et al., 1995; Wolanski et al., 1980). Due to these tidal asymmetries, sediment is imported into the mangrove forest (Wolanski et al., 1980). In contrast, due to the delayed discharge of water from the hydraulically rough vegetated regions, flow inside channels within forests is frequently ebb-dominant (Mazda et al., 2007). These channels allow for substantial exchange of materials between the forest and the ocean and are maintained through self-scouring (Wolanski et al., 1980).

Within mangrove vegetation, flow routing is controlled by the balance of drag forces, turbulence generated by the vegetated drag, bottom friction, and wind stress (Mazda and Wolanski, 2009). However, due to negligible bottom friction (compared to vegetative drag; Nepf 1999) and inhibition of wind stress due to mangrove trees (Mazda et al., 2005) flow routing in mangroves is predominantly dependent on the force balance between the drag force and vegetation density. Patterns of flow rotation have been observed in field studies (e.g. Mullarney et al., 2017) and numerical experiments (e.g. Horstman et al.,

2015). In forests with incised creeks, due to the difference in friction between un-vegetated and vegetated areas, two varying flow regimes arise (Horstman et al., 2013). "Creek flow," characterized by strong currents in the creeks, and little exchange across the forest occurs during times of low water. The alternative regime called "sheet flow," allows direct exchange with the forest and only occurs when the water level rises above the threshold depth. Furthermore, mangroves can be effective buffers against storm surges and coastal flooding (associated with tsunamis) by dissipating tidal currents and waves through the vegetative drag generated within the aerial roots and canopy systems (Temmerman et al., 2023).

Previous studies (e.g. Masse and Murthy, 1992) have established that mangroves play an essential role in the dissipation of wind and swell waves and the protection of coasts against storm surges (Zhang et al., 2012). The water depth, which depends on bathymetry and tidal stage, the incident wave height, and vegetation features (density, size, and spatial distribution) are all known to impact wave attenuation in mangroves (McIvor et al., 2012). Wave dissipation is most significant at water depths below the bottom root or above the upper leaf canopies of mangrove trees (e.g. Mazda et al., 2006; Brinkman et al., 1997) and diminishes for intermediate water depths due to fewer obstacles causing drag.

Sediment dynamics in mangrove environments have been studied previously using field studies (e.g. Norris et al., 2019), numerical modeling studies (e.g. Horstman et al., 2015) and laboratory studies (e.g. Nepf, 2012a). Suspended terrigenous material is delivered into mangrove forests by rivers (Thom, 1967), the combined action of tides and waves (Ellison, 2009) or by storm or tsunami occurrences (Bouma et al., 2014). Over time, accretion occurs in mangrove forests when the deposition rate exceeds the erosion rate. Conversely, in a mangrove environment, erosion occurs when the hydrodynamic forces of

tidal currents and waves exceed the shear stress of the substrate. Nepf and Vivoni (2000), in their experimental study in open channel flumes, established two flow regions within a canopy. Firstly, an upper zone where turbulence exchange is the dominant contributor to the momentum is termed "vertical exchange zone," and a lower zone where the longitudinal advection is predominant is termed "longitudinal exchange zone." They further substantiated that factors such as canopy morphology, density, and flexibility determine the vertical extent of these zones. Mangrove sedimentation is also aided by flocculation/deflocculation processes and by the creation of turbulence in the wake of mangrove roots (Furukawa and Wolanski, 1996). Within sufficiently thick vegetation, wake turbulence can generate eddies and stagnation zones that aid in the capture of suspended sediments.

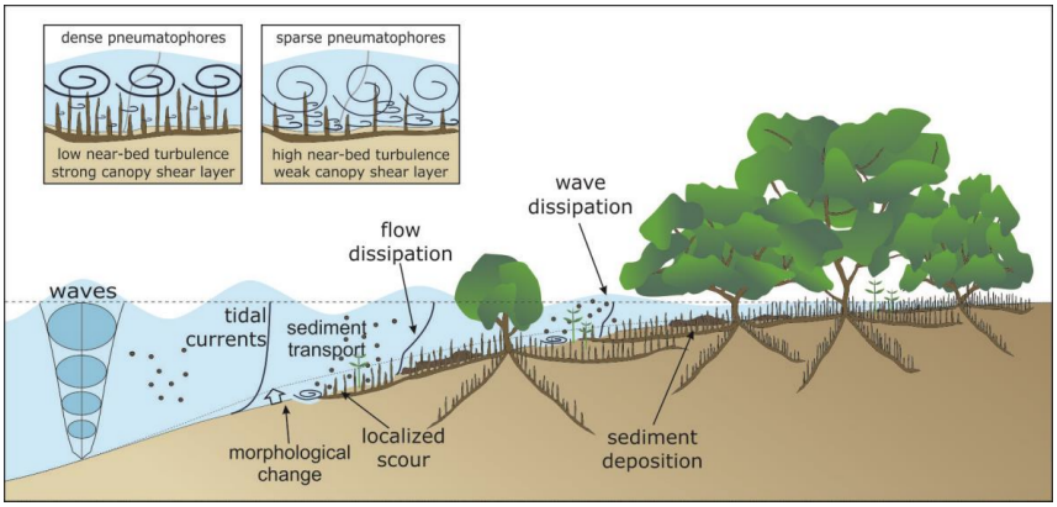

Figure 1.2: Schematic representing physical processes and biophysical interactions within a typical mangrove forest. Figure from Horstman et al. (2018).

At the various temporal and spatial scales, hydrodynamic and morphodynamic processes are interlinked within a mangrove environment (Bullock et al., 2017). Over time long-term processes in mangroves feed back into the short-term processes by altering the biogeomorphic landscape that affects the mangroves' inundation time, sediment supply, and sediment transport capacity (McIvor et al., 2013). Small-scale processes within mangroves, particularly

occurring in the transition zones between the forest and the tidal flats, may influence the sediment erosion/deposition balance (Figure 1.2), thereby playing a crucial role in the overall morphological evolution of the forest (Mullarney et al., 2017). In particular, attenuation of hydrodynamic forces and small-scale interactions between the water and vegetation elements can create a suitable environment for sediment deposition within the forest, as illustrated in Figure 1.2. In other cases however, the presence of vegetation aids in the generation of wake turbulence at small length scales, which corresponds to the width and the spacing between the obstacles to the flow, thereby leading to resuspension and local scour (Mullarney et al., 2017).

The previous sections have outlined studies concerning the large-scale morphological processes in mangrove environments and sediment dynamics within a river plume system; however, the underlying complex interactions between river plumes and mangroves are relatively understudied.

1.4 Research questions

The overarching aim of this thesis is to examine how the interplay between tidal processes, river flows, and winds influences the sediment transport patterns resulting from a mangrove-lined river debouching into a coastal bay. I will answer the following research questions:

- How does the presence of vegetation affect river plume dynamics and associated sediment transport patterns within a mangrove environment? Specifically, what principal momentum contributors influence sediment transport within the forest, fringe, and the tidal flat of a mangrove forest?
- How does the change in freshwater discharge and the presence of winds influence these sediment transport patterns?
- How does the presence and coalescence of multiple nearby river plumes

alter the sediment transport and deposition patterns within a coastal mangrove environment?

1.4.1 Approach used in this thesis

To answer the aforementioned research questions and to understand the underlying hydro-morphodynamics of river plume interactions with mangrove vegetation, we used a numerical model, which was a highly idealized version of a real system (the Firth of Thames in New Zealand), yet nonetheless retained sufficient complexity to replicate key elements of the system adequately. This reductive approach allows for easier comprehension of the underlying dynamics of a complex heterogeneous environment and provides enhanced computational efficiency. For this thesis, an idealized numerical model was created in Delft3D.

1.4.2 The Firth of Thames

Of all the 73 countries in the world with the presence of mangroves (Giri et al., 2008), New Zealand sits at the southernmost extent. The monospecific mangroves in New Zealand are *Avicennia marina*. In contrast to the global trends, mangroves in New Zealand have expanded substantially over the past 60 years (Figure 1.3b) due to sediment input associated with deforestation and land-use changes (Horstman et al., 2018).

One of the principal sites of mangrove habitat in New Zealand that has been experienced particularly rapid growth is the Firth of Thames, located on the east coast of the North Island (S37°12′ E175°30′) of New Zealand (Figure 1.3). Bounded by the Coromandel and Hunia Ranges to the east and west, respectively, the Firth of Thames estuarine embayment occupies the Hauraki Depression (Swales et al., 2007). Historical aerial photography has revealed that the Firth of Thames was a sandy tidal flat in the 1950s with some mangroves solely at river mouths; however, by 2007, mangroves comprised of *Avicennia marina* occupied a $\sim 800\,\mathrm{m}$ wide zone on an upper-intertidal platform (Love-

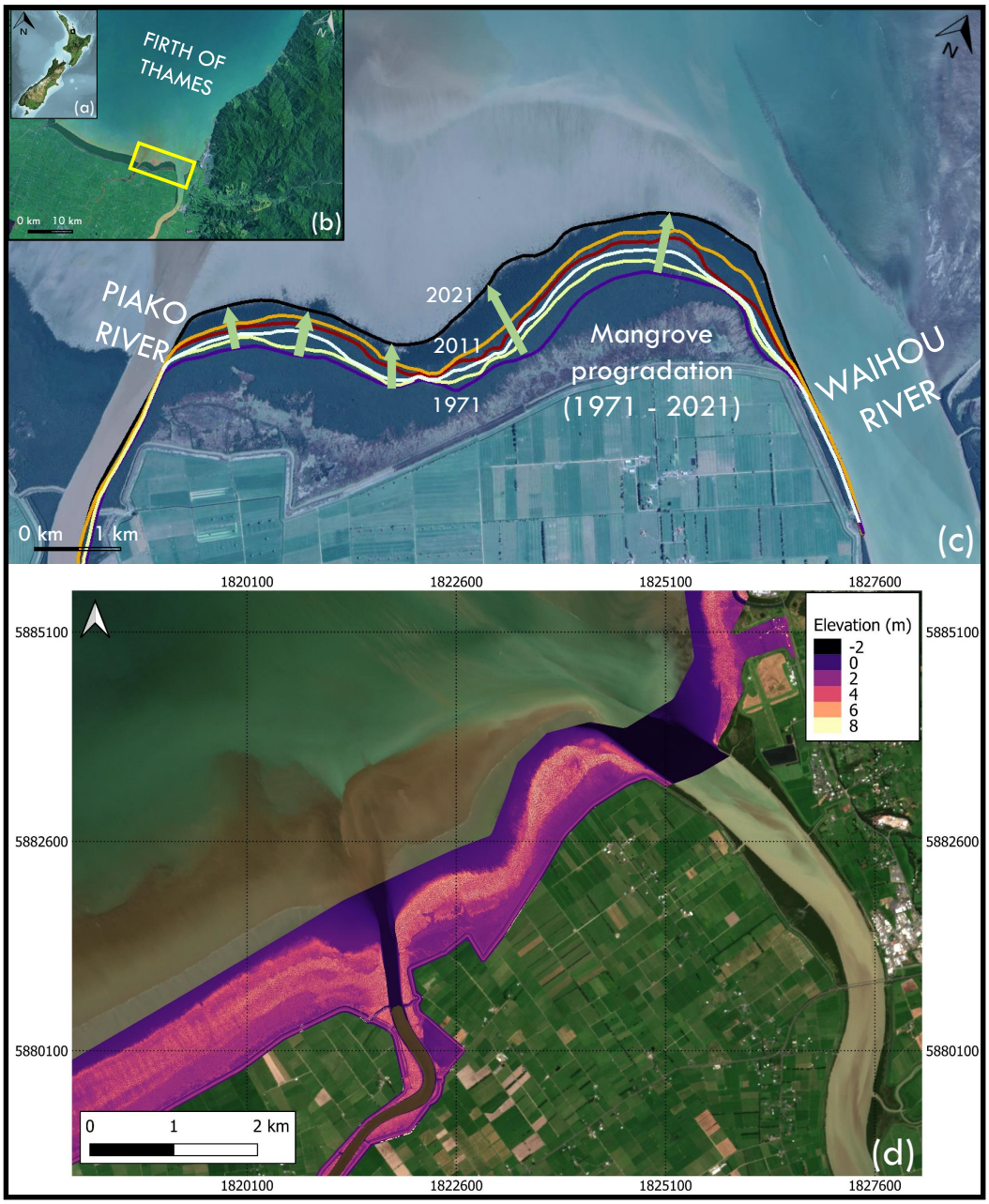

Figure 1.3: Inset (a) shows the map of New Zealand and the location of the Firth of Thames (thick black box). Panel (b) displays the broader Firth of Thames field site and the location of the Waihou and Piako rivers. Panel (c) shows the progradation of the mangrove forest based on the Landsat imagery (1971 - thick purple line, 2011 - thick orange line, and 2021 - thick black line) obtained from the U.S. Geological survey. Panel (d) displays LiDAR measurements of the Firth of Thames with elevation data. Green arrows in Panel (c) show the direction of mangrove expansion.

lock et al., 2010). The Firth of Thames has a shelf-slope bathymetry wherein the southern region shoals southwards from 10 m water depth to broad mud-

flats (Naish, 1990).

The Firth of Thames has a temperate climate with monthly mean air temperature ranging from 10.3°C in July to 19.8°C in February. The mean annual rainfall in the Firth of Thames recorded by the New Zealand Meteorological Service is 1211 mm, and mean monthly rainfall varies from 73 mm (January) to 145 mm (July). The two largest rivers, Waihou and Piako, enter the Firth of Thames from the south and deliver combined freshwater runoff from $\sim$ 3600 km^2 of catchment. The eastern Waihou river delivers nearly 160,000 $t.yr^{-1}$, and the centrally located Piako river delivers nearly 30,000 $t.yr^{-1}$ of suspended sediment into the Firth of Thames (Hicks et al., 2011). The tidal influence on the Waihou River is extensive, with tides during low flow conditions typically affecting the river level as far as Te Aroha monitoring station of the Waikato Regional Council located $\sim$ 8 km upstream of the river mouth (Webster, 1995). The mean flow for the Waihou River at Te Aroha ranges from 25.7 $m^3.s^{-1}$ to 91.8 $m^3.s^{-1}$ (Hill, 2011).

The Firth of Thames is mesotidal with average spring and neap tidal ranges of 2.9 m, and 2.2 m, respectively. Throughout the Hauraki Gulf, the tide is characterized as a standing wave wherein the high tide occurs nearly simultaneously throughout the region with a weak residual circulation (Bowman and Chiswell, 1982). Tidal-current speeds are $\leq$ 0.3 $m.s^{-1}$ on an average tide. Within the Firth of Thames, northwesterly (35.8%), westerly (24.7%), and northerly (18.5%) winds constitute the dominant wind directions (Naish, 1990). A wind rose recorded by the Firth of Thames weather station for the years 2019-2020 is show in the Figure 1.4c.

The presence of southerly and westerly winds produces a large-scale anticlockwise circulation that can trap the river-borne suspended sediments within the southern Firth of Thames (Healy, 2002), while northerly and westerly

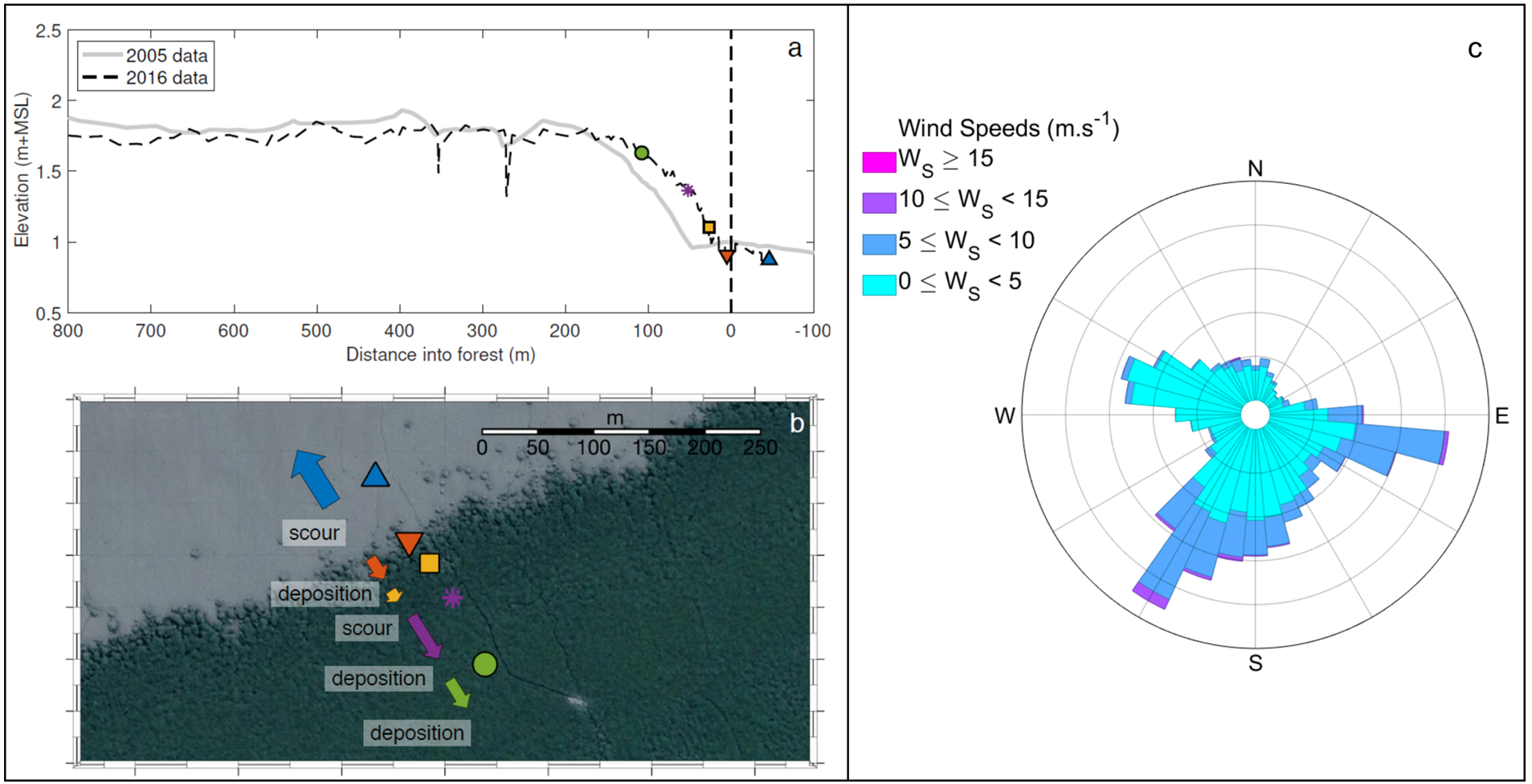

Figure 1.4: Panel (a) shows the elevation profile along mudflats to forest (m + MSL) recorded for 2005 (thick grey line) and 2016 (thick dashed black line). Panel (b) shows the conceptual diagram displaying the sediment fluxes in and out of the mangrove forest (adapted from Lovett 2017). Panel (c) shows wind rose created using hourly wind data from a NIWA weather station at Firth of Thames ([S37°12′ E175°30′]) over the period 2019-2020. Colors indicate wind speeds, bars indicate direction from and the length of the bars indicate the frequency of occurrence of the wind conditions.

winds generate a clockwise residual circulation of currents. In the central region of the Firth of Thames, predominant northwesterly and northerly wind directions generate small and short-period waves with mean significant wave heights of 0.41 m and a maximum average wave period of 8.6 s (Swales et al., 2007).

Mangrove habitat in the Firth of Thames currently and occupies a $\sim$ 800 m wide forest with a mean high water spring tide (MHWS) elevation of 1.6 m above the mean sea level (MSL). The characteristics of mangroves vary throughout the forest. In particular, trees are characterized by open spreading forms along the forest fringe. The forest trees tend to have straight vertical trucks with heights ranging from 0.5 m and 3.5 m. Pneumatophores in the region emerge up to 25 cm in height from the bed and are nearly 1 cm in diameter (Horstman et al., 2018). Due to elevation with respect to tides, the hydroperiod on the mangrove forest is less than 3% yearly (Swales et al., 2015). However, owing to a small tidal prism, tidal creeks are not developed within the forest (Montgomery et al., 2018).

Within mangrove environments, sediment transport and deposition patterns contribute towards the vertical accretion of intertidal mudflats, which acts as a precursor to mangrove seedling establishment. This seedling establishment also helps further spread the forest (Roskoden et al., 2020). To efficiently manage these ecosystems, an understanding of key processes controlling hydrodynamics, sediment transport and deposition patterns, and morphodynamics is of key importance.

1.4.3 Thesis outline

This thesis consists of three major scientific chapters, which form the main body and are focused on the idealized numerical simulations with cohesive sediments. Each chapter in this thesis was intended as a stand-alone document

for submission to a peer-reviewed journal.

- In Chapter 2 of this thesis, I examine the interactions between mangrove vegetation and a single river plume system using an idealized numerical model. The 3-dimensional morphological model was developed in Delft3D and was designed as an idealized version of the Firth of Thames mangrove forest in the North Island of New Zealand. This study examined river plume dynamics and how the associated sediment transport patterns change due to the presence of mangrove vegetation. This work was published in *Continental Shelf Research* in 2021, with me as the first author.

- In Chapter 3, I explore the influence of forcing factors of river discharge and winds on the dynamics of the river plume along with the resultant sediment deposition patterns in a mangrove environment. The numerical model grid was the same as in Chapter 2 under different forcing regimes. The model scenarios were chosen based on the climatic data recorded for the Firth of Thames averaged over a year. For each numerical simulation, total, riverine, and bed-sourced sediment fluxes along the edge of the mangrove forest were evaluated and compared. This work has been submitted to *Estuaries and Coasts,* with me as the first author.

- In Chapter 4, the links are explored between the coalescence of two nearby river plumes and the corresponding sediment transport patterns in a mangrove environment. The idealized numerical model used in Chapters 2 and 3 was modified to include an additional river, and sediment transport fluxes along the edges of three mangrove forests (central, western, and eastern) were analyzed. Additionally, the influence of wind on plume coalescence and the consequences to sediment transport were investigated. This work has been submitted to *Estuarine, Coastal and*

Shelf Science, with me as the first author.

Chapter 5 summarizes the main findings of this thesis and ends with suggestions for future work.

Chapter 2

The interaction of buoyant coastal river plumes with mangrove vegetation and consequences for sediment deposition and erosion in a tidal environment

Contribution of authors

Chapter 2 duplicates a paper of the title "The interactions of the buoyant river plumes with vegetation and consequences for sediment transport in a mangrove environment" by Hemanth Vundavilli, Julia C. Mullarney, Iain T. MacDonald, and Karin R. Bryan, which was published in *Continental Shelf Research* in 2021. The majority of text and figures are identical to the published version with the exception of the relabeling of figures, tables, equation numbers, and a few changes as suggested by the examiners of this thesis. Along with development of the idealized numerical model using Delft3D, I wrote MATLAB scripts to process and analyze the model data. Along with the preparation of initial and subsequent drafts, I prepared all the figures for this manuscript. My co-authors, Julia C. Mullarney, Iain T. MacDonald, and Karin R. Bryan edited my drafts along with providing helpful comments, direction, and editorial help responding to reviewers' comments.

Abstract

To identify the drivers of sediment deposition within a mangrove-lined river delta, we developed a three-dimensional numerical model in an idealized domain. Our model system is based on the Firth of Thames, a modern flat-fronted, bay-head deltaic system, in the Hauraki Gulf, in the North Island of New Zealand. The interactions of the buoyant river plume with mangroves are examined, including sediment deposition and erosion patterns. The morphological study presented here is restricted to cohesive sediments, whose patterns are observed after 4 months of morphological evolution. For the non-vegetated case, represented by a spatially uniform roughness, sediment deposited throughout the central model domain with a formation of a cuspate delta at the river mouth. However, in the vegetated case (with vegetated areas represented by an enhanced and spatially varying roughness coefficient), sediment deposition occurred in the regions of forests and flats, whereas the fringe areas experienced erosion. The sediment deposition patterns along cross-sections were qualitatively consistent with field observations from the Firth of Thames. Analysis of the across-transect and along-transect momentum balances demonstrates that the predominant balance between the bottom shear stress and baroclinic pressure gradient largely controls the sediment deposition in the riverine sections of the domain. However, close to the center of the plume, vertical advection promotes suspension of the sediments in the fringe region during the flood tide.

2.1 Introduction

Freshwater river systems are the primary mechanism of transporting sediments to the coast. Understanding the transport and deposition of this sediment is essential for predicting the morphological evolution of coastal regions. As the buoyant freshwater merges with deeper and saline ocean waters, the horizontal advection of the freshwater establishes the shape and characteristics of the river plume, and thus also influences the distribution of sediments (both suspended and bed sediments) along the coast.

Field observations, laboratory flume experiments, and numerical models have been used to investigate the effects of the external influence of wind stresses, tidal forcing, storms, and discharges on plume dynamics. Numerical models have been shown to accurately reproduce observations from large river systems such as the Eel, Delaware, and Amazon Rivers (Pullen and Allen, 2000; Whitney and Garvine, 2006; Nikiema et al., 2007, respectively). Other studies (Chao and Boicourt, 1986; Fong and Geyer, 2001; García Berdeal et al., 2002; Hetland, 2005) used idealized numerical simulations formulated with single river inputs and straight coastlines to investigate how river plumes respond to wind stresses. The processes that control the dynamics of the downstream expansion of plumes are found to be: (1) buoyancy forces; (2) mixing due to turbulence and bottom friction; and (3) a balance between the Coriolis acceleration and the across-shore pressure gradient (Ikeda, 1984).

Within aquatic environments, the interaction of flows with vegetation substantially modifies the velocity fields and circulation patterns (e.g. Nepf, 2012a; Mullarney and Henderson, 2018). The additional drag due to vegetation slows flows and creates small-scale turbulent eddies shown in laboratory experiments (Kothyari et al., 2009; Lee et al., 2004), numerical studies (Hickey et al., 2010; Yang and Choi, 2010; López and García, 2001) and field observations (Norris

et al., 2017, 2019). Studies in mangrove environments (Wolanski et al., 1992; Iftekhar and Takama, 2008) have concluded that the flow resistance due to vegetative drag can be parameterized by a drag coefficient which in turn depends on the Reynolds number R_e and with vegetation width. Multiple studies have explored bulk parameterizations for the drag coefficient (e.g. Furukawa and Wolanski, 1996; Wolanski et al., 1980; Mazda et al., 1997; Suzuki et al., 2012) with forces quantified as

$$\frac{\text{Vegetative Drag}}{\text{Volume}} = \frac{1}{2}\rho C_D a U^2, \tag{2.1}$$

where ρ is the density of water, a is the canopy frontal area density (in m^{-1}), U is an average velocity, and C_D is the vegetation drag coefficient (Mazda et al., 1997).

The modification in drag induced vegetation has been shown to alter the sediment transport and deposition patterns (Nepf, 2012b). In a small-scale laboratory study, Zong and Nepf (2010) identified three zones of deposition. The first zone occurs as the flow diverges at the leading edge of the vegetation, where there is a rapid decrease in flow speeds and the associated increase in the deposition in the streamwise direction. The second zone is associated with the near-uniform velocity within the vegetation, suspended sediment load, and deposition rate gradually decrease in the streamwise direction. Along the sides of the vegetation, a shear layer characterized by high turbulence restricts deposition.

At fresh and saltwater transition zones, waves, tides, and winds play a significant role in controlling sediment accumulation patterns inside the vegetative environments (Zhou et al., 2016; Talke and Stacey, 2008; Carniello et al., 2011). The role of asymmetric tidal cycles and the implications for the transport of sediment has been studied extensively (Postma, 1967; Boothroyd and Hubbard, 1975; Boon III and Byrne, 1981; Pethick, 1994; Wang et al., 2002;

Fortunato and Oliveira, 2005; Brown and Davies, 2010). Tidal asymmetry can influence sediment transport by creating an imbalance in the maximum flow speeds, thereby causing either flood dominance or ebb dominance (Friedrichs, 2011). Regions with faster flood velocities (flood dominant) lead to sediment import and deposition, and conversely, regions with faster ebb velocities (ebb dominant) move the sediment seaward (Speer et al., 1991). However, net sediment transport in the case of inter-tidal regions with minimal spatial variations of velocity or stresses over a tidal cycle occurs in response to time-dependent asymmetries (Friedrichs and Aubrey, 1988; van Maanen et al., 2013).

Dronkers (1986) established that sediment transport patterns, particularly the potential directions of fine suspended sediments (small grain sizes), can be evaluated using the slack tide duration. The longer slack water lasts at high tide; the more time is available for fine sediments to settle from suspension. The presence of decreased tidal range and shorter duration of high water on the tidal flats results in net seaward sediment transport (increased erosion), thereby favoring a concave-up tidal flat profile. In contrast, in regions with increased tidal range and longer duration high water periods, net shoreward transport occurs (increased deposition) and favors a convex-up tidal flat profile (Friedrichs, 2011).

Sediment transport dependencies on tidal asymmetry change with sediment grain sizes. In particular, while local asymmetries in maximum velocities affect the coarser sediments, fine sediments are dependent on the duration of slack tides (Friedrichs, 2011; Hunt et al., 2016). Slack tidal asymmetry assumes that sediment suspension and transport increase with the magnitude of bed shear stress above the critical stress (τ_c). Longer slack water durations around high tide compared to low tides favor landward sediment transport as the time required for sediment to settle after the flood is increased and vice-versa (Dronkers, 1986).

While the above studies have helped understand the dynamics of flow in vegetated regions and the dynamics of buoyant river plumes in isolation, the interactions of buoyant plumes with vegetation are still relatively less explored. The aim of this study is not to provide a comprehensive review of sediment transport dependencies on various physical parameters as provided in previous literature (e.g., Fong and Geyer, 2002; Schiller et al., 2011; Kourafalou et al., 1996; Garvine and Monk, 1974), but instead to examine how plume dynamics and associated sediment transport differ between cases with a spatially varying (vegetated) and uniform (non-vegetated) bottom roughness.

The model we present here is designed as an idealized version of the Firth of Thames mangrove forest in New Zealand. Although the key dimensions are similar to those of the real system, for our study, multiple simplifications have been made to allow us to explore the fundamental underlying dynamics of the system without the additional complexities arising from the asymmetric geometry. Chao and Boicourt (1986) applied a 3D primitive equation model consisting of an estuarine channel connected normal to a straight coastline filled with saline water to investigate the development of a plume by a fresh-water discharge. They established that a fully developed plume consisting of features such as an anticyclonic turning region could be produced over a shelf with a discharge of 10 days. Our study uses their result as a motivation to avoid simulations over long time scales, which increase the computational loads significantly. To analyze the major momentum contributors in the forest, fringe, and tidal flats, we performed a series of numerical simulations for two cases: (1) a domain with uniform bed roughness and (2) using a spatially varying bed roughness in the model to mimic the presence of vegetation in Delft3D. Horstman et al. (2013), successfully applied and validated this usage, which is more computationally effective than other methods such as implementing a directional point model (DPM) to account for the vegetation (Temmerman

et al., 2005, 2007). In our study, we use a three-dimensional idealized model to explore how sediment deposition and erosion processes are influenced by the interaction of a buoyant river plume with vegetation. In particular, we use this model to explore slack water asymmetry patterns and momentum balances to identify dominant controls on sediments' distribution and transport.

Section 2.2 of this paper describes the model, governing equations, and the solution procedure. Section 2.3 describes the numerical model setup and initialization of our model simulations. In Section 2.4, we explore the tidal asymmetry patterns and momentum balances in across-transect and along-transect directions for both the flood and peak ebb phases of the tidal cycle. As the flow is strongly vertically stratified, we present the momentum balances within both the surface and bottom layers. Additionally, in Section 2.4, we present the changes in deposition patterns due to vegetation across two transects from the forest interior to intertidal mudflats at different locations within the river plume. Lastly, discussion and conclusions are presented in Section 2.5 and Section 2.6, respectively.

2.2 Model setup

2.2.1 Governing equations

For this study, we used the Delft3D software package, which has been successfully applied for simulating hydrodynamics, sediment dynamics, and morphological processes across a wide range of modeling studies (e.g., Elias et al., 2001; Lesser et al., 2004; Hibma et al., 2003; Hu et al., 2009; Temmerman et al., 2005). The flow module of Delft3D determines the flow characteristics by solving the three-dimensional (3D) or two-dimensional (2DH, depth-averaged) unsteady shallow-water equations using the Boussinesq assumptions along with continuity equations (Lesser et al., 2001). The flow module is coupled to a sediment transport morphological model, which updates the evolution of the

bed simultaneously with the hydrodynamics. We briefly summarize the equations here. However, for a complete description, refer to Deltares (2021) and Roelvink and Van Banning (1995).

2.2.1.1 Momentum equations

In the vertical direction, we chose a boundary-fitted (σ - coordinate system), where the number of layers over the computational area are constant at any given water depth. The σ-coordinate system is defined as:

$$\sigma = \frac{z - \zeta}{h + \zeta}, \tag{2.2}$$

where z is the vertical coordinate in physical space, ζ is the free surface elevation above the reference ($z = 0$), h is the water depth.

In the horizontal direction, Delft 3D-FLOW uses orthogonal curvilinear coordinates in spherical or Cartesian coordinates. The horizontal momentum equations in x and y directions are:

$$\frac{\partial U}{\partial t} + U\frac{\partial U}{\partial x} + V\frac{\partial U}{\partial y} + \frac{\omega}{h}\frac{\partial U}{\partial \sigma} - fV = -\frac{1}{\rho_0}P_x + F_x + M_x + \frac{1}{h^2}\frac{\partial}{\partial \sigma}\left(v_{\mathrm{V}}\frac{\partial u}{\partial \sigma}\right), \tag{2.3}$$

$$\frac{\partial V}{\partial t} + U\frac{\partial V}{\partial x} + V\frac{\partial V}{\partial y} + \frac{\omega}{h}\frac{\partial V}{\partial \sigma} + fU = -\frac{1}{\rho_0}P_y + F_y + M_y + \frac{1}{h^2}\frac{\partial}{\partial \sigma}\left(v_{\mathrm{V}}\frac{\partial v}{\partial \sigma}\right), \tag{2.4}$$

where U, V denote the flow velocities in the x and y directions, respectively, ω denotes the vertical velocity in the σ direction, f is the Coriolis parameter, h is the water depth, ρ is the density of water, ρ_0 is the reference density of water taken as 1000 kg.m^{-3}, v_{H} is the horizontal eddy viscosity, v_{V} is the vertical eddy viscosity, D_H is the horizontal eddy diffusivity, and D_V is the vertical eddy diffusivity. M_x represents the contributions due to wind stress on the

surface layer and bed shear stress in the bottom layer in the x direction. M_y represents the contributions due to wind stress on the surface layer and bed shear stress in the bottom layer in the y direction.

The horizontal pressure terms P_x, and P_y, are solved using the Boussinesq approximations as,

$$\frac{1}{\rho_0}P_x = g\frac{\partial\zeta}{\partial x} + g\frac{h}{\rho_0}\int_\sigma^0 \left(\frac{\partial\rho}{\partial x} + \frac{\partial\sigma'}{\partial x}\frac{\partial\rho}{\partial\sigma'}\right) d\sigma', \tag{2.5}$$

$$\frac{1}{\rho_0}P_y = g\frac{\partial\zeta}{\partial y} + g\frac{h}{\rho_0}\int_\sigma^0 \left(\frac{\partial\rho}{\partial y} + \frac{\partial\sigma'}{\partial y}\frac{\partial\rho}{\partial\sigma'}\right) d\sigma'. \tag{2.6}$$

.

The horizontal viscous stresses F_x and F_y, are evaluated through the commonly adopted eddy viscosity approach. The forces are of the form,

$$F_x = v_{\mathrm{H}}\left(\frac{\partial^2 U}{\partial x^2} + \frac{\partial^2 U}{\partial y^2}\right), \tag{2.7}$$

$$F_y = v_{\mathrm{H}}\left(\frac{\partial^2 V}{\partial x^2} + \frac{\partial^2 V}{\partial y^2}\right). \tag{2.8}$$

.

In order to evaluate the vertical velocity for each layer in the σ direction (ω), the continuity equation is used:

$$\frac{\partial U}{\partial x} + \frac{\partial V}{\partial y} + \frac{\partial W}{\partial z} = 0, \tag{2.9}$$

where W denotes the velocity in the z direction.

Three-dimensional transport of suspended sediment is evaluated by solving the 3-D (advection-diffusion) transport equation in Delft3D which reads:

$$\frac{\partial c}{\partial t}+\frac{\partial(Uc)}{\partial x}+\frac{\partial(Vc)}{\partial y}+\frac{\partial\left(w-w_s\right)c}{\partial z}=\frac{\partial}{\partial x}\left(D_H\frac{\partial c}{\partial x}\right)+\frac{\partial}{\partial y}\left(D_H\frac{\partial c}{\partial y}\right)+\frac{\partial}{\partial z}\left(D_V\frac{\partial c}{\partial z}\right)+S, \tag{2.10}$$

where c is the mass concentration, w_s is the particle settling velocity in a mixture, and S is a source or sink term.

2.3 Study area

Our model domain is loosely based on the Firth of Thames (FoT), located in the North Island [S37°12′ E175°30′]) of New Zealand (Figure 2.1a and b). The Waihou, Piako, and Waikataruru rivers enter the Firth of Thames, which is located in the southern region of the Hauraki Gulf. *Avicennia marina* mangroves were originally found only at the river mouths but over the last 60 years have rapidly colonized the whole of the southern Firth region (Figure 2.1c). The forest is now $\sim$1 km in width. This expansion has been attributed to sediment input associated with deforestation and land-use changes (Lovelock et al., 2010). The buoyant inflow from the largest river, Waihou, generates a large persistent freshwater and sediment plume (Figure 2.1c).

2.3.1 Model grid and bathymetry

We used a domain-decomposed curvilinear grid composed of three smaller model domains. The outer domain includes the tidal boundary and has a varying grid resolution of 500 m x 900 m to 200 m x 475 m. The central domain, which encompasses the mangrove forest and the intertidal mudflat, is made up of a highly refined grid with a varying resolution of 15 m x 6 m in the mangrove region to a maximum of 218 m x 140 m. The lower domain includes the river and river boundary with resolution varying from 25 m x 17 m at the river mouth to 15 m x 10 m at the river boundary (Figure 2.1d). All transitions between the grid domains follow the guidelines provided in Delft3D manual

(Deltares, 2021). We conducted a sensitivity analysis in both the horizontal and vertical directions, and as the further refinement did not change the results substantially, we chose the above horizontal and vertical resolutions to minimize the computational time of our simulations.

The idealized model bathymetry was developed from the depth contours extracted from the region's hydrographic chart and hence represented a similar bathymetry to the Firth of Thames, but ensuring symmetry along the longitudinal axis (Figure 2.1e). Near land boundaries, the depth was gradually decreased in the shallow areas to suppress any artificial reflections from the boundaries. The model has five sigma layers in the vertical direction of equal layer thicknesses (20% of the water depth).

2.3.2 Initial boundary conditions and parameter settings

For simulations with river flow and tidal forcing, we imposed a water level condition at the northern seaward boundary, which was forced with an M2 astronomic tide of the amplitude of 1.3 m with a phase of 0^o, while the southern river boundary was forced by a constant freshwater discharge of $35\,\mathrm{m^3 s^{-1}}$ across the whole boundary. This discharge value was based on the seasonal average flow recorded at an upstream monitoring station by the Waikato Regional Council over July 2019 to September 2019. Salinity and sediment were set to uniform across the boundaries (horizontally and vertically). The model simulations throughout this paper are initialized with no flow and a uniform Delft3D salinity of 31 ppt. As the primary goal of this study is to investigate the interaction of a river plume with vegetation and to explore the sediment deposition, we neglect the effects of winds or any other external forcing parameters. The Coriolis parameter was set at -37^o latitude in the model. The wetting and drying threshold depth in the model was set at the default value of 0.1 m.

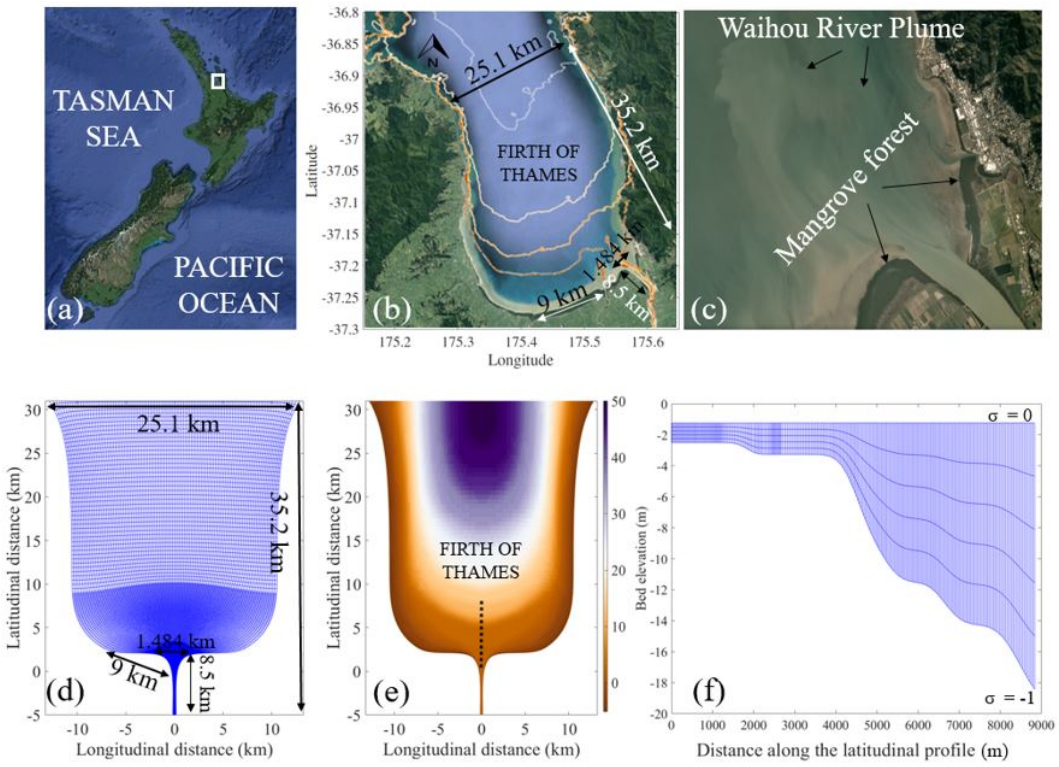

Figure 2.1: (a) Location of Firth of Thames in New Zealand (white box). (b) Firth of Thames and key dimensions. (c) Satellite image of the Waihou River sediment plume and mangroves. (d) Idealized symmetric model grid with open boundaries at the northern and southern ends of the domain. (e) Idealized symmetric bathymetry in (m), (f) shows the latitudinal profile along the center of the domain from the river mouth (dashed line in (e)) of bed elevation in (m) with vertical mesh grids of 5 equal thickness σ layers; note that the colorbar for panels (b) and (e) is the same.

A cyclic advection scheme for momentum and transport was used, and forester filters in the horizontal and vertical direction were applied (Lesser et al., 2004). The k-ϵ scheme with default parameters was the chosen 3-D model for turbulence. Scenarios were undertaken with different roughness to examine the effects on plume propagation and deposition of the sediments. We used a spatially uniform Chézy friction coefficient of $65\,\mathrm{m}^{1/2}.\mathrm{s}^{-1}$ throughout the model for the no-vegetation scenario, which corresponds to a bottom friction coefficient of $C_D = 0.0023$. To investigate the impacts of vegetation, the central domain was divided into three roughness zones, where roughness is specified as a Chézy value. In the along-transect direction from forests to flats, the Chézy roughness varied from a minimum value of $15\,\mathrm{m}^{1/2}.\mathrm{s}^{-1}$ (across $\sim 1\,\mathrm{km}$ of the forest) to $45\,\mathrm{m}^{1/2}.\mathrm{s}^{-1}$ (~ 200-m of forest fringe) to a maximum value of $65\,\mathrm{m}^{1/2}.\mathrm{s}^{-1}$ (in the flats) over 2 km, corresponding to bottom friction coefficients of 0.132, 0.044 and 0.0023, respectively (Figure 2.2). These Chézy and bottom friction coefficients were chosen based on literature values (Zhang et al., 2012; Mazda et al., 1997).

Delft3D allows evaluation of sediment transport, bed evolution (erosion and deposition) of both cohesive and non-cohesive sediments by solving the 3-D advection-diffusion equation for the suspended sediment (Equation 2.10). Throughout this study, the sediment type was set to cohesive (mud) sediments with a riverine mud input of $0.1\,\mathrm{kg.m}^{-3}$ (representative of sediment concentration through the Waihou river during low flows), critical bed shear for erosion (τ_c) and deposition (τ_d) were set at $0.50\,\mathrm{N.m}^{-2}$ and $1000\,\mathrm{N.m}^{-2}$, respectively while the fresh and saline settling velocities were $0.25\,\mathrm{mm.s}^{-1}$. For cohesive sediments, the exchange of sediment fluxes between water and bed are evaluated using the Partheniades-Krone approach (Partheniades, 1965). In this study, sediment parameters such as erosion parameter, dry bed density, etc., were set to the default values.

To reduce computational loads, morphological evolution in Delft3D models can be accelerated using the Morphological Acceleration Factor or MORFAC without having a significant impact on the hydrodynamic flows (Roelvink, 2006; Lesser et al., 2004). The MORFAC value can be simply applied in the model to multiply the bed level changes by a non-unity factor after each hydrodynamic timestep to compute sediment transport and morphological change simultaneously with the hydrodynamics. In our model simulations, the initial sediment layer bed thickness was set at 2 m, and a MORFAC of 12 was used to simulate a morphological evolution after 4 months ($\sim$ 240 tidal cycles). The model was run for 10 days with a timestep of 0.01 minutes to satisfy the Courant-Friedrichs-Lewy condition.

2.4 Results

2.4.1 Hydrodynamic model output and plume development

We consider two transects: transect 1 extends from the forest to the intertidal mudflat, and transect 2, located closer to the river mouth (Figure 2.2). The across-transect position (x) of the different regions along the transect are identified in Table 2.1. At the transition between the forest and the intertidal mudflats, both transects are perpendicular to the forest edge. The comparison of water levels, depth-averaged velocities, and their magnitudes in across-transect and along-transect directions in different environments at 3 model observation points (OP) for transect 1 are shown in the Figure 2.3. Predicted along-transect velocities (Figure 2.3d) reached up to 0.1 $\mathrm{m.s^{-1}}$ on the mudflat model observation point 4 (OP 4) and 0.05 $\mathrm{m.s^{-1}}$ deep inside the forest model observation point 2 (OP 2).

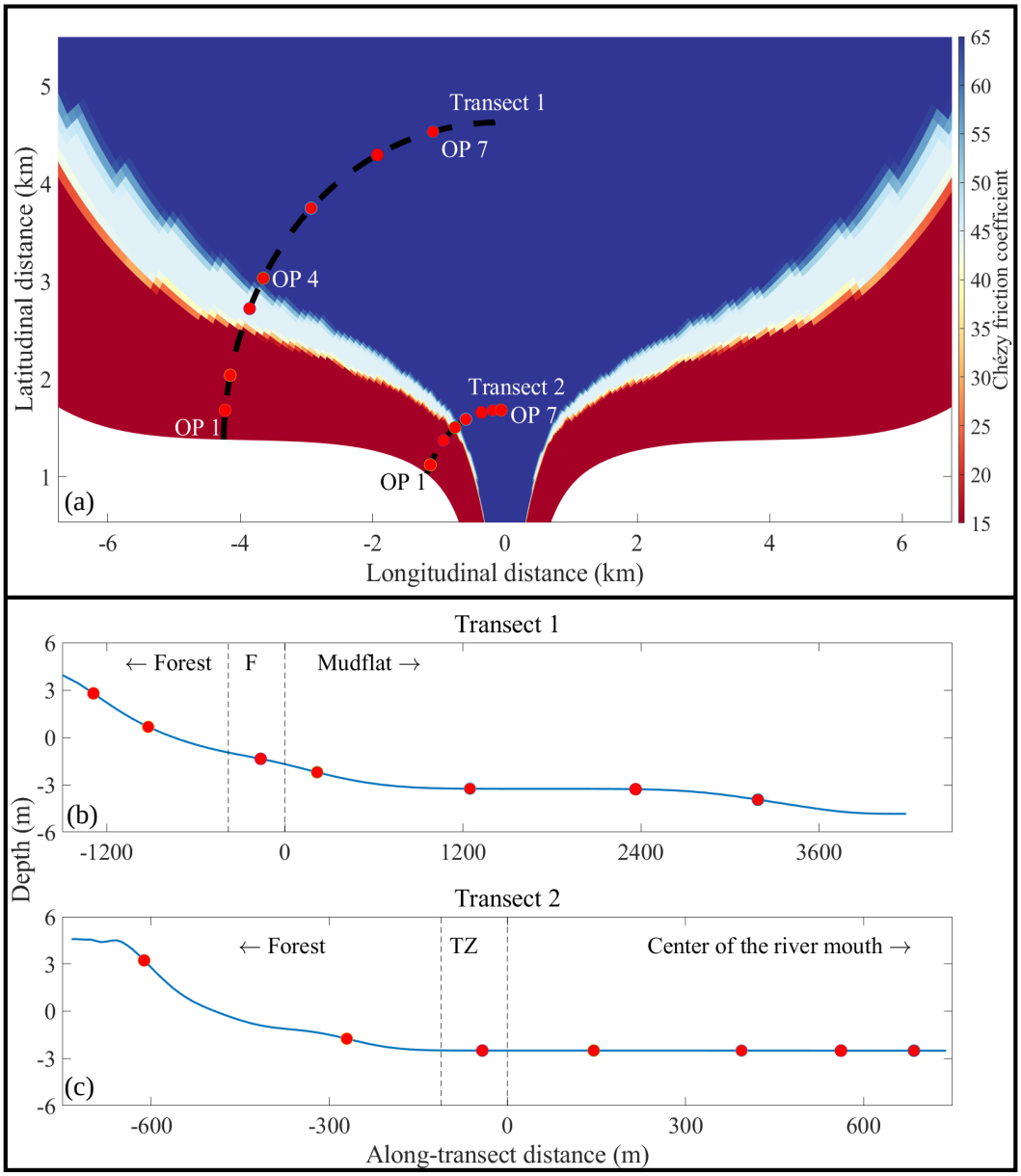

Figure 2.2: Panel (a) shows the spatially varying Chézy friction coefficient (colorbar) used in the model. Panels (b) and (c) show the depth profiles and regions of varying roughness used for transect 1 and transect 2, respectively. "F" in panel (b) and "TZ" in panel (c) denote Fringe and Transition Zone, respectively. See text for the individual Chézy and bottom friction coefficients used for each region. Locations of transect 1 and 2 (red dashed lines) and model observation points 1 to 7 (red circles).

2.4.2 Plume development

Model simulations without tidal forcing showed a large portion of plume expansion spreading into the central domain due to the absence of opposing

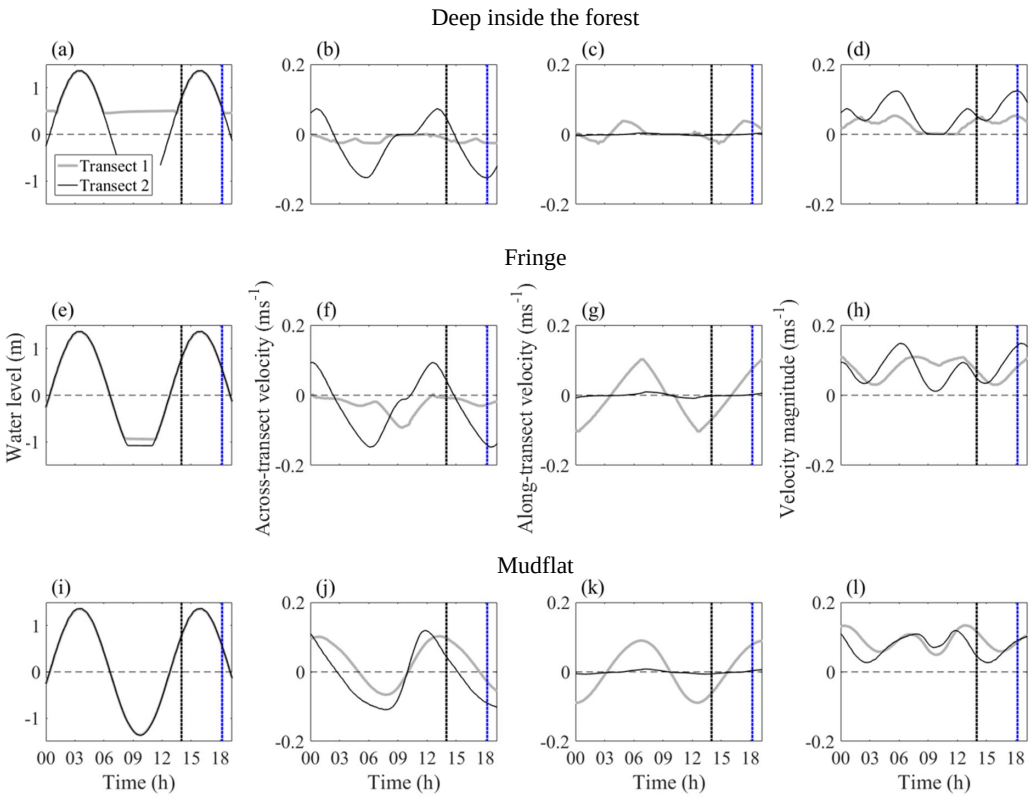

Figure 2.3: Time series (smoothed with 5-point (10-minutes) running mean of predicted water levels, across-transect, along-transect velocities and their magnitudes for different environments along transect 1 (grey thick line) and transect 2 (black thin line). Deep inside the forest (a-d, model observation point 2 in Figure 2a), fringe (e-h, model observation point 4 in Figure 2a), and the deep end of the transects (i-l, model observation point 7 in Figure 2a). Black and blue thick dashed lines show times corresponding to peak flood and peak ebb velocities at the forest edge (model observation point 2), respectively.

currents. The freshwater plume had a surface signature extending over 4 km from the river mouth during the peak ebb. While the plume was deflected slightly to the west throughout the tidal cycle, in an otherwise symmetric domain due to the Coriolis effect (Southern Hemisphere), this effect of rotation was more predominant during the peak flood stage (Figure 2.4b). Further, due to the incoming tidal currents, the plume remained trapped within the river for both the surface and bottom layers (Figure 2.4).

Tidal residual currents were evaluated for the surface and bottom layers of

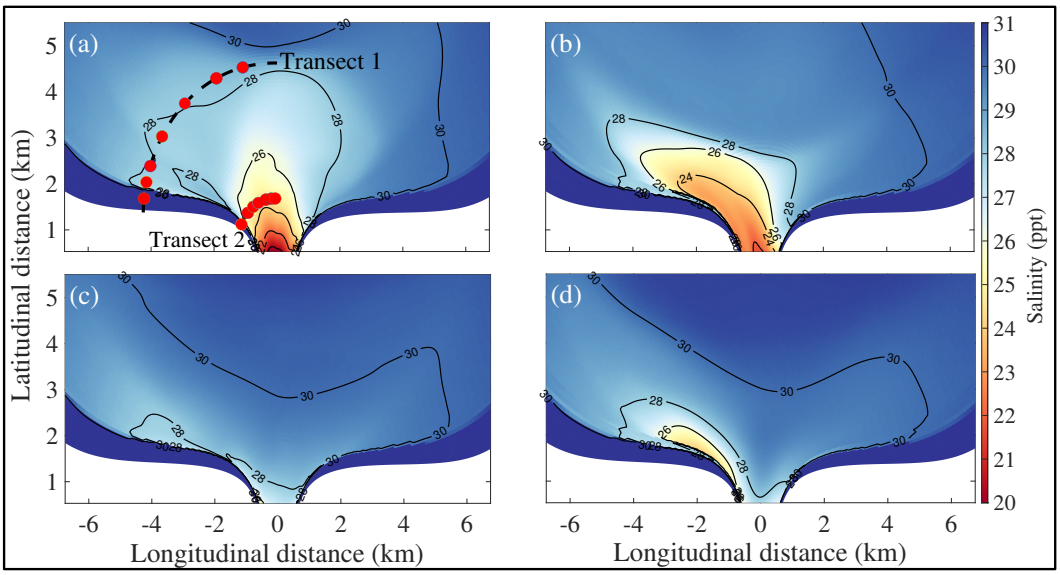

Figure 2.4: Plume expansion observed at different tidal stages. Salinity in (a) the surface layer at peak ebb, (b) surface layer at peak flood, (c) bottom layer at peak ebb, and (d) the bottom layer at peak flood. Red dashed lines indicate transects 1 and 2, and red circles show the model observation points from 1 to 7. Black contour lines show the isohalines for their respective tidal stages (Contour interval: 2 ppt).

the central domain (Figure 2.5a and b). Tidal residual currents for the deeper regions in the model showed a net mean speed of $0.2\,\mathrm{m.s^{-1}}$ near the river mouth and $0.08\,\mathrm{m.s^{-2}}$ away from the river mouth, resulting in a net-offshore transport on the surface layer (Figure 2.5a). In the bottom layer, mean speeds close to the river mouth were close to $0.06\,\mathrm{m.s^{-1}}$ while away from the river mouth it was just $0.04\,\mathrm{m.s^{-1}}$ resulting in a net-onshore transport (Figure 2.5b). In the shallow regions, residual velocities were close to $0.08\,\mathrm{m.s^{-1}}$ and $0.02\,\mathrm{m.s^{-1}}$ for surface and bottom layers, respectively.

The baroclinic deformation radius describes the length scale at which the rotational effects of the plume become more critical compared to the effects of buoyancy (Yankovsky and Chapman, 1997). Baroclinic deformation radii were evaluated both inside and outside the plume. Baroclinic deformation radius is given by Equation 2.11,

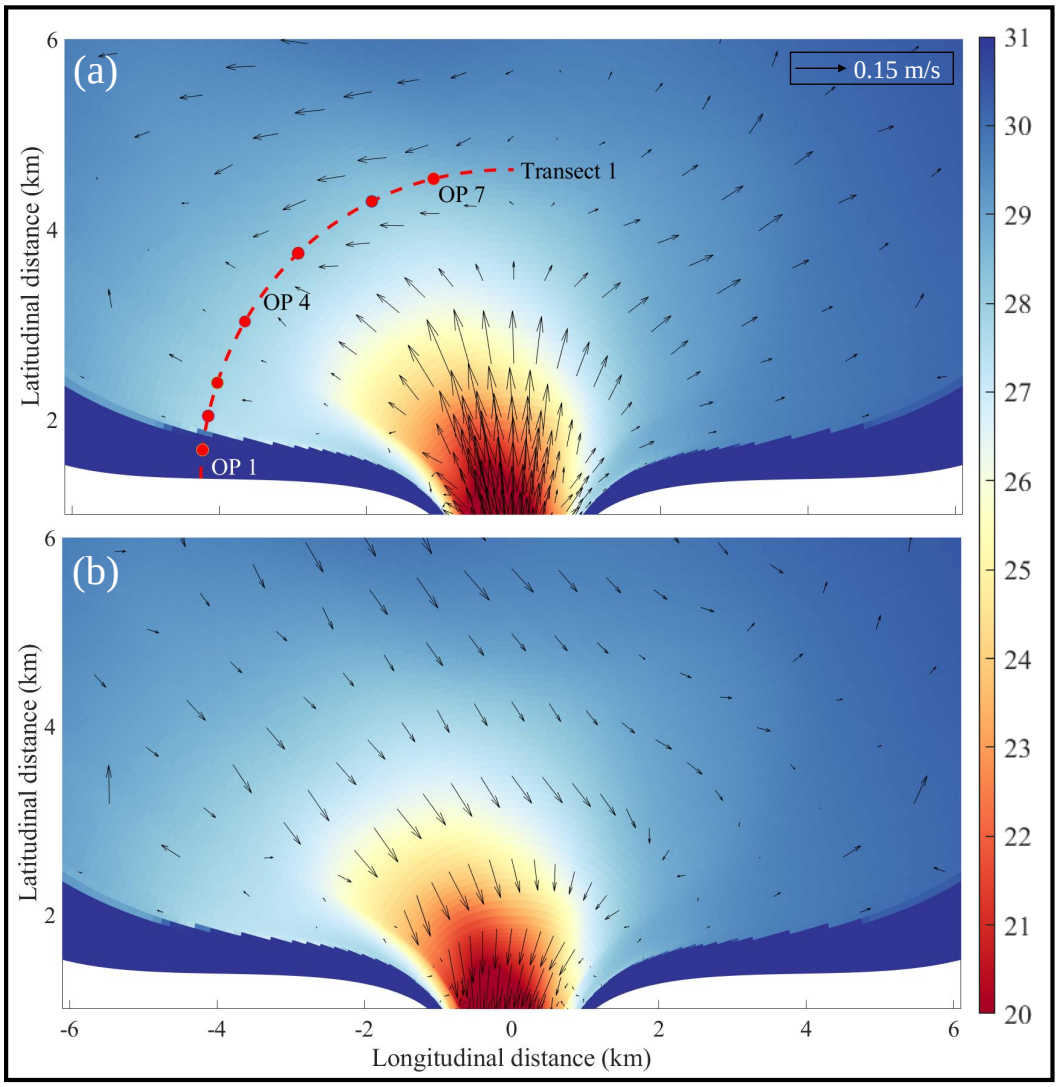

Figure 2.5: Distribution of residual flow velocity (black arrows) and residual salinity (colorbar) for (a) surface layer (b) bottom layer for vegetated simulation.

$$R_o = \frac{\sqrt{g'h}}{f}, \tag{2.11}$$

where,

$$g^{'} = \frac{\Delta\rho g}{\rho_o}, \tag{2.12}$$

where R_o is the baroclinic deformation radius, h is the depth at river mouth, reduced density and ρ_o is the initial water density and $g^{'}$ is the reduced gravity

and f is the Coriolis frequency (0.875 x $10^{-4}\,s^{-1}$ at -37^{o} latitude). For simulations involving tide, the evaluated baroclinic deformation radii inside and outside of the river plume were 10.96 km, and 29.7 km, respectively. However, while the deformation radius remained the same outside the plume for no-tide simulations, the radius decreased to 9.47 km inside the plume.

Table 2.1: Description of coordinates and different regions along transect 1 and transect 2 in the case of vegetated simulations.

Transect number	Along-transect position along the transect (x) in m (positive eastward)	Region of vegetation	Model observation points in region as shown in Figure 2.6c
Transect 1	-1250 $< x <$ -250	Forest	OP 1 - 2
	-250 $< x <$ 0	Forest Fringe	OP 3
	0 $< x <$ 1000	Tidal Flat	OP 4 - 7
Transect 2	-250 $< x <$ -150	Forest	OP 1 - 3
	-150 $< x <$ 0	Transition zone (over a $\sim$ 20 m-wide fringe region)	OP 4
	0 $< x <$ 100	Center of the river mouth	OP 5 - 7

2.4.3 Slack water asymmetry and sediment deposition patterns

Figure 2.6a shows that sediment deposition at the end of the model run for the case of spatially uniform bottom roughness resulted in an increase in the bed layer thickness (deposition) throughout transect 1 while the regions close to the river mouth experienced a decrease in the sediment bed layer thickness

(erosion). To investigate these patterns, we evaluated the tidal asymmetry (Table 2.2) for 7 model observation points along two transects at different distances from the river mouth in the model domain (Figure 2.6a).

In our study, to quantify the duration of high and low water slack tide, the magnitudes of bed shear stresses ($|\tau|$) were evaluated for two transects (near and away from the river mouth), and compared to the critical bed shear stress (τ_c). The slack duration asymmetry was then evaluated using the ratios of durations of high water and low water slack tide (T_{hw}/T_{lw}) for $|\tau| > \tau_c$, where ratios greater than 1 indicate a flood-directed asymmetry and ratios less than 1 indicated an ebb-directed asymmetry. Results displayed in Table 2.2 show that in the non-vegetated simulations, high water slack durations were longer than low water slack duration of tide throughout transect 1 (away from the river mouth), indicating flood dominance. However, near the river mouth (Transect 2), shallow inter-tidal regions (OP 1, 2) remained flood dominant (Table 2.2), whereas deeper regions (OP 3, 4, 5, 6, and 7) were ebb-dominant for both vegetated and non-vegetated simulations. The inter-tidal slack duration asymmetries evaluated for transect 1 in the vegetated simulations showed ebb-directed asymmetry in the fringe region (OP 3) while the forest and flats regions were flood dominant (Table 2.2). Also, slack water ratios in the vegetated simulations were higher (both flood and ebb-directed) in comparison to the non-vegetated simulations across both transects.

In the vegetated run, there was an increased level of bed layer thickness (sediment accretion) in the forests and over the mudflats; whereas the fringe area experienced a decrease in the thickness (sediment erosion) for a morphological bed evolution observed after four months (Figure 2.6c). These patterns of erosion and deposition observed are qualitatively consistent with field observations collected in the Firth of Thames (Lovett, 2017).

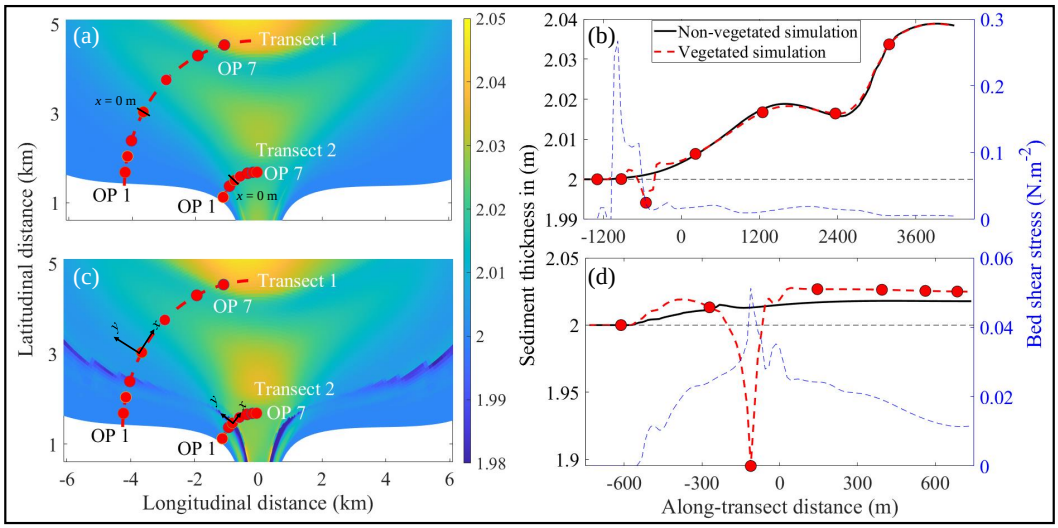

Figure 2.6: Predicted sediment deposition patterns for Non-vegetated (a) and Vegetated simulations (c). Along-transect sediment thickness along transect 1 (b) and transect 2 (d) for both the vegetated (thick red line) and non-vegetated (thin black line) simulations, respectively. In panels (b) and (d), blue thin dashed line shows the bed shear stress recorded for the vegetated simulation for transect 1 and transect 2, respectively. Thin black dashed lines show the initial sediment thickness in the model. Locations of transects 1 and 2 (red dashed lines) and model observation points 1 to 7 (red circles). x and y represent the along-transect and across-transect directions relative to the transect lines.

2.4.4 Momentum balances - Vegetated case

To analyze the major momentum contributors that influence the transport of sediment in the case of vegetated and non-vegetated simulations, momentum balances were evaluated in the across-transect and along-transect directions at two phases of the tidal cycle: (1) peak flood tide and (2) peak ebb tide inside the forest (at model observation point 2). Along the transects considered in this study, the dominant contributors towards the momentum balance were similar, with modest changes to the magnitudes across various stages of the tidal cycle. As the sediment plume attains maximum and minimum expansion during peak ebb and flood stages of the tidal cycle, respectively; hence balances during these tidal stages are presented. At this model observation point, water depths during peak flood and ebb flows were 0.65 m, and 0.5 m, respectively. To

Table 2.2: Tidal dominance evaluated in the case of vegetated simulations and non-vegetated simulations for model observations points (OP 1-7) along the transects 1 and 2. Ratios greater than 1 indicate flood dominance.

	Location	Non-Vegetated simulations		Vegetated simulations	
		Slack water ratio (T_{hw}/T_{lw})	Slack water asymmetry	Slack water ratio (T_{hw}/T_{lw})	Slack water asymmetry
Transect 1	Model OP 1	1.011	Flood	1.6	Flood
	Model OP 2	1.024	Flood	1.4	Flood
	Model OP 3	1.006	Flood	0.89	Ebb
	Model OP 4	1.01	Flood	1.01	Flood
	Model OP 5	1.02	Flood	1.10	Flood
	Model OP 6	1.146	Flood	1.13	Flood
	Model OP 7	1.175	Flood	1.20	Flood
Transect 2	Model OP 1	1.026	Flood	1.89	Flood
	Model OP 2	1.007	Flood	1.84	Flood
	Model OP 3	0.93	Ebb	0.99	Ebb
	Model OP 4	0.85	Ebb	0.98	Ebb
	Model OP 5	0.93	Ebb	0.97	Ebb
	Model OP 6	0.98	Ebb	0.98	Ebb
	Model OP 7	0.87	Ebb	0.87	Ebb

account for both the vertical transport of sediment and to consider the realistic hydro-morphodynamic phenomena, we evaluated momentum balances in the surface and bottom layers. The different terms in the momentum equation are shown in Table 2.3. As the focus of the present work is the interaction of the plume with vegetation, we presented the balances for the vegetated simulations here; however, the corresponding momentum balances for the non-vegetated simulations are included in Appendix A.

Table 2.3: Momentum components and their description ($\tau_{b,x}$, $\tau_{b,y}$ are the bed shear stress in x and y directions, respectively).

Along-transect momentum components	Across-transect momentum components	Textual description	Legend
$\frac{\partial U}{\partial t}$	$\frac{\partial V}{\partial t}$	Inertial Acceleration	A
$U\frac{\partial U}{\partial x}$	$U\frac{\partial V}{\partial x}$	Acceleration due to the streamwise momentum	B
$V\frac{\partial U}{\partial y}$	$V\frac{\partial V}{\partial y}$	Acceleration due to lateral momentum transport	C
$\frac{\omega}{h}\frac{\partial U}{\partial \sigma}$	$\frac{\omega}{h}\frac{\partial V}{\partial \sigma}$	Vertical advection of momentum	D
$-fV$	fU	Coriolis Acceleration	E
$g\frac{\partial \zeta}{\partial x}$	$g\frac{\partial \zeta}{\partial y}$	Acceleration due to the barotropic pressure gradient	F1
$g\frac{h}{\rho_0}\int_\sigma^0\left(\frac{\partial \rho}{\partial x}+\frac{\partial \sigma'}{\partial x}\frac{\partial \rho}{\partial \sigma'}\right)d\sigma'$	$g\frac{h}{\rho_0}\int_\sigma^0\left(\frac{\partial \rho}{\partial y}+\frac{\partial \sigma'}{\partial y}\frac{\partial \rho}{\partial \sigma'}\right)d\sigma'$	Acceleration due to the baroclinic pressure gradient	F2
F_x	F_y	Acceleration due to viscosity	G
$\frac{1}{h^2}\frac{\partial}{\partial \sigma}\left(v_V\frac{\partial u}{\partial \sigma}\right)$	$\frac{1}{h^2}\frac{\partial}{\partial \sigma}\left(v_V\frac{\partial v}{\partial \sigma}\right)$	Vertical diffusion of momentum	H
$\frac{\tau_{b,x}}{\rho h}$	$\frac{\tau_{b,y}}{\rho h}$	Bottom shear stress	I1

2.4.4.1 Dominant dynamics - Transect 1

Shallow regions inside the forest ($x \approx$ -1000 m to $x \approx$ -750 m) remained dry throughout the model simulations for this transect.

Surface layer Deep inside the forest ($x \approx$ -750 m to $x \approx$ -250 m) in the along-transect direction, the inertial acceleration (term A) and vertical diffusion of momentum (term H) balanced the barotropic pressure gradient (term F1) on the surface layer for transect 1 during the peak ebb tide (Figure 2.7a). In the along-transect direction, further away on the regions corresponding to fringe and mudflat ($x \approx$ -250 m to $x \approx$ +1000 m), the magnitudes of the accelerations significantly reduced (decreasing almost 10% of their magnitudes to that observed inside the forest), indicating a weak along-transect transport during the peak ebb tide. During the peak flood, the dominant balance in the regions corresponding to $x \approx$ -750 m to $x \approx$ +1000 m in along-transect direction, was between the barotropic pressure gradient ($\sim$-1.5x10^{-5} m.s^{-2}) and inertial acceleration ($\sim$1.25x10^{-5} m.s^{-2}, Figure 2.7c) in the along-transect direction with a modest contribution from the vertical diffusion of momentum ($\sim$0.25x10^{-5} m.s^{-2}).

During the peak ebb tide, the dominant balance deep inside the forest ($x \approx$ -750 m to $x \approx$ -250 m) in the across-transect direction, was between the inertial acceleration, the Coriolis acceleration balancing the barotropic pressure gradient and lateral momentum exchange. Across the fringe region ($x \approx$ -250 m to $x \approx$ 0 m), while the magnitudes of these components significantly reduced (almost halved to that observed deep inside the forest), additional contributions from terms such as streamwise momentum exchange, and vertical advection indicated the highly complex nature of dynamics in the fringe region. From $x >$ 250 m, the momentum balance existed between the streamwise momentum exchange ($\sim$0.25x10^{-5} m.s^{-2}), lateral momentum exchange ($\sim$0.25x10^{-5} m.s^{-2}), baroclinic pressure gradient ($\sim$0.25x10^{-5} m.s^{-2}), and the inertial acceleration

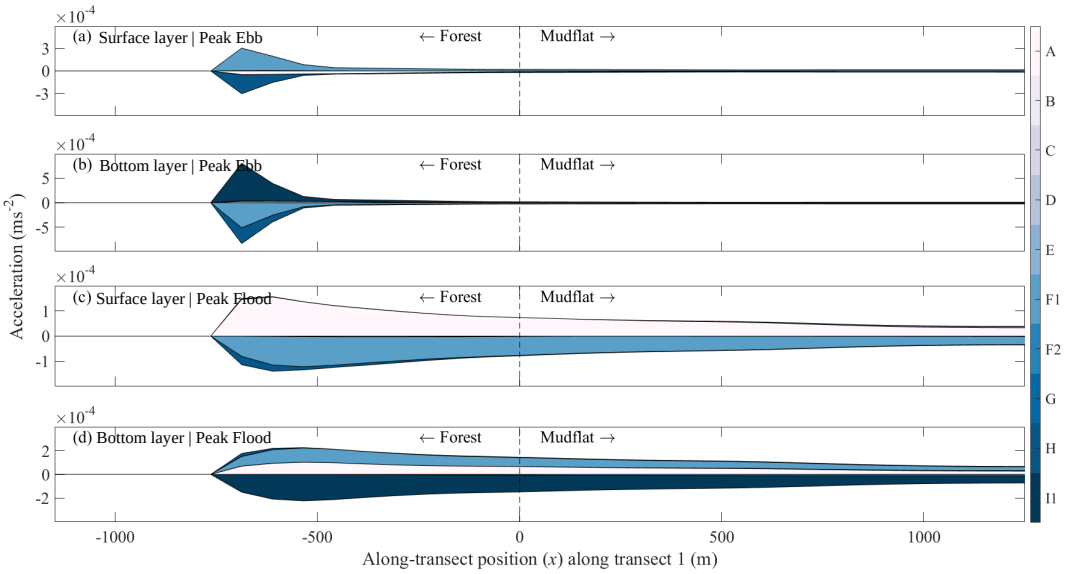

Figure 2.7: Along-transect momentum balance for transect 1 for vegetated simulations (spatially varying roughness). Panels (a) and (b) show the balances at the peak ebb of the tidal cycle in the surface and bottom layers, respectively. Panels (c) and (d) show the balances recorded for peak flood in the surface and bottom layers, respectively. The cumulative sum of positive and negative momentum components (colors show the individual momentum components represented in Table 2.3).

($\sim$-0.5x10^{-5} m.s^{-2}) and the Coriolis acceleration ($\sim$-0.25x10^{-5} m.s^{-2}, Figure 2.8a). During the peak flood tide, the dominant balances deep inside the forest and across the fringe region ($x \approx$ -750 m to $x \approx 0$ m) in the across-transect direction were between the inertial acceleration (term A) and the barotropic pressure gradient (term F1, Figure 2.8c) with modest contributions from the lateral momentum exchange and vertical diffusion in the $+x$ and $-x$ directions, respectively. Further out on the mudflat ($x \approx 0$ m to $x \approx 1000$ m), momentum balance was between the barotropic pressure gradient ($\sim$-0.5x10^{-5} m.s^{-2}) and the inertial acceleration ($\sim$0.5x10^{-5} m.s^{-2}).

Bottom layer Deep inside the forest ($x \approx$ -750 m to $x \approx$ -250 m), during the peak ebb tide, bed shear stress ($\sim$5x10^{-4} m.s^{-2}) balanced the barotropic pressure gradient ($\sim$-2.5x10^{-4} m.s^{-2}) and the vertical diffusion of momentum ($\sim$-2.5x10^{-4} m.s^{-2}). Across the fringe region ($x \approx$ -250 m to $x \approx 0$ m), the

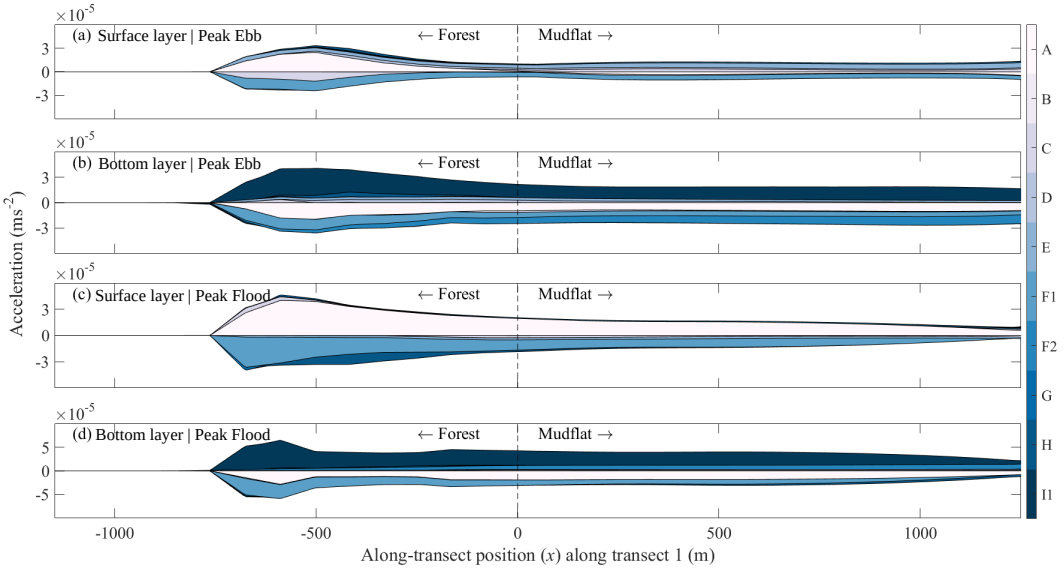

Figure 2.8: Across-transect momentum balance for transect 1 for vegetated simulations (spatially varying roughness). Peak ebb of tidal cycle (a) surface layer and (b) bottom layer. Peak flood of tidal cycle (c) surface layer, and (d) bottom layer. The cumulative sum of positive and negative momentum components (colors show the individual momentum components represented in Table 2.3).

barotropic and baroclinic pressure gradients, balanced vertical advection of momentum and the bed shear stress. Momentum balances evaluated during the peak flood stage of the tidal cycle were similar to those evaluated for the peak ebb stage inside the forest on the bottom layer. Throughout the transect ($x \approx$ -750 m to $x \approx +250$ m), the bed shear stress (term I1, Figure 2.7d) balanced the baroclinic pressure gradient (term F2, Figure 2.7d), inertial acceleration (term A) with modest contribution from the vertical diffusion of the momentum (term H).

In the across-transect direction, during the peak ebb tide (Figure 2.8b), bed shear stress ($\sim 3\text{x}10^{-5}$ m.s^{-2}) balanced the inertial acceleration ($\sim$-1.5x10^{-5} m.s^{-2}) and the barotropic pressure gradient ($\sim$-1.5x10^{-5} m.s^{-2}). Across the fringe region ($x \approx$ -250 m to $x \approx 0$ m), bed shear stress ($\sim 1.5\text{x}10^{-5}$ m.s^{-2}), the Coriolis acceleration ($\sim 0.25\text{x}10^{-5}$ m.s^{-2}) balanced the inertial acceleration ($\sim$-0.5x10^{-5} m.s^{-2}) and the barotropic pressure gradient ($\sim$-0.5x10^{-5} m.s^{-2}) with

an additional contribution of the baroclinic pressure gradient ($\sim$-0.75x10^{-5} m.s^{-2}). These contributions remained the same until the mudflat ($x \approx +250$ m) where the magnitudes almost halved (Figure 2.8d). On the mudflat ($x \approx +250$ m), while the dominant balances remained the same, the magnitudes of each component were approximately halved.

2.4.4.2 Dominant dynamics - Transect 2

Surface layer In the along-transect direction, deep inside the forest, lateral momentum exchange (term C) and the barotropic pressure gradient (term F1) balanced the inertial acceleration (term A), streamwise momentum exchange (term B), and the Coriolis acceleration (term E, Figure 2.9a) during the peak ebb stage of the tidal cycle for this transect. However, near the transition region (from $x \approx$ -50 m to $x \approx 0$ m), the barotropic pressure gradient ($\sim$-1.5x10^{-4} m.s^{-2}), balanced the vertical diffusion of momentum ($\sim$0.75x10^{-4} m.s^{-2}), Coriolis acceleration ($\sim$0.25x10^{-4} m.s^{-2}), lateral momentum exchange ($\sim$0.25x10^{-4} m.s^{-2}), and vertical advection of momentum ($\sim$0.25x10^{-4} m.s^{-2}, Figure 2.9a). However, near the transition region (from $x \approx$ -50 m to $x \approx$ 0 m), there were two dynamic balances. In particular, from the region $x \approx$ -50 m to $x \approx$ -25 m, the barotropic pressure gradient ($\sim$-1.5x10^{-4} m.s^{-2}), balanced the vertical diffusion of momentum ($\sim$0.75x10^{-4} m.s^{-2}), Coriolis acceleration ($\sim$0.25x10^{-4} m.s^{-2}), lateral momentum exchange ($\sim$0.25x10^{-4} m.s^{-2}), and vertical advection of momentum ($\sim$0.25x10^{-4} m.s^{-2}, Figure 2.9a). Along the transition zone (from $x \approx$ -25 m to $x \approx 0$ m), acceleration due to viscosity (term G, $\sim$-1.5x10^{-4} m.s^{-2}), Coriolis acceleration (term E, $\sim$-0.1x10^{-4} m.s^{-2}) balanced the barotropic pressure gradient (term G, $\sim$1.5x10^{-4} m.s^{-2}) with modest contributions from the inertial acceleration, streamwise and lateral momentum exchanges (Figure 2.9a). Further along this transect ($x > 0$ m), the magnitudes of all the terms significantly reduced in this region (to almost one-third to that observed in the forest interior) where the dominant balance was between the Coriolis acceleration and the lateral momentum exchange with

a small contribution from the inertial acceleration. This presence of Coriolis acceleration in this area (especially around the region designated as center of the river mouth) caused the westward deflection of the river plume as observed in the Figure 2.4. During the peak flood tide, deep inside the forest region (from $x \approx$ -250 m to $x \approx$ -175 m), both the barotropic (term F1) and baroclinic pressure gradients (term F2) balanced the inertial acceleration (term A, Figure 2.9c). In the regions corresponding to $x \approx$ -175 m to $x \approx +100$ m of this transect, the balances remained same as observed in the case of the peak ebb tide.

During the peak ebb tide, in the across-transect direction, inside the forest interior (from $x \approx$ -250 m to $x \approx$ -50 m), the acceleration due to viscosity ($\sim$ 1.7x10^{-4} m.s^{-2}) and the inertial acceleration ($\sim$ 0.4x10^{-4} m.s^{-2}) balanced the lateral momentum exchange ($\sim$ -1x10^{-4} m.s^{-2}) and the barotropic pressure gradient ($\sim$ -1x10^{-4} m.s^{-2}) with a small contribution from the streamwise momentum exchange ($\sim$ -0.1x10^{-4} m.s^{-2}). This trend remained the same throughout this transect with an additional contribution by the vertical advection (term D) and the streamwise momentum exchange (term B) near the transition zone (from $x \approx$ -50 m to $x \approx +100$ m). Throughout transect 2 (from $x \approx$ -250 m to $x \approx +100$ m), the barotropic pressure gradient balanced the inertial acceleration during the peak flood tide in the across-transect direction (Figure 2.10c). However, in the transition zone (from $x \approx$ -50 m to $x \approx$ -15 m), additional contributions from the acceleration due to viscosity and the vertical advection of momentum in $+y$ and $-y$ directions respectively, completed the balance.

Bottom layer During the peak ebb tide (Figure 2.9b), the baroclinic pressure gradient ($\sim$ 3x10^{-4} m.s^{-2}) and the vertical advection of momentum ($\sim$ 0.5x10^{-4} m.s^{-2}) balanced bed shear stress ($\sim$ -3.35x10^{-4} m.s^{-2}) with a small contribution of acceleration due to viscosity ($\sim$ -0.15x10^{-4} m.s^{-2}) inside the

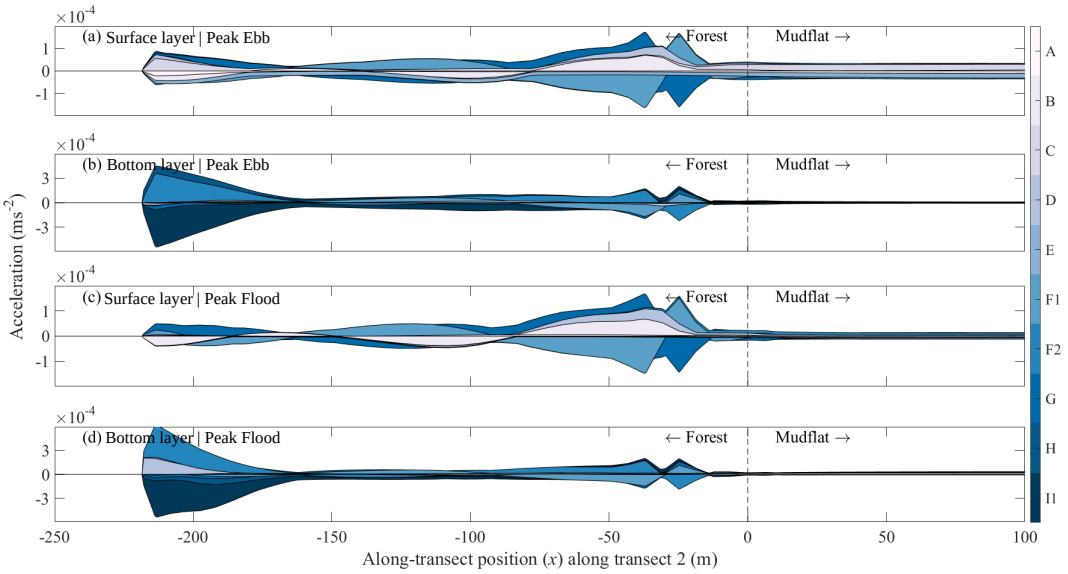

Figure 2.9: Along-transect momentum balance for transect 2 for vegetated simulations (spatially varying roughness). Peak ebb of tidal cycle (a) surface layer and (b) bottom layer. Peak flood of tidal cycle (c) surface layer, and (d) bottom layer. The cumulative sum of positive and negative momentum components (colors show the individual momentum components represented in Table 2.3).

forest interior ($x \approx$ -250 m to $x \approx$ -150 m). Further along this transect (from $x \approx$ -150 m to $x \approx$ -50 m), acceleration due to viscosity ($\sim 0.1\text{x}10^{-4}$ m.s^{-2}) and baroclinic pressure gradient ($\sim 0.5\text{x}10^{-4}$ m.s^{-2}), balanced the bed shear stress ($\sim$-0.6x10^{-4} m.s^{-2}). Near the transition zone ($x \approx$ -50 m to $x \approx$ +50 m), the Coriolis acceleration ($\sim 0.5\text{x}10^{-4}$ m.s^{-2}) and the acceleration due to viscosity of the order $\sim 0.5\text{x}10^{-4}$ m.s^{-2} along with the baroclinic pressure gradient ($\sim 0.5\text{x}10^{-4}$ m.s^{-2}) balanced the barotropic pressure gradient ($\sim$-1.5x10^{-4} m.s^{-2}, Figure 2.9b). In the along-transect direction of transect 2, the baroclinic pressure gradient ($\sim 2.5\text{x}10^{-4}$ m.s^{-2}) and the vertical advection due to momentum ($\sim 1\text{x}10^{-4}$ m.s^{-2}) balanced the bed shear stress ($\sim$-3.5x10^{-4} m.s^{-2}) during the peak flood (Figure 2.9d). The contribution of the vertical advection due to momentum (term D, Figure 2.9d) was seen for a few 100 meters of the forest interior (from $x \approx$ -250 m to $x \approx$ -180 m) but eventually it became insignificant near the transition zone, where instead there existed a non-zero contribution from the barotropic pressure gradient. Near the center of the river mouth

($x > 0$), the balance remained between the barotropic and baroclinic pressure gradients (Figure 2.9d).

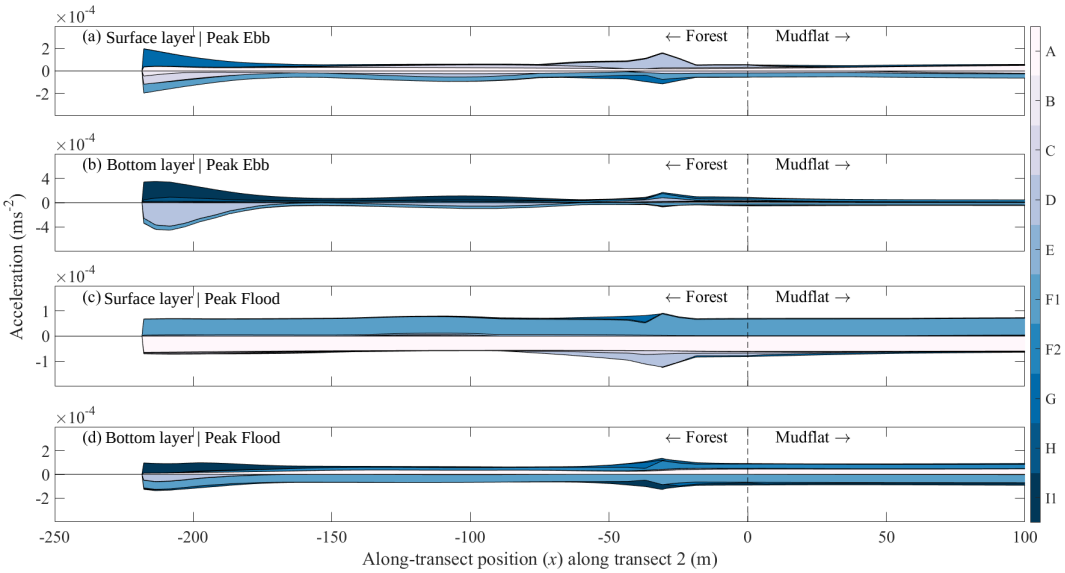

Figure 2.10: Across-transect momentum balance for transect 2 for vegetated simulations (spatially varying roughness). Peak ebb of tidal cycle (a) surface layer and (b) bottom layer. Peak flood of tidal cycle (c) surface layer, and (d) bottom layer. The cumulative sum of positive and negative momentum components (colors show the individual momentum components represented in Table 2.3).

The across-transect momentum balance evaluated for the peak ebb (Figure 2.10b) was distributed between the baroclinic pressure gradient (term F2, $\sim$-3.75x10^{-4} m.s^{-2}) and viscous term (term G, $\sim$-0.25x10^{-4} m.s^{-2}) in the negative y-direction, and bed shear stress (I1, $\sim$4x10^{-4} m.s^{-2}) in the positive y direction, inside the forest interior (from $x \approx$ -250 m to $x \approx$ -70 m). In the transition zone, the principal balance was achieved by the same terms except that viscous term was now replaced by vertical advection of momentum instead. This balance existed throughout the transition zone and center of the river mouth (Figure 2.10b). During the peak flood, in the across-transect direction, barotropic pressure gradient and the Coriolis acceleration balanced the bed shear stress throughout the forest interior ($x \approx$ -250 m to $x \approx$ -150 m). In the regions ($x \approx$ -150 m to $x \approx$ -50 m), the dominant balance was be-

tween the baroclinic pressure gradient ($\sim$0.5x10^{-4} m.s^{-2}), inertial acceleration ($\sim$0.5x10^{-4} m.s^{-2}) and the barotropic pressure gradient ($\sim$-1x10^{-4} m.s^{-2}). Near the transition zone ($x \approx$ -50 m to $x \approx$ +50 m), the dominant balance remained between the baroclinic pressure gradient ($\sim$2.4x10^{-4} m.s^{-2}) and bed shear stress ($\sim$-2.4x10^{-4} m.s^{-2}, Figure 2.10d).

2.5 Discussion

We presented idealized model simulations to elucidate the sediment transport and deposition resulting from the interaction of river plumes with vegetation.

2.5.1 Plume development (without and with tides)

2.5.1.1 River flow only (without tides)

Model simulations forced by river flow only (without tides) showed a large portion of plume expansion spreading northward into the central domain due to the absence of opposing currents. These results are in agreement with Wu et al. (2011) who evaluated the influence of tide on the Changjiang River plume and found that when forced by river flow alone, the associated outflow exhibits eddies and grows with time.

Horner-Devine et al. (2015) describes the plume's initial plume expansion region and boundaries as the near-field region and frontal region, respectively. In our plume, similar to (Horner-Devine, 2009; Fong and Geyer, 2002; Hetland, 2005), the effect of Coriolis on the plume in the near-field region (rotation to the left) and expansion of frontal region over time was evident in an otherwise symmetric domain. In our model simulations without tides, the vertical structure of the plume in the absence of tides resembles geostrophically balanced Margulus front (Fong and Geyer, 2002; Yao et al., 2016; Schiller and Kourafalou, 2010; Mazzini and Chant, 2016; Mestres et al., 2010).

2.5.1.2 River flow and tidal forcing

As the plume exits from the river mouth, near the mouth, an anticyclonic eddy (bulge) is formed owing to different density and current speeds inside and outside the river (Figure 2.4a). This non-linear anti-cyclonic circulation near the mouth of rivers has been seen in many plume studies (Chant et al., 2008; Horner-Devine, 2009; Marsaleix et al., 1998; Ruddick et al., 1994; Rong and Li, 2012). The extent of this freshwater plume was strongly modified by the tides. In particular, during the ebbing tide, the plume extends up to 4 km into the model domain. During the flooding tide, the plume is pushed completely into the river, in a similar manner to numerical model observations of Kourafalou et al. (1996).

The tidal effects observed in our model simulations were evident in the extent of the freshwater plume and its rotation. Baroclinic deformation radii evaluated inside the plume were significantly different for model simulations with and without tides. In particular, the radius evaluated inside the plume increased compared to the model run in the absence of tides. This anticyclonic bulge was previously reported in Chant et al. (2008) who attributed this difference to the augmentation of the bulge region often caused by tidally driven eddies. Cole and Hetland (2016) previously studied the effects of rotation and river discharge on the mixing in plumes and established that increased rotation of plumes limits lateral expansion and suppresses its shear mixing. Results such as these as observed in our study can be attributed to the increased sediment in the vicinity of the river.

The residual tidal currents showed that the plume reverses its direction with depth (Figure 2.5). Closer to the river mouth, in the surface and bottom layers, residual currents (Figure 2.5a) were directed towards the forest, which can explain the deposition of sediment in this region (2.6a and c). Near the transition zone, while the residual vectors were directed towards the shallow

region in the surface layer of the domain, these were directed offshore in the bottom layer. Furthermore, residual velocity magnitudes were higher on the bottom layer than the surface layer in this region for both the non-vegetated and vegetated model simulations. These model observations along with the presence of barotropic pressure gradients directed offshore (Figure 2.9 and A.3) can explain the modeled sediment deposition patterns in this region. Such reversal of currents on the surface and bottom layers, attributed to tidal rectification, has been seen in previous plume studies such as Xuan et al. (2016); Chao (1990).

2.5.2 Non-vegetated run

In the non-vegetated simulation, there was an increase in sediment bed layer thickness in both the upper and central domain. However, the lower domain, which includes both river and river boundary, recorded erosion at the edges of the domain in the latitudinal direction and deposition at the center. This result is similar to that observed by Fagherazzi et al. (2015) who, in their 1-D modeling of the river jet, which attributes this deposition to a change in the flow speed at the river mouth, which leads to sediment suspension and hence erosion.

Tidal asymmetry patterns evaluated for non-vegetated simulations showed stronger flood dominance away from the river mouth (Transect 1) than near the river mouth (Transect 2). This result is consistent with Cheng et al. (2010) who showed using an analytical model that asymmetric tidal mixing decreases towards the river mouth and the large asymmetry leads to residual currents landward direction if the tide is flood dominant. The changes observed in our model study related to tidal dominance indicate that the net flux of sediment varies across the domain, thereby causing sediment deposition or erosion. Transect 2 (near the river mouth) exhibited ebb dominance throughout the majority of the transect except for shallow regions, thus indicating that the flux

of suspended sediment was directed landward, which increased the sediment bed level thickness in the shallower regions (Figure 2.6d).

2.5.3 Vegetated run

The presence of vegetation substantially altered the sediment deposition patterns observed in our model simulations. The drag induced by simulated vegetation slowed currents and altered shear stresses. Along with the changes in the magnitude of bed shear stress, the momentum balances for the forest fringe area showed more complexity than that of the forest and flat regions. Mullarney et al. (2017), in their field study conducted in a *Sonneratia caseolaris*, dominated mangrove forest in the Mekong Delta, Vietnam reported the highly dynamic nature of fringe region relative to inside the forest. They observed that incident tidal currents on the forest region modify the momentum balance inside the fringe due to the strong advection of momentum in this region. This result was also reflected in our study: momentum balances at both peak ebb and flood cases were considerably more complex in both across and along-transect balances inside the fringe than inside the forest or the mudflat, both on the east and west side of the domain (Figure 2.9).

The influence of friction on tides can often cause the tide to distort and create asymmetric tides (Friedrichs and Aubrey, 1994). This impact of friction is evident in the momentum balances close to the river (Transect 2, Figures A.3 and A.4). Along-transect momentum balances were largely dominated by the balance between the pressure gradient and the inertial accelerations during the flood on the surface layer and between the barotropic and baroclinic terms in the bottom layer. During the peak ebb, a dominance of the vertical advection and diffusion of momentum terms in the central region of the plume indicated the sediment would remain in suspension. However, due to the locally lengthened high water slack period in this region, the suspended sediment is advected in the along-transect direction ($-x$ and $+x$ directions),

thereby creating a delta near the river mouth.

The deposition patterns in the vegetated run were different from that of the non-vegetated simulation. Here, deposition occurs inside the forest and flat regions while fringe regions observed erosion of sediment (Figure 2.6). This result is consistent with Bryan et al. (2017) who, in their modeling study of mangroves in the Mekong Delta, Vietnam, established that changes in the depth profile of transects alter the tidal asymmetry observed. This change is attributed to the progressive nature of the tidal currents and their interaction with the vegetation.

2.5.4 Momentum balances

The momentum balances for both transects showed a dominance of the barotropic pressure gradient, streamwise momentum exchange, and inertial acceleration inside the forest interior. These observations are similar to Mossa et al. (2017) who investigated the influences of vegetation on a turbulent jet through theoretical and experimental methods. They found that the presence of the cylindrical arrays of vegetation greatly reduces the diffusive and advective capabilities of the jets in the longitudinal direction due to the presence of streamwise flow around the vegetation. In our study, the presence of significant vertical advection and diffusion components of momentum in the fringe region further indicate a mechanism through which the sediment present in this region is distributed. In particular, sediment is lifted into suspension by the vertical advection and diffusion components, while the across-transect pressure gradient helped distribute a major part of this sediment in the across-transect direction (-y and +y in Figure 2.6). The Coriolis acceleration also promoted the transfer of sediments in the along-transect directions (-x and +x), thereby leading to sediment erosion in the fringe region. The dominant balances in the along-transect directions (-x and +x) remained similar for both the transects. However, the individual terms in the momentum balances were around

10 times higher in terms of magnitude for transect 2 compared to that of transect 1. This increase could explain the relatively higher deflection of the plume near the river mouth than that of the far-field zone of the plume (Figure 2.4a and b).

2.5.4.1 Differences between surface and bottom flows

In the surface layer, modeled momentum balances in our study showed a balance between barotropic pressure gradient, baroclinic pressure gradient, and the Coriolis acceleration during peak ebb and flood stages tidal cycle. In the bottom layer, the dominant balance is again between the Coriolis acceleration, which is balanced by bed shear stress. This result is similar to that of Ren and Wu (2014), who using a numerical model of the Pearl River plume, who found that the Earth's rotation drives the transport in the mid-field region of the plume. According to Horner-Devine et al. (2015), the mid-field region of a plume is a transition zone into a far-field plume from a high-speed near-field zone, and hence forms the region where the momentum dynamics transition into a balance between the inertial acceleration and the barotropic pressure gradient in the far-field region.

In the mid-field region of the plume (the region between transect 1 and 2), magnitudes of the evaluated balances were found to be lower compared to those of transect 1 and transect 2. Horner-Devine et al. (2015), previously explained this reduced momentum in the mid-field regions to the dominance of the Coriolis acceleration in this region in comparison to other momentum components, thereby arresting the spreading of the plume. These reduced magnitudes in the momentum balance can explain the reduced sediment erosion in the regions between transects 1 and 2 (Figure 2.6c). Additionally, away from the river mouth in the plume's far-field region (Transect 1), the magnitudes of momentum balance and the sediment erosion in the fringe region are larger again due to increased tidal influence in this region. These increased

magnitudes have been previously observed in various studies such as Chen et al. (2009); Horner-Devine (2009); Chant et al. (2008).

Closer to the river mouth (Transect 2), the presence of the inertial acceleration term along with the barotropic pressure gradient term at the center of the river mouth in the surface layer indicated the sediment distribution from the plume into the domain. This sediment is imported to the west side of the domain due to Coriolis acceleration in the along-transect direction (-x direction). In the bottom layer, drag coupled with the tide's ebb dominance plays a significant role in trapping most of this sediment near the river mouth (Figure 2.6a and c). The presence of vertical advection and the diffusion components indicate a mechanism through which the sediment from the bed is uprooted throughout the tidal cycle closer to the river, and surface layer balances such as barotropic pressure gradient and inertial accelerations help transport the majority of this sediment into the across-transect directions of the domain. Also, during the ebb tide, when the plume is at its maximum expansion, barotropic and baroclinic pressure gradients and the Coriolis acceleration helped deliver a significant part of river sediment to the forest and mudflat regions on the east-west sides of the domain. These dynamics hold for both the uniform and spatially varying roughness near the river mouth.

In the far-field region of the river plume, modeled momentum balances showed a dominance of the inertial acceleration and barotropic pressure gradients throughout the tidal cycle in the surface layer. Despite the reduction in the Coriolis acceleration in this region, the inertial and barotropic pressure gradients help transport this sediment into the forest and mudflat regions. These effects in salt marshes have been previously observed in Zhang et al. (2019). Analysis of bottom layer dynamics showed a different mechanism of sediment transport in the far-field region altogether. In particular, bed shear stress and barotropic pressure gradient, coupled with flood dominance in this

region due to reduced water depths and velocities, helped transport this sediment into the domain's shallow regions.

2.5.4.2 Differences in dynamics from east to west and their impact on the sediment transport

Momentum balances on the east side of the domain showed that within the forest, the principal balance was between the barotropic pressure gradient and inertial acceleration in the surface layer, while the balance was between inertial acceleration and the bed shear stress in the bottom layer. As expected, Coriolis acceleration was not a dominant contributor to the momentum balance evaluated for the east side of the mangroves. On the west side, balances are similar, but the contribution from the Coriolis acceleration is larger, which contributes to enhanced sediment deposition and erosion on the west side compared to the east side. These results are similar to Van Leeuwen and De Swart (2002) who found that advective fluxes become relatively more important with decreasing contributions of the Coriolis acceleration.

2.5.5 Summary

Figure 2.11 summarizes the modeled momentum balances and tidal asymmetries in each of the domain's distinct regions. The balances, coupled with the asymmetric tidal patterns, alter these regions' deposition and erosion patterns. In particular, the flood dominant forest increases the time sediment stays in suspension, and further delayed drainage inside this region due to vegetation drag results in sediment deposition inside the forest. Inside the fringe region, momentum balances indicate a process by which the vertical advection and diffusion components suspend the sediment present in this region into suspension. The across-shore pressure gradients and inertial acceleration help distribute this sediment in the $\pm x$ directions of the domain.

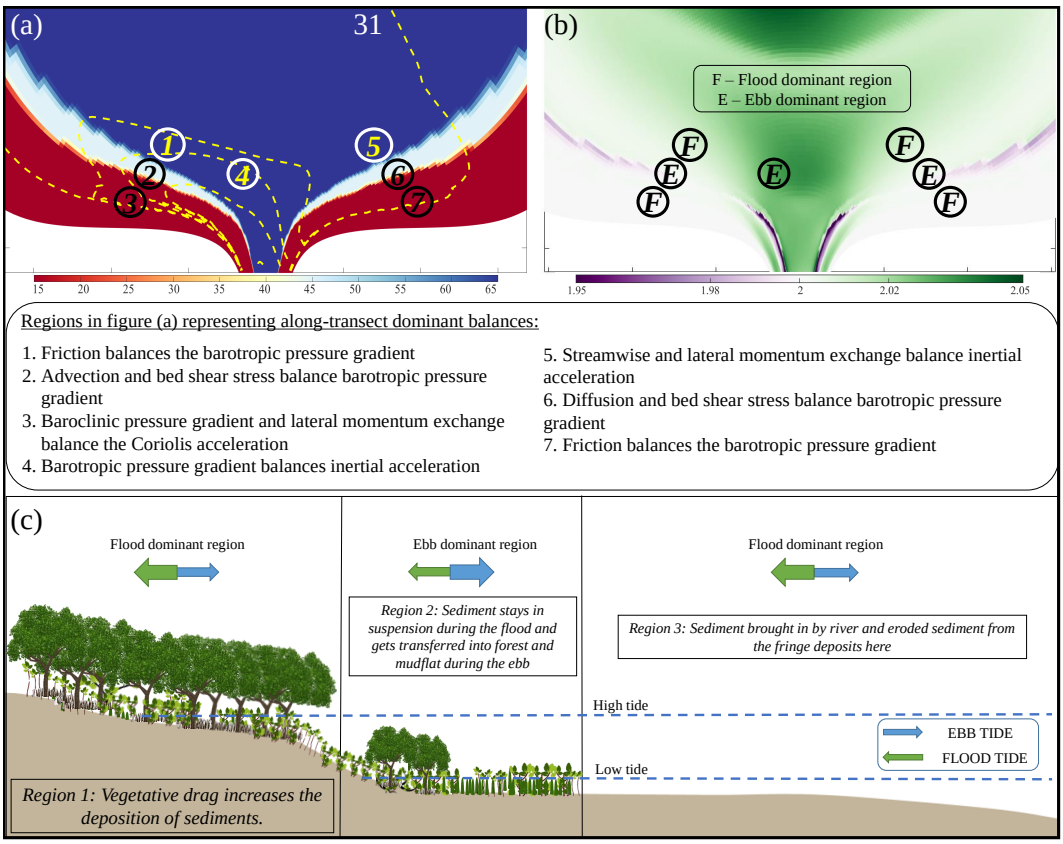

Figure 2.11: Schematic showing momentum balances and tidal asymmetry patterns recorded in the different regions. Panel (a) shows the dominant balances within the model domain, (b) tidal asymmetry patterns, and (c) shows the conceptual diagram of various momentum contributors in different environments of a mangrove forest and their effects on the net transport of the sediment. Colorbars in panels (a) and (b) show the Chézy friction coefficient used in the model and modeled deposition patterns in the vegetated run, respectively. Contour lines (thick dashed yellow lines) in Panel (a) show modeled surface layer salinities with a contour interval of 2 ppt at the peak flood and ebb stages of the tidal cycle, respectively.

2.6 Conclusions

We use a 3-D idealized morphological model to explore the sediment patterns resulting from the interaction of buoyant river plumes with uniform vegetation. The modeled river plume, forced by a steady river discharge, showed that vegetated areas influence the sediment patterns as the underlying dynamics are altered due to the drag produced by the vegetation. Comparing the momentum balance on the surface layer for each of the model runs (non-

vegetated and vegetated run) showed that force balance between barotropic pressure gradient and inertial acceleration remains dominant in plume regions. However, the importance of inertial term was substituted by bed shear stress in the cases of the vegetated run in the bottom layer, indicating that vegetative drag essentially helped to slow the movement of sediment offshore. This result is similar to that reported by Fagherazzi et al. (2015) who observed the changes in hydro-morphodynamics of a jet of water exiting a river mouth, and our study can be seen as an extension to their 1-D modeling study. Results also show that the fringe environment is critical to sediment deposition and, eventually, the seaward extension of mangroves (Balke et al., 2013; Mullarney et al., 2017).

The results described in this paper are highly relevant to our understanding of how vegetation influences sediment deposition patterns. In some locations, mangrove forests have shown to help mitigate coastal erosion by attenuating the waves and trapping sediment to keep pace with sea-level rise (Kumara et al., 2010; Walsh and Nittrouer, 2004; Krauss et al., 2014). These ecosystems have also shown to be in rapid decline across the world due to various reasons such as climate change, population growth, and urbanization (Giri et al., 2011). In contrast to other locations, mangroves in New Zealand have increased over the early 1940s, which is attributed to increased sediment deposition (Horstman et al., 2018). Understanding the buoyant river plumes with vegetation, and tidal currents due to their ability to change the flow dynamics, are pivotal in investigating sediment patterns. In addition, spatially varying open coast effects such as winds and waves play a role in further controlling sediment patterns in the presence of vegetation. These dependencies and effects will be explored in future work.

Chapter 3

The influence of river plume discharge and winds on sediment transport into a coastal mangrove environment

Contribution of authors

Chapter 3 duplicates a paper of the title "The influence of river plume discharge and winds on sediment transport into a coastal mangrove environment" by Hemanth Vundavilli, Julia C. Mullarney, and Iain T. MacDonald, which was submitted to *Estuaries and Coasts* in 2022. The majority of text and figures are identical to the initially submitted version, except for the relabeling of figures, tables, equation numbers, and changes as suggested by the examiners of this thesis and the ongoing peer-review process. Along with development of the idealized numerical model using Delft3D, I wrote MATLAB scripts to process and analyze the model data. Along with the preparation of initial and subsequent drafts, I prepared all the figures for this manuscript. My co-authors, Julia C. Mullarney and Iain T. MacDonald edited my drafts along with providing helpful comments and direction.

Abstract

We investigated the influence of wind and river discharge on sediment transport from a river plume into a vegetated coastal environment. Flows and sediment transport patterns are explored using an idealized Delft3D numerical model. Total sediment transport and the relative contributions of riverine and bed-sourced sediment into the forest are assessed using a transect along the edge of the forest region, which was represented with an enhanced roughness coefficient. When the river discharge was varied, the dominant contributors to the total sediment transport changed along the regions of the river plume. In particular, the total sediment transport in the near-field region has equal contributions by both the riverine and bed-sourced sediments. However, farther away in the mid- and far-field region of the plume, bed-sourced sediment remains the dominant contributor towards total sediment transport. As the freshwater and sediment-laden plume spread out at the river mouth (the near field region), across-transect sediment loads were directed into the mangrove forest, indicating an accretionary environment consistent with satellite observations. The mass loads increased with the river discharge for small to medium discharges (0 - 280 $\mathrm{m^3.s^{-1}}$); however, increasing the discharge further did not substantially alter the sediment mass loads deposited in the forest region. For the large discharge events, owing to the high riverine momentum carried within the near-field region, the sediment plume was sufficient to push sediment through and out of the forest front. Total transport fluxes revealed that 5 $\mathrm{m.s^{-1}}$ wind velocities could alter the sediment patterns in the far and mid-field region of the river plume. However, larger wind velocities 10 $\mathrm{m.s^{-1}}$ were able to modify the sediment transport in the near-field region of the river

plume despite strong river momentum. The model results further reveal that in the presence of strong winds, a combined effect of the riverine discharge, Coriolis, bed-shear stress, and winds influence the total sediment mass transport. In the presence of strong winds, sediment transport in the far-field region is controlled by a combination of tidal effects and wind stress in case of easterly winds. Alternatively, in the case of westerly wind directions, when the river plume is pushed away from the forest, tidal effects control the total transport.

3.1 Introduction

Mangroves are often the predominant vegetation growing along the coastlines in tropical and subtropical regions. In addition to providing valuable ecosystem services (e.g. Barbier et al., 2011; Sheaves et al., 2015), these salt-tolerant trees play a critical role in the morphological evolution of rivers, estuaries, and tidal environments. With extensive growth in the intertidal zones, mangroves can influence hydrodynamics within the aquatic environments by altering velocity fields (Nepf, 2012a; Mullarney et al., 2017), generating small-scale turbulence (Furukawa and Wolanski, 1996; Norris et al., 2019), attenuating wave energy (Furukawa and Wolanski, 1996; Mazda et al., 2006; Henderson et al., 2017), and reducing storm surges (Montgomery et al., 2019). Interactions between flows and mangroves' aerial root systems have been shown to facilitate both the deposition and erosion of sediment (Woodroffe, 1992; Norris et al., 2021; Temmerman et al., 2007) depending on environmental conditions and vegetation parameters such as stem spacing, densities and geometries (Nepf, 2004; Li et al., 2014).

The small (sub-meter) scale spatial heterogeneity of the vegetation-induced turbulence and associated variability in sediment resuspension (Temmerman et al., 2007; Zong and Nepf, 2012; Chen et al., 2012) has been shown to influence morphological characteristics at the estuary scale. Mangrove roots (pneu-

matophores) generate stem-scale turbulence through the processes of vortex shedding and generation of eddies (Norris et al., 2019). Using field observations from a wave-influenced mangrove coastline in the Mekong Delta, Norris et al. (2017) explored the relationships between the density of mangrove roots (pneumatophores), and enhanced turbulence at the forest fringe (the transition between mudflat and vegetated area), which were found to act as a control on sediment size distributions, and erosion and accretion regimes (Fricke et al., 2017; Mullarney et al., 2017).

Tidal asymmetry is one of the principal mechanisms that transport sediment through mangrove environments (Furukawa and Wolanski, 1996) by creating an imbalance in maximum flow speeds owing to friction caused by vegetative drag. Mazda et al. (1995) previously explored the tidal asymmetry patterns observed and noted that greater ebb flow speeds in the vegetated fringe led to ebb dominance of the region. Numerical modeling also revealed that vegetation changes the tidal asymmetry and the shape of the cross-shore bottom profile, with denser vegetation developing a more convex profile (Bryan et al., 2017). Some vegetated coastal systems have shown the ability to trap sufficient sediment to keep pace with sea-level rise (Lovelock et al., 2015; Kumara et al., 2010; Walsh and Nittrouer, 2004). However, this capability depends strongly on the amount of sediment delivered to the system. As rivers form the primary mechanism of sediment input to coastlines (Nittrouer et al., 1995), it is critical to elucidate how factors such as variable discharge and winds influence the interaction of river plumes with vegetation, and hence also affect the sediment transport and deposition patterns.

Chapter 2 used an idealized numerical model of a mangrove-lined river debouching into a coastal bay to examine momentum balances and sediment fluxes into the forest from the different plume regions. They found that the principal balance between the bottom shear stress (enhanced by the presence

of vegetation) and baroclinic pressure gradient largely controlled the sediment deposition in the riverine sections of the domain. During flood tide, vertical advection and diffusion enhanced erosion in the fringe region. The longer duration of high water slack at the forest fringe region, pressure gradients, and inertial acceleration led to the advection of the suspended sediment into the forest, where deposition occurred. Sediment deposition was more prominent on the western than the eastern side of the model domain owing to the influence of Coriolis (Southern Hemisphere). During ebb tide, when the freshwater plume was at its maximum extent, the barotropic and baroclinic pressure gradients and the Coriolis acceleration resulted in the riverine sediment being delivered to the forest and mudflat regions. In the mid-field region, the magnitude of acceleration terms and changes in bed elevations were smaller. Away from the river mouth, in the far-field region of the plume, a stronger tidal influence led to sediment erosion in the mangrove fringe region (also observed in Chen et al., 2009). In the shallow forested regions, the presence of vegetative drag slows down the movement of sediment offshore and leads to an overall flood dominance (also noted in Fagherazzi et al., 2015).

In the above study, momentum balances were evaluated for a single river discharge, and the effects of wind forcing were not considered. Chao (1988a,b) explored the effects of bathymetry and wind forcing on river plume circulation, with a model encompassing both the estuary and the shelf. They highlighted that the plume response to wind forcing was strongly dependent on the orientation of the wind stress: upwelling wind events cause the plume to become more expansive as the seaward front is advected offshore (e.g. Hallock and Marmorino, 2002; Lentz and Chapman, 2004). In contrast, in the presence of downwelling winds, the plume is confined against the coast due to the onshore surface currents of the Ekman flow fields, which results in a narrower plume with less area exposed to the wind.

Here, we explore the influence of forcing factors of river discharge and wind (both speed and direction) on a sediment-laden freshwater river plume in a mangrove-fringed coastal region, and in particular, how these factors affect the resulting sediment deposition patterns. Section 3.2 describes the idealized numerical model scenarios, including model parameters and boundary conditions. In Section 3.3, we show the dependence of sediment fluxes into the forest on varying river flows and wind speeds, and directions. The implications for the morphological evolution are discussed in Section 3.4. Conclusions are presented in Section 3.5.

3.2 Methods

3.2.1 Numerical model

The idealized numerical model used in this study was developed in Delft3D (Deltares, 2021). The Delft3D software package solves both the continuity and the three-dimensional shallow-water equations under the Boussinesq assumption and has been successfully applied across many modeling studies to study hydro-morphodynamics (Roelvink and Van Banning, 1995; Lesser et al., 2004).

3.2.1.1 Study area, model grid, and bathymetry

The idealized model is based on the dimensions and bathymetry of the Firth of Thames (FoT, [S37°12′ E175°30′]) located to the south of the Hauraki Gulf, New Zealand as described in the prior study by Vundavilli et al. (2021). *Avicennia marina* mangrove habitat lines the river mouths and southern coast of the Firth. Mangrove coverage has expanded rapidly since the 1960s owing to sediment input from three rivers Waihou, Piako, and Waikataruru (Horstman et al., 2018). A 3-D curvilinear and symmetric (along the longitudinal axis) grid of 25 km in the longitudinal direction and 35 km in the latitudinal direction was decomposed into three model domains: The outer domain had a varying grid resolution of 500 m x 900 m near the tidal boundary to a finer grid

size of 200 m x 475 m. The central domain covered the vegetated region and the tidal flats with grid cells of sizes $\sim$ 218 m x 140 m in the deeper regions to 15 m x 6 m in the mangrove areas. Grid sizes in the lower domain consisting of the river varied from 25 m x 17 m at the river mouth to 15 m x 10 m at the upstream boundary. In the vertical direction, there were five sigma layers of equal thickness (20% of the water depth).

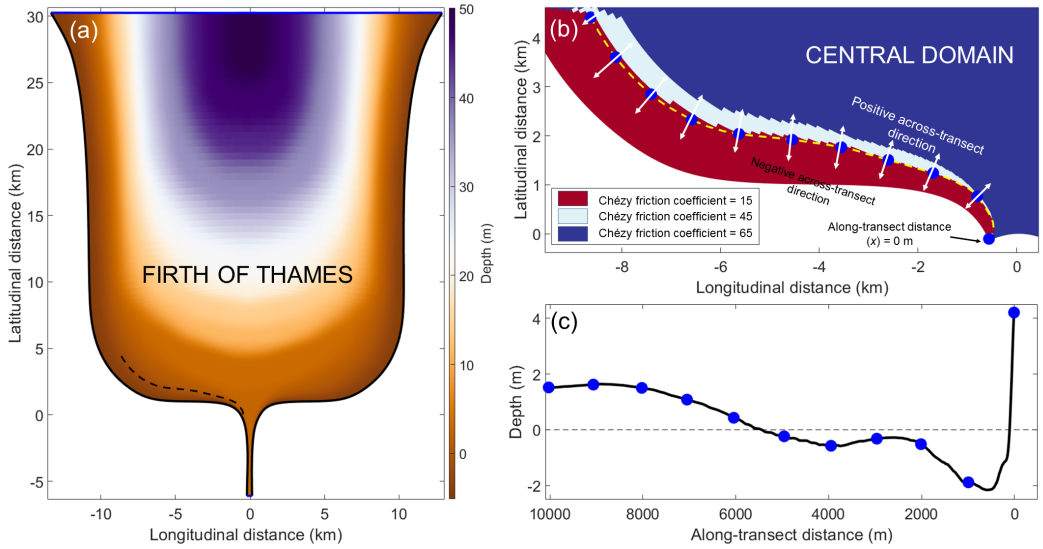

Figure 3.1: Panel (a) shows the idealized symmetric bathymetry, transect along the forest edge (black dashed line), (b) spatially varying Chézy roughness coefficient used in the model central domain to represent vegetation, and (c) shows the depth profile along the transect. Thick blue lines in Panel (a) represent tidal (top) and river (bottom) boundaries. The transect is shown by thick yellow and black lines in panels (b) and (c), respectively. Blue circles are shown every 1000 m. In panel (b), the white arrows depict the across-transect directions.

In our vegetated simulations, a spatially varying Chézy value (Figure 3.1b) was employed to represent vegetation based on literature values (Zhang et al., 2012; Mazda et al., 1997). In particular, the forest was represented with a Chézy value of 15 $\mathrm{m}^{1/2}.\mathrm{s}^{-1}$ (corresponding to a friction coefficient of C_D = 0.044) and the intertidal zone with a Chézy value of 65 $\mathrm{m}^{1/2}.\mathrm{s}^{-1}$ ($C_D = 0.0023$). The thin transition zone ($\sim$ 200 m fringe area) between the forest and intertidal flats was represented with a value of 45 $\mathrm{m}^{1/2}.\mathrm{s}^{-1}$ ($C_D = 0.0048$).

3.2.1.2 Model parameters and boundary conditions

The model was forced along the northern boundary with an M2 astronomic tide of amplitude 1.3 m and a constant salinity of 31 ppt. The southern river boundary was forced with a freshwater discharge with a riverine sediment input of 1 $kg.m^{-3}$. The Coriolis parameter was defined for -37° latitude. The horizontal eddy viscosity and diffusivity, were set to 1 $m^2.s^{-1}$, and 0.1 $m^2.s^{-1}$, respectively. The settling velocity, critical bed shear stress, and erosion parameters were set at 0.1 $m.s^{-1}$, 0.1 $N.m^{-2}$, and 0.0001 $kg.m^{-2}$ $.s^{-1}$, respectively, based on literature values (Mehta and Partheniades, 1982). In our model runs with winds, spatially uniform wind speeds and directions were specified over the entire domain. All the wind parameters such as air density, and drag coefficients were set to Delft3D defaults (Deltares, 2021). These models were run with a threshold depth of 0.1 m, and a cyclic advection scheme was chosen for the spatial discretization of momentum.

To satisfy the Courant–Friedrichs–Lewy condition, a time step of 0.01 min was used. The model simulation was forced at the river boundary with a freshwater discharge (no sediment input) for an initial spin-up period of 7 days (flow time) to achieve a quasi-steady state. Subsequently, the model simulations were conducted for another seven days with a sediment concentration input of 1 $kg.m^{-3}$ through the river boundary. While the sediment class was restricted to cohesive sediments in our model simulations, we label the sediments to distinguish between the riverine (new sediments input at the boundary) and bed-sourced sediments (legacy sediments). This approach allowed us to track the delivery of sediment to the mangrove forest. An initial sediment bed level thickness of 2 m was used throughout the model domain. For a detailed sensitivity analysis conducted to understand the influence of the initial bed sediment thickness on the overall total sediment fluxes, see Appendix B. Morphological evolution in Delft3D can be accelerated using a Morphological Acceleration Factor (MORFAC) which is multiplied to the bed

level after each timestep to enable faster computational times (Lesser et al., 2004; Roelvink and Van Banning, 1995). In our model simulations, a MORFAC of 12 was used to simulate $\sim$ 3 months of morphological evolution.

3.2.1.3 Modeled scenarios

A total of 114 model simulations (57 runs each for vegetated and non-vegetated simulations) were performed to understand the effects of varying discharges and winds on the sediment transect fluxes (Table 3.1). River discharges varied from $0\,\mathrm{m^3.s^{-1}}$ to $455\,\mathrm{m^3.s^{-1}}$, with an increment of $35\,\mathrm{m^3.s^{-1}}$. Additionally, a high discharge event of $480\,\mathrm{m^3.s^{-1}}$ was also modeled (Table 3.1). Winds were applied for three different discharges ($35\,\mathrm{m^3.s^{-1}}$, $175\,\mathrm{m^3.s^{-1}}$, and $480\,\mathrm{m^3.s^{-1}}$). Simulations with no wind and wind speeds of $5\,\mathrm{m.s^{-1}}$, and $10\,\mathrm{m.s^{-1}}$ were selected based on the climate data recorded for the Firth of Thames station averaged over a year (2019 - 2020). For each wind speed, model simulations were conducted with wind directions ranging from 0° - 315° with an increment of 45°. The model scenarios employed in this study encompass the most commonly occurring conditions in the Firth of Thames region, while also covering the full parameter space.

3.2.2 Analysis of model results

To quantify the sediment transport into the vegetation, we define a transect which separates the forest from the mudflat along the edge of the west-side mangrove forest (Figure 3.1c). The transect begins from the raised river bank located in the river mouth, incorporates a slightly deeper section of the mudflat around the bend, and extends along the edge of the western mangrove forest. The depth profile along the transect is shown in Figure 3.1c, and the along-transect position $x = 0\,\mathrm{m}$ corresponds to the beginning of the transect. Regions close to the river mouth ($0 \lesssim x \lesssim 100\,\mathrm{m}$) and shallow regions away from the river mouth ($x \gtrsim 6000\,\mathrm{m}$) remained dry throughout the model simulations.

Table 3.1: Model simulations undertaken in our study for the vegetated simulations. Simulations 58-114 used a uniform Cheźy roughness coefficient of $65\,\mathrm{m}^{1/2}.\mathrm{s}^{-1}$ ($C_D = 0.0023$) throughout the domains, but were otherwise identical to 1-57.

Varying parameters	Model runs	River discharge ($\mathrm{m}^3.\mathrm{s}^{-1}$)	Wind speed ($\mathrm{m.s}^{-1}$)	Wind direction (°)	Increment in wind direction
River discharge	1 - 15	0, 35, 70, 105, 140, 175, 210, 245, 280, 315, 350, 385, 420, 455, 480	0	-	-
Winds	16 - 22	35	5	0 - 315	45°
	23 - 29	35	10	0 - 315	45°
	30 - 36	175	5	0 - 315	45°
	37 - 43	175	10	0 - 315	45°
	44 - 50	480	5	0 - 315	45°
	51 - 57	480	10	0 - 315	45°

3.2.2.1 Sediment flux calculations

In order to investigate the critical linkages between the riverine flows, tidal influence, and the wind in the presence of vegetation, we evaluate the sediment fluxes for sediment types (riverine and bed-sourced) separately. Instantaneous sediment fluxes for each type of sediment type (Q, $\mathrm{kg.m}^{-1}.\mathrm{s}^{-1}$) at time t, in the across-transect direction, are obtained by integrating the product of sediment concentration and the horizontal across-transect velocity over the height of water column:

$$Q(t) = \int_0^{h(t)} c(t,z) \cdot v(t,z).dz, \tag{3.1}$$

where, $c(t,z)$ is the instantaneous sediment concentration ($\mathrm{kg.m}^{-3}$), $v(t,z)$ indicates the horizontal across-transect velocity at height z and time t, and h is the height of the water column. The fluxes are integrated over the ebb, flood, and the full tidal cycle to provide the net sediment transport into and out of

the forest region (Equation 3.2). In the intertidal zones, only the timesteps when the grid cell was fully inundated were used in the flux calculations.

$$Q = \int_0^T Q(t).dt, \tag{3.2}$$

where, Q is the time-integrated sediment transport flux.

The time-integrated fluxes ($\mathrm{kg.m^{-1}}$) were further integrated along the entire length of the transect (Equation 3.3) to estimate the net mass transfer (kg),

$$M = \int_0^X Q.dx, \tag{3.3}$$

where, X is the total length of transect in the along-transect direction.

In our evaluations, positive fluxes correspond to an offshore flux directed out of the mangrove forest, and negative fluxes correspond to sediment movement into the mangrove forest (Figure 3.1b).

3.3 Results

As this study aims to understand the morphological response to sediment transported in the buoyant river plume under the influence of varying river flows and winds, we briefly describe the plume hydrodynamics but predominantly focus on the sediment transport results. A detailed description of the model output from a single discharge scenario without winds, including an analysis of surface and bottom layer momentum balances within various regions of the river plume can be found in Vundavilli et al. (2021).

3.3.1 Plume dynamics

An example of along-transect distributions of residual across-transect velocities, riverine sediment concentrations, and horizontal sediment fluxes is shown in Figure 3.2 for the simulation with a river flow of $175\,\mathrm{m^3.s^{-1}}$. We divide the transect into three zones to highlight the different sections of the river plume which interact with the vegetation at these locations. Following Hetland (2005), these distinct dynamical regions of the river plume in our model simulations are: the near-field mixing zone, which is localized at lower salinity values (5-15 ppt), mid-field region, which encapsulates the anti-cyclonic bulge (16-25 ppt), and the far-field which has a lower rate of mixing with a salinity range of 26-29 ppt.

Mean across-transect horizontal velocities along the transect over ebb ranged from $\sim$ -0.12 $\mathrm{m.s^{-1}}$ in the near-field zone close to the river mouth ($100\,\mathrm{m} \lesssim x \lesssim 2100\,\mathrm{m}$) to about $\sim 0.03\,\mathrm{m.s^{-1}}$ in the bottom of the mid-field region ($2100\,\mathrm{m} \lesssim x \lesssim 3500\,\mathrm{m}$) and far-field zones ($x \gtrsim 3500\,\mathrm{m}$). While across-transect velocities were directed into the forest zone in the near-field region (negative), in the mid and far-field regions, velocities were oriented out of the forest (positive). Over ebb, as the plume debouched from the river mouth, riverine sediment remained on the surface layer and underwent rapid mixing in the near-field zone. The sediment concentrations ranged from $\sim 0.25\,\mathrm{kg.m^{-3}}$ on the surface to $\sim 0.15\,\mathrm{kg.m^{-3}}$ in the bottom. In the mid-field and far-field zones, riverine sediment concentrations were close to zero.

Over the flood tide, as the plume is pushed back into the river mouth due to the incoming tidal currents, the near-field zone extends just over $\sim$1000 m of the transect ($100\,\mathrm{m} \lesssim x \lesssim 1100\,\mathrm{m}$), and the section of the transect interacting with the re-circulating mid-field region is also narrower $1100\,\mathrm{m} \lesssim x \lesssim 1600\,\mathrm{m}$. In the mid- and far-field regions of the river plume ($x \gtrsim 1100\,\mathrm{m}$),

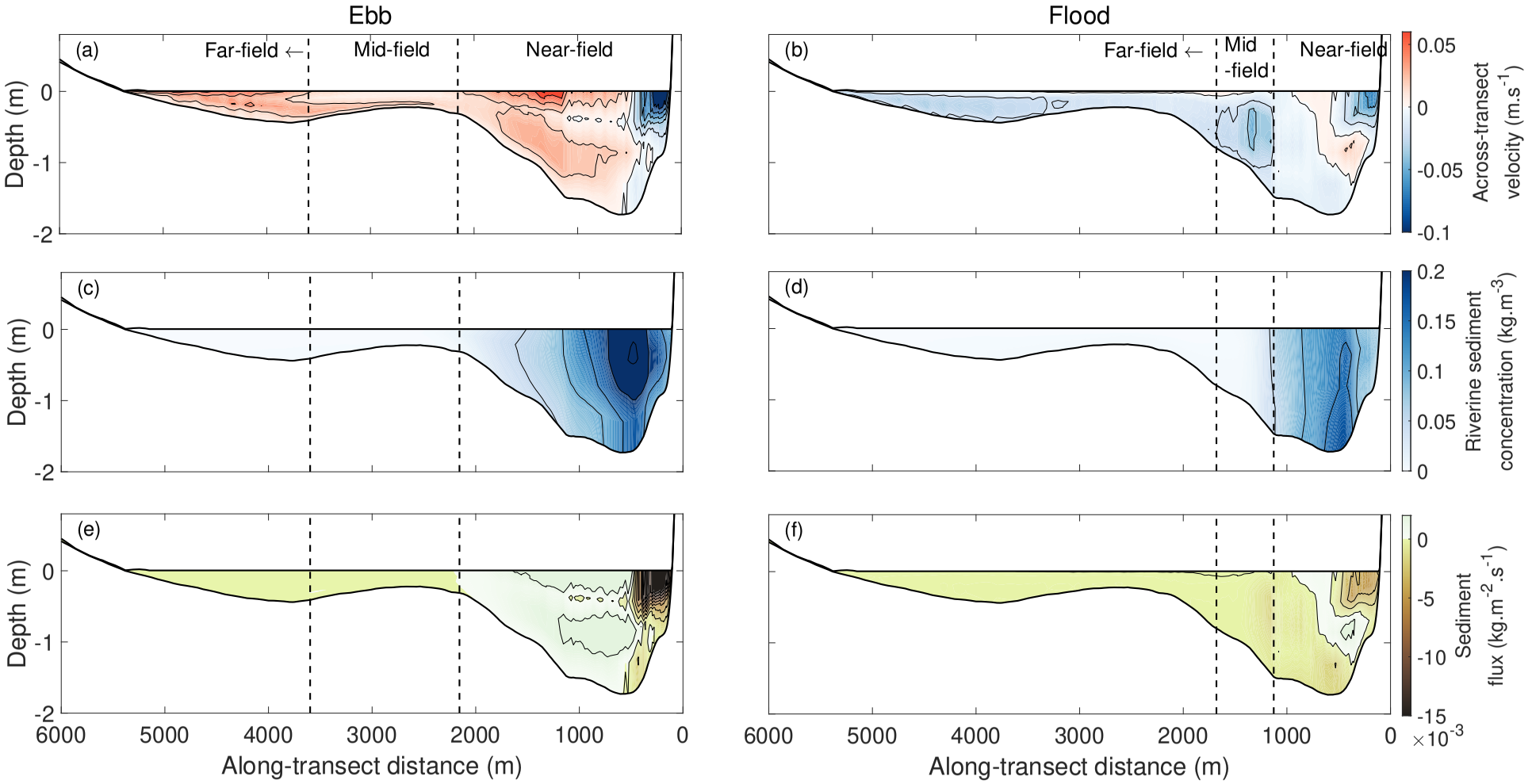

Figure 3.2: Across-transect velocity (a, b), riverine sediment concentration (c, d), and horizontal sediment flux (e, f) along the transect for the $175\,\mathrm{m^{-3}.s^{-1}}$ discharge scenario (Run 6, Table 3.1). Panels a, c, e are mean over ebb and panels b, d, and f are mean over the flood tide. The along-transect distance of zero corresponds to the shallow river bank. Dashed black lines delineate the different regions relative to the sediment plume. Thin black lines show $0.02\,\mathrm{m.s^{-1}}$, $0.05\,\mathrm{kg.m^{-3}}$, and $0.002\,\mathrm{kg.m^{-2}.s^{-1}}$ contours in panels a and b, c and d, e and f, respectively.

as the plume loses its momentum, tidal currents dictate the transport of the sediment in this region, and the across-transect velocities are directed into the forest (Figure 3.2b).

Magnitudes of the across-transect mean velocities ranged from $\sim 0.02\,\mathrm{m.s^{-1}}$ on the surface to $\sim 0.004\,\mathrm{m.s^{-1}}$ in the bottom layer. While the surface layer velocities were directed out of the forest, the bottom layer velocities, however, were directed into the forest region (Figure 3.2b). In the near-field region ($100\,\mathrm{m} \lesssim x \lesssim 1100\,\mathrm{m}$), modeled riverine sediment concentrations in the bottom were ~ 5 times greater than in the surface layer (Figure 3.2d). Away from the river mouth in the far-field region of the river plume, river-sourced sediment concentrations were negligible. Along the transect, over the flood stage of the tidal cycle, in the near-field zone ($100\,\mathrm{m} \lesssim x \lesssim 1100\,\mathrm{m}$), sediment fluxes were directed into the forest region on the surface layer and away from the forest in the bottom layer (Figure 3.2f).

3.3.1.1 Tidally integrated fluxes

Figure 3.3 shows the depth-integrated across-transect fluxes of riverine, bed-sourced and the total sediment for the $175\,\mathrm{m^3.s^{-1}}$ discharge scenario. For along-transect distances of $x \gtrsim 2500$, fluxes were $\mathcal{O}(0)$, so only the regions close to the river mouth are shown in subsequent figures. Over the ebb stage (Figure 3.3b), in the regions closer to the river mouth ($100\,\mathrm{m} \lesssim x \lesssim 500\,\mathrm{m}$), both the riverine and bed-sourced sediment fluxes were found to be directed into the forest region with magnitudes of the riverine sediment fluxes nearly double that of the bed-sourced sediment fluxes. Farther along the transect ($500\,\mathrm{m} \lesssim x \lesssim 1100\,\mathrm{m}$), as the river pushed through the transect owing to the near-field circulation, the direction of the fluxes was now reversed and sediment was directed out of the forest region (Figure 3.3b). Riverine sediment transport remained the dominant contributor to sediment transport in this part of the transect. In the far-field region ($x \gtrsim 1100\,\mathrm{m}$), owing to the loss of

momentum carried by the river in this region, tidal currents remain the major drivers of the sediment and both the riverine and bed-sourced sediment are directed out of the forest (Figure 3.3b). As expected, contributions towards the total transport was dominated by the bed-sourced sediment with only modest contributions from the riverine sediment.

Over the flood tide, sediment fluxes were directed into the forest region over close to the entirety of the transect; however, the dominant contributors to the fluxes varied along the transect (Figure 3.3c). Riverine and bed-sourced sediments were of similar magnitudes contributions in the near-field region of the river plume ($0 \lesssim x \lesssim 500\,\mathrm{m}$); however, as the freshwater plume is pushed back into the river mouth due to the oncoming tidal currents, the plume spread is restricted and bed-sourced forms the largest contributor to the fluxes elsewhere along the transect (Figure 3.3c). Over the full tidal cycle, sediment is transported into the forest close to the river mouth ($100\,\mathrm{m} \lesssim x \lesssim 500\,\mathrm{m}$), with greater riverine sediment contributions over that of the bed-sourced sediment by nearly $\sim 45\%$. Farther along the transect ($500\,\mathrm{m} \lesssim x \lesssim 1000\,\mathrm{m}$), the total sediment transport is directed out of the forest facilitated through as the freshwater plume is pushed through the forest close to the river mouth, and fluxes of bed-sourced sediments are minimal (Figure 3.3a).

3.3.2 Tidally integrated fluxes and total sediment mass loads under varying river flows

To examine the effects of varying discharges, we consider the sediment fluxes with position on the transect (Figure 3.4) and the total sediment mass loads integrated along the full length of the transect (Figure 3.5). Close to the river mouth, sediment was transported into the forest lining the river banks, and total sediment flux magnitudes increased with discharge. The relative importance of the sediment type varied across river discharges. In particular, for low to medium river flows ($35\,\mathrm{m^3.s^{-1}}$ - $210\,\mathrm{m^3.s^{-1}}$), the contributions of river-

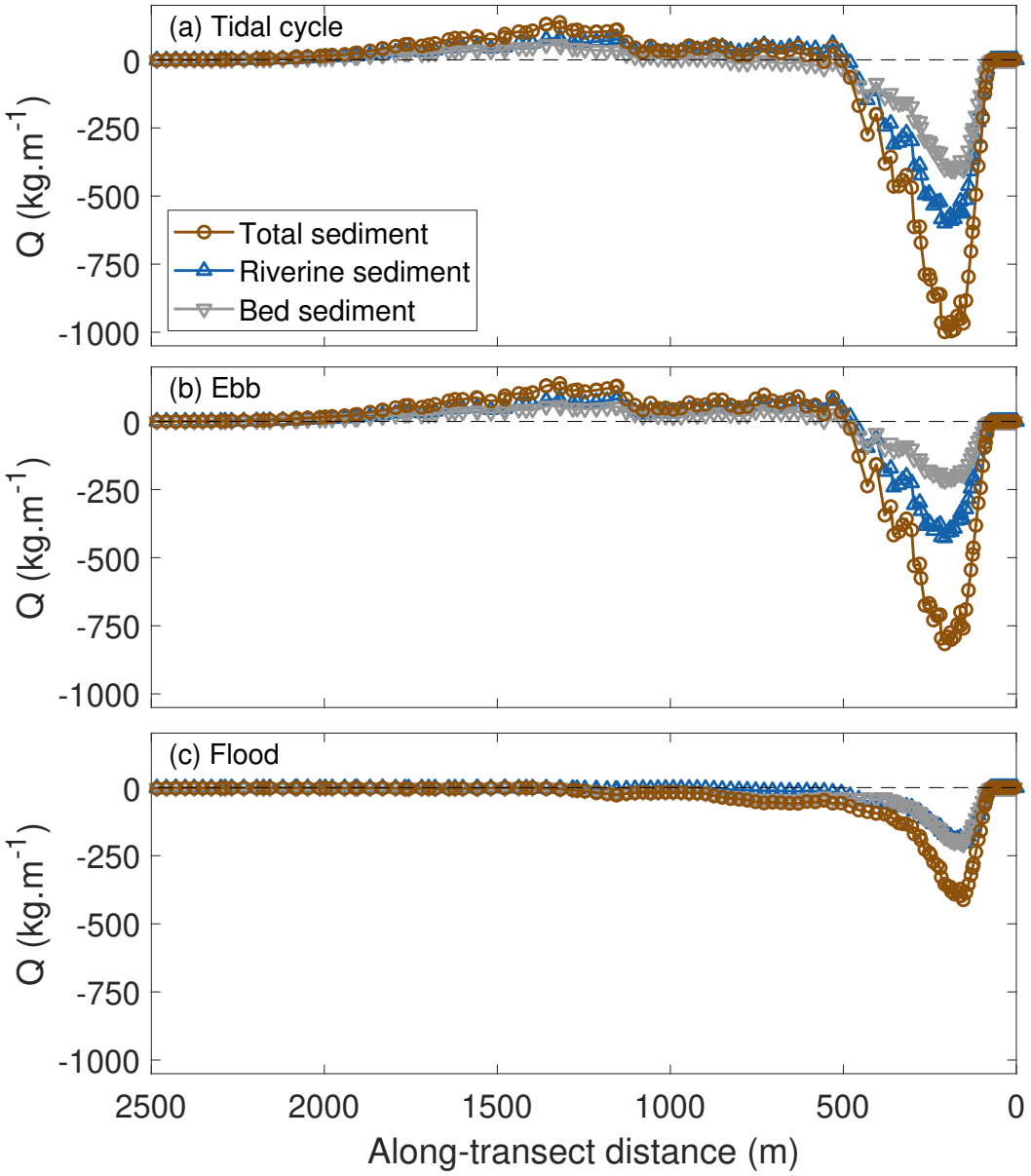

Figure 3.3: Across-transect total, riverine, and bed-sourced sediment fluxes (Q) along the transect were evaluated for the 175 $m^3.s^{-1}$ discharge scenario integrated over: (a) the full tidal cycle, (b) the ebb stage, and (c) the flood stage. Thick brown lines represent the total sediment fluxes, blue lines represent the riverine sediment fluxes, and thick grey lines represent the corresponding fluxes for the bed-sourced sediment. In our evaluations, positive and negative fluxes indicate sediment transport out of the forest and into the forest region, respectively.

ine and bed-sourced sediment were similar in the near-field region of the river plume. For higher river flows, the riverine sediment was the major contributor towards the total sediment into the forest in the region ($0 \lesssim x \lesssim 500$ m, Figure

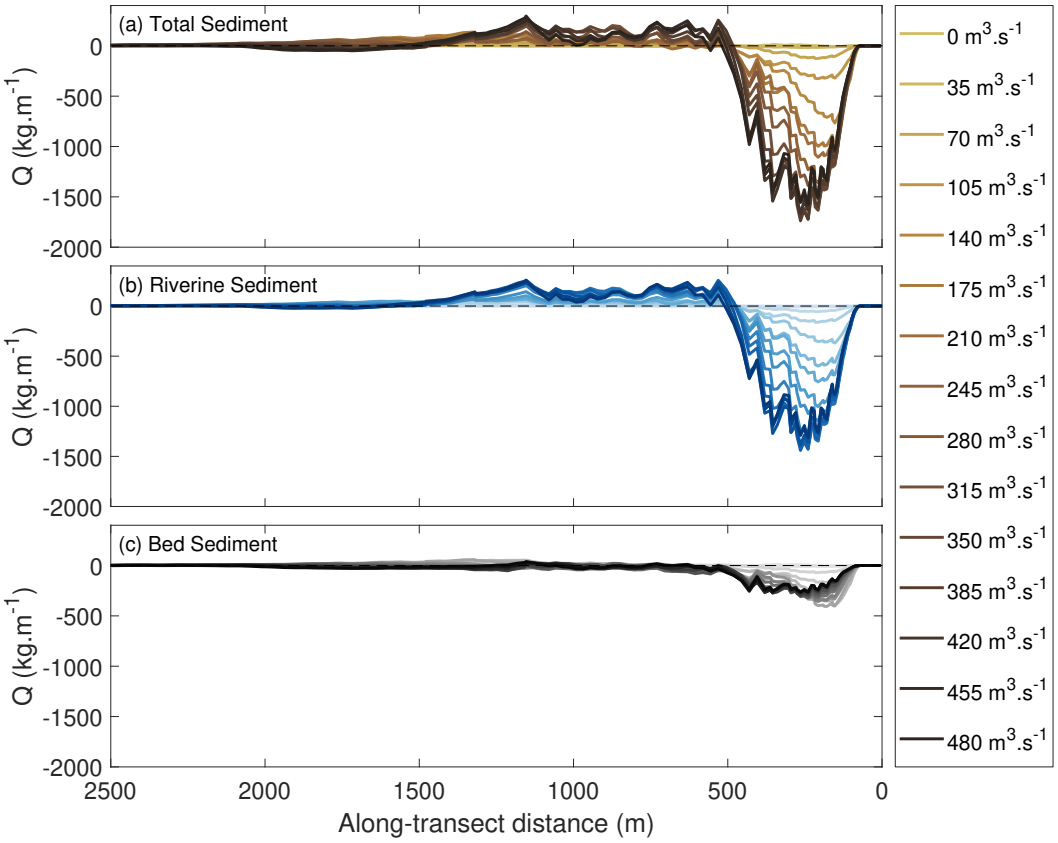

Figure 3.4: Comparison of the tidal integrated across-transect (a) total sediment fluxes (brown lines), (b) riverine sediment fluxes (blue lines), and (c) bed-sourced sediment fluxes (black lines) for each of the discharge scenarios (Table 3.1, row 1) undertaken in the study. Colors show individual discharge scenarios from low discharge (lighter shades) to high discharge (darker shades). In our evaluations, positive and negative fluxes indicate sediment transport out of the forest and into the forest region, respectively.

3.4a). In the region ($500\,\mathrm{m} \lesssim x \lesssim 1000\,\mathrm{m}$), the riverine sediment transport was directed out of the forest irrespective of the discharge employed in our model simulations. Farther away from the river mouth, in the region, $x \gtrsim 1500\,\mathrm{m}$, the total sediment transport was directed out of the forest region for all except the highest discharges. For the very large discharges ($> 210\,\mathrm{m^3.s^{-1}}$), the anti-cyclonic bulge of the river plume extends into this region and moves suspended bed-sourced sediment (lifted off during flood) into the forest (Figure 3.5a and c).

Figure 3.5 shows the total, riverine and bed-sourced sediment mass loads

integrated along the full transect for the different discharges. The transport over the flood stage of the tidal cycle is around an order of magnitude larger than that during ebb, and hence dominates the contributions to the total transport. The total sediment mass load was directed into the forest for all discharges, indicating an accretionary environment. Mass loads were found to increase approximately linearly with discharge across the range $70\,\mathrm{m}^3.\mathrm{s}^{-1}$ to $280\,\mathrm{m}^3.\mathrm{s}^{-1}$, at which point, further increases in discharge only resulted in small amounts of additional sediment being delivered to the forest. For these larger discharges, a greater portion of the sediment delivered to the mangroves is pushed through and out of the forest (Figure 3.4b). The relative contributions towards the total sediment were found to be similar for both the bed-sourced and riverine sediment for river discharges up to $210\,\mathrm{m}^3.\mathrm{s}^{-1}$, beyond which the relative contribution of the riverine sediment increased (to approximately double that of the bed-sourced sediment).

3.3.3 Response of the river plume and sediment transport to varying wind velocities

3.3.3.1 Influence of winds on the plume structure

The influence of wind direction on the sediment transport can be seen in the tidal residual of the riverine sediment concentrations and horizontal velocities in the surface layer (Figure 3.6, gives an example for wind speeds of $5\,\mathrm{m}.\mathrm{s}^{-1}$ and a discharge of $175\,\mathrm{m}^3.\mathrm{s}^{-1}$). Compared with the no-wind scenario (Figure 3.6a), northerly winds push the plume back into the river mouth leading to an accumulation of the riverine sediment in this region. While the surface current residuals remain unaltered in this region ($0 \lesssim y \lesssim 2\,\mathrm{km}$ in the latitudinal direction), residual currents in the region away from the river mouth ($x \geq 2\,\mathrm{km}$ in the longitudinal direction) are altered due to the surface winds.

Across all of the model simulations, easterly winds (90°) were found to

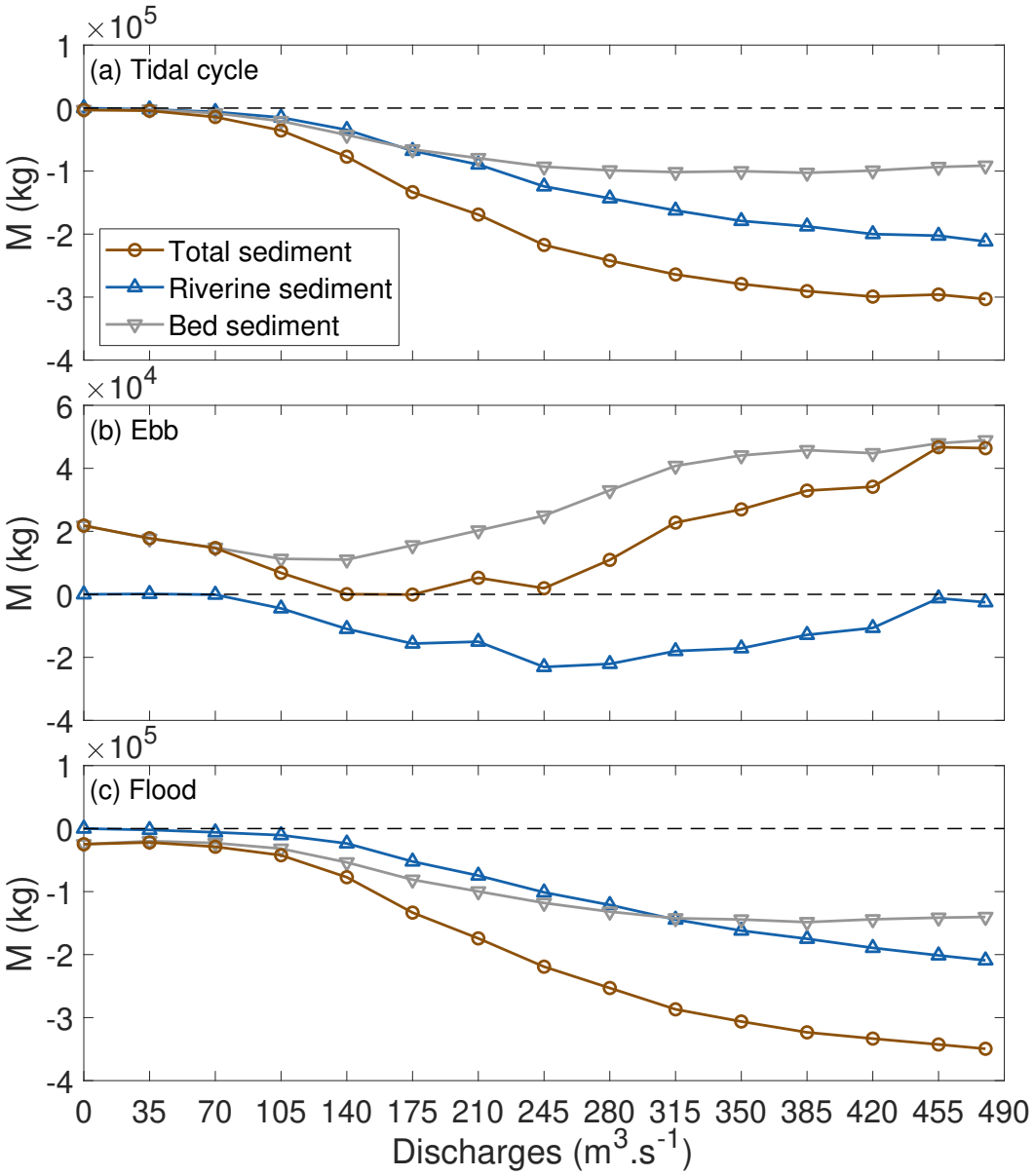

Figure 3.5: Comparison of the sediment mass loads (in kg) of total (brown lines), riverine (blue lines), and bed-sourced sediment (grey lines) through the transect as a function of each discharge scenario undertaken in the study. Panels (a), (b), and (c) show the mass loads integrated over the entire tide, ebb stage, and flood stages of the tidal cycle, respectively. Positive and negative mass loads indicate sediment transport out of the forest and into the forest region, respectively.

maximize the sediment transport into the transect (Figure 3.6d). Southerly winds (180°) effectively increase the overall plume extent in our simulations and increase the sediment concentration observed close to the river mouth ($\sim 0.2\,\mathrm{kg.m^{-3}}$). Westerly, southwesterly, and northwesterly winds were sufficient

to dominate over Coriolis and generated a strong wind-driven eastward flow in the regions away from the river mouth (Figure 3.6g, h, and i).

3.3.3.2 Tidally integrated fluxes under varying winds

Figure 3.7 shows the total sediment flux, riverine sediment flux, and bed-sourced sediment fluxes along the transect evaluated over a tidal cycle for a $175\,\mathrm{m}^3.\mathrm{s}^{-1}$ discharge with varying wind directions and two wind speeds (Model runs 16-57, Table 3.1).

The response of the plume to the winds changed between the different regions of the sediment plume. Wind speeds of $5\,\mathrm{m.s}^{-1}$ were not sufficient enough to alter the direction of the sediment transfer closer to the river mouth. In the region close to the river mouth ($0 \lesssim x \lesssim 500\,\mathrm{m}$), total sediment transport was found to be directed into the forest irrespective of the direction of the wind with both riverine and bed-sourced sediments contributing towards the total sediment transport (Figure 3.7a). Farther along the transect ($x \gtrsim 500\,\mathrm{m}$), total sediment transport in this region was dictated by the wind direction. In particular, in the case of easterly, wind directions (0° - 180°), the total sediment transport was into the forest; however, in the case of westerly wind directions (225° - 315°), the sediment transport was instead directed out of the forest. The fluxes of bed-sourced sediment were more strongly influenced by wind directions than those of riverine sediment. In particular, the maximum fluxes or river sediments into the forest in the region $0 \lesssim x \lesssim 500\,\mathrm{m}$ varied between $\sim 500\,\mathrm{kg.m}^{-1}$ and $\sim 750\,\mathrm{kg.m}^{-1}$ for all the wind directions, while the maximum fluxes of bed-sourced sediments ranged from $\sim 200\,\mathrm{kg.m}^{-1}$ and $\sim 650\,\mathrm{kg.m}^{-1}$.

In our model simulations, the presence of strong winds ($10\,\mathrm{m.s}^{-1}$, Figure 3.7b, d, and f) significantly altered the total transport fluxes along the transect. Close to the river mouth ($0 \lesssim x \lesssim 500\,\mathrm{m}$), while the total sediment

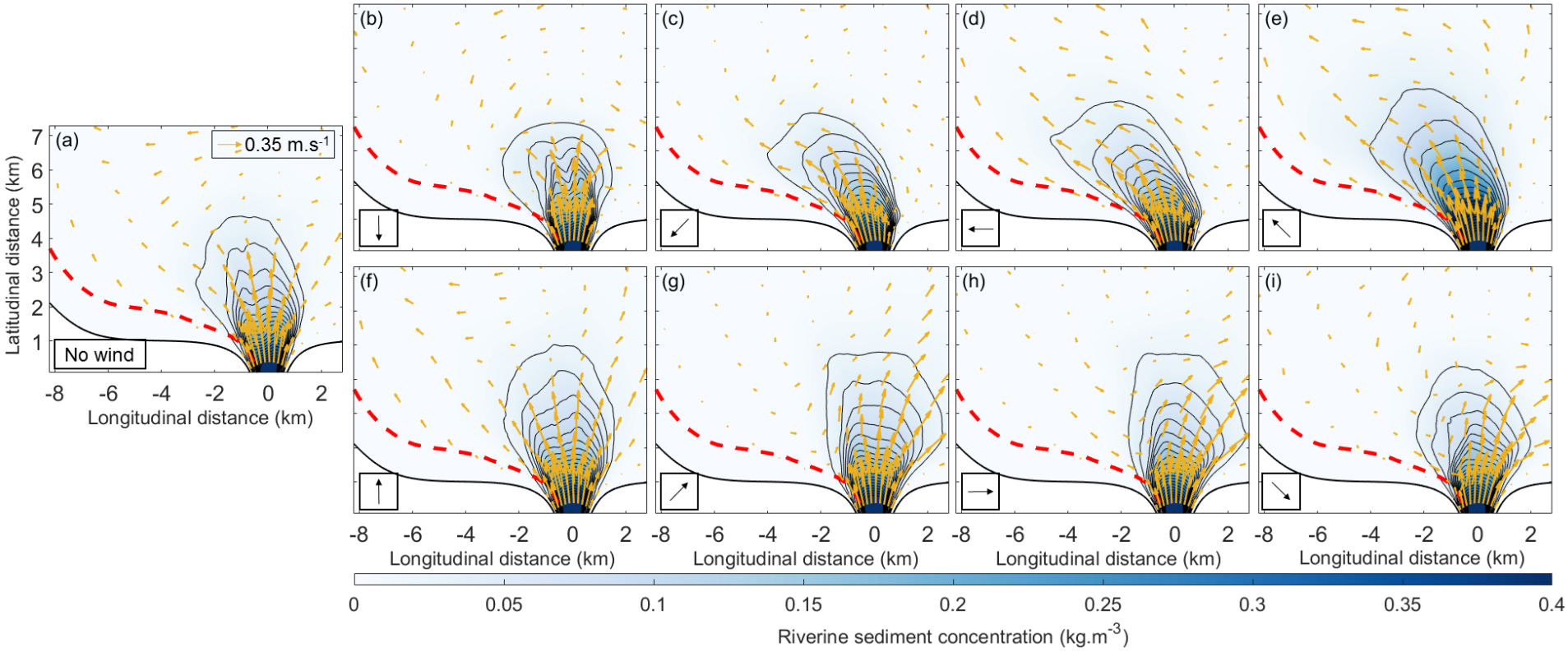

Figure 3.6: Response of the surface layer tidal residual sediment plume with discharge forcing of $175\,\mathrm{m^3.s^{-1}}$ and $5\,\mathrm{m.s^{-1}}$ wind speeds. Insets show wind direction (b) Northerly (0°), Panel (c) Northeasterly (45°), Panel (d) Easterly (90°), Panel (e) Southeasterly (135°), Panel (f) Southerly (180°), Panel (g) Southwesterly (225°), Panel (h) Westerly (270°), and Panel (i) Northwesterly (315°). Yellow arrows show the surface layer residual velocities. Thin black contours show $0.02\,\mathrm{kg.m^{-3}}$. The corresponding no-wind scenario is shown in Panel (a). The thick red line shows the location of the transect. Colorbar represents riverine sediment concentration in $\mathrm{kg.m^{-3}}$.

transport was directed into the forest irrespective of the wind direction, the magnitudes increased by nearly 75% in the case of easterly wind, and reduced by 42% in the case of westerly directions (225°, 270°, 315°, Figure 3.7b) in comparison to that of $5\,\mathrm{m.s^{-1}}$ wind speeds. In the region defined by the along-transect distance of $500\,\mathrm{m} \lesssim x \lesssim 1500\,\mathrm{m}$, as the wind altered the plume structure, magnitudes of the total sediment fluxes were largest (due to larger riverine and bed-sourced sediment contributions) in the case of easterly wind directions, while conversely, fluxes were smaller for westerly wind directions. Similarly, in the far-field region of the plume where the influence of river momentum was minimal, winds controlled the direction of the total sediment transport flux (Figure 3.7a). In the case of westerly winds, the entirety of the sediment plume was pushed away from the transect, and hence contributions of the riverine sediment fluxes towards the total transport were negligible.

Interestingly, along the forest in the region $x \gtrsim 1500\,\mathrm{m}$, the bed-sourced sediment fluxes in the presence of $5\,\mathrm{m.s^{-1}}$ winds were insignificant; however, strong winds of $10\,\mathrm{m.s^{-1}}$ significantly altered the bed-sourced sediment fluxes (lower left inset (Figures 3.7e and f)). In particular, while the bed-sourced sediments were $\sim 10\%$ of that observed in the near-field region in the case of light winds of $5\,\mathrm{m.s^{-1}}$, bed-sourced sediments were $\sim 33\%$ in the case of $10\,\mathrm{m.s^{-1}}$ wind speeds.

3.3.3.3 The combined influences of discharge and winds on tidally integrated sediment mass loads

The combined effects of discharge and winds on the mass loads into the forest over a tidal cycle are summarized in Figure 3.8. In the presence of $5\,\mathrm{m.s^{-1}}$ wind speeds, total sediment mass loads were found to be directed into the forest irrespective of the wind direction. However, in the case of low - medium river flow events ($35\,\mathrm{m^3.s^{-1}}$ and $175\,\mathrm{m^3.s^{-1}}$), total sediment mass loads were larger for all the easterly wind directions (45° - 135°). On the contrary, northerly,

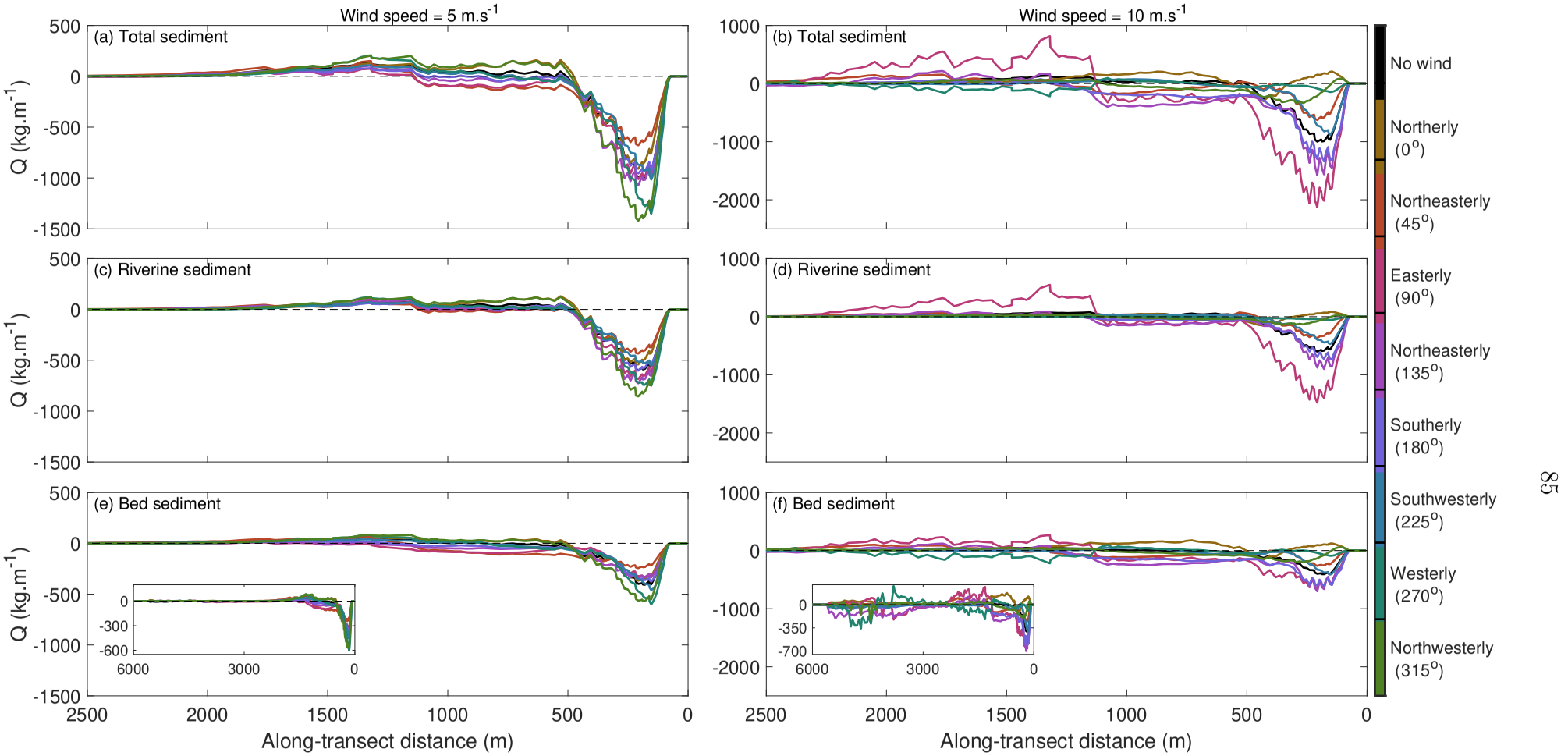

Figure 3.7: Integrated across-transect fluxes for the river discharge scenario of $175\,\mathrm{m^3.s^{-1}}$, for wind speeds of $5\,\mathrm{m.s^{-1}}$ (left-hand panels), and $10\,\mathrm{m.s^{-1}}$ (right-hand panels) for different wind directions. Panels (a) and (b) are total sediment fluxes, Panels (c) and (d) are fluxes of riverine sediments, and Panels (e) and (f) show bed-sourced sediments. In our evaluations, positive and negative fluxes indicate sediment transport out of the forest and into the forest region, respectively.

southerly, and westerly wind speeds of $5\,\mathrm{m.s^{-1}}$ were sufficient to alter the total sediment transport mass loads in the case of both the $35\,\mathrm{m^3.s^{-1}}$ and $175\,\mathrm{m^3.s^{-1}}$ discharge scenarios. While the largest magnitudes were observed in the south-easterly wind scenario, the lowest mass loads were found to be in the case of 0° for both cases of river discharge.

Mass loads varied substantially with wind direction for the high riverine discharge ($480\,\mathrm{m^3.s^{-1}}$) scenario. Interestingly, the highest sediment mass load was recorded in the case of the southwesterly wind scenario (225°, a westerly wind direction that directs the sediment plume away from the transect). This anomaly can be attributed to the decreased river sediment transport outflow (compared to remaining wind directions) in the mid-field region of the sediment plume (Figure 3.8c, $1500\,\mathrm{m} \lesssim x \lesssim 2100\,\mathrm{m}$), which consequentially leads to higher mass loads into the forest. In the presence of $5\,\mathrm{m.s^{-1}}$ wind speeds, both the riverine and bed-sediment loads were directed into the transect for all the discharge scenarios irrespective of the wind direction, except the model run with $480\,\mathrm{m^3.s^{-1}}$ in the case of northerly winds where the total sediment transport was instead directed out of the forest (Figure 3.8c). The reversal of the plume into the river due to wind can explain this reversal of the sediment transport direction. However, as the contributions of bed sediment transport were significantly lower than that of the riverine sediment, the sediment transport was found to be directed into the forest.

In the presence of strong winds ($10\,\mathrm{m.s^{-1}}$), the sediment mass loads were approximately double those in the $5\,\mathrm{m.s^{-1}}$ wind speed cases. Total mass loads increased non-linearly with discharge: In comparison to the $35\,\mathrm{m^3.s^{-1}}$ discharge scenario, mass loads were $\sim$ 10 and 15 times larger for the $175\,\mathrm{m^3.s^{-1}}$ and $480\,\mathrm{m^3.s^{-1}}$ discharge scenarios, respectively. The dependence on wind direction was more pronounced and similar for the larger discharges, with the notable result that irrespective of discharge, for northerly winds, sediment transport

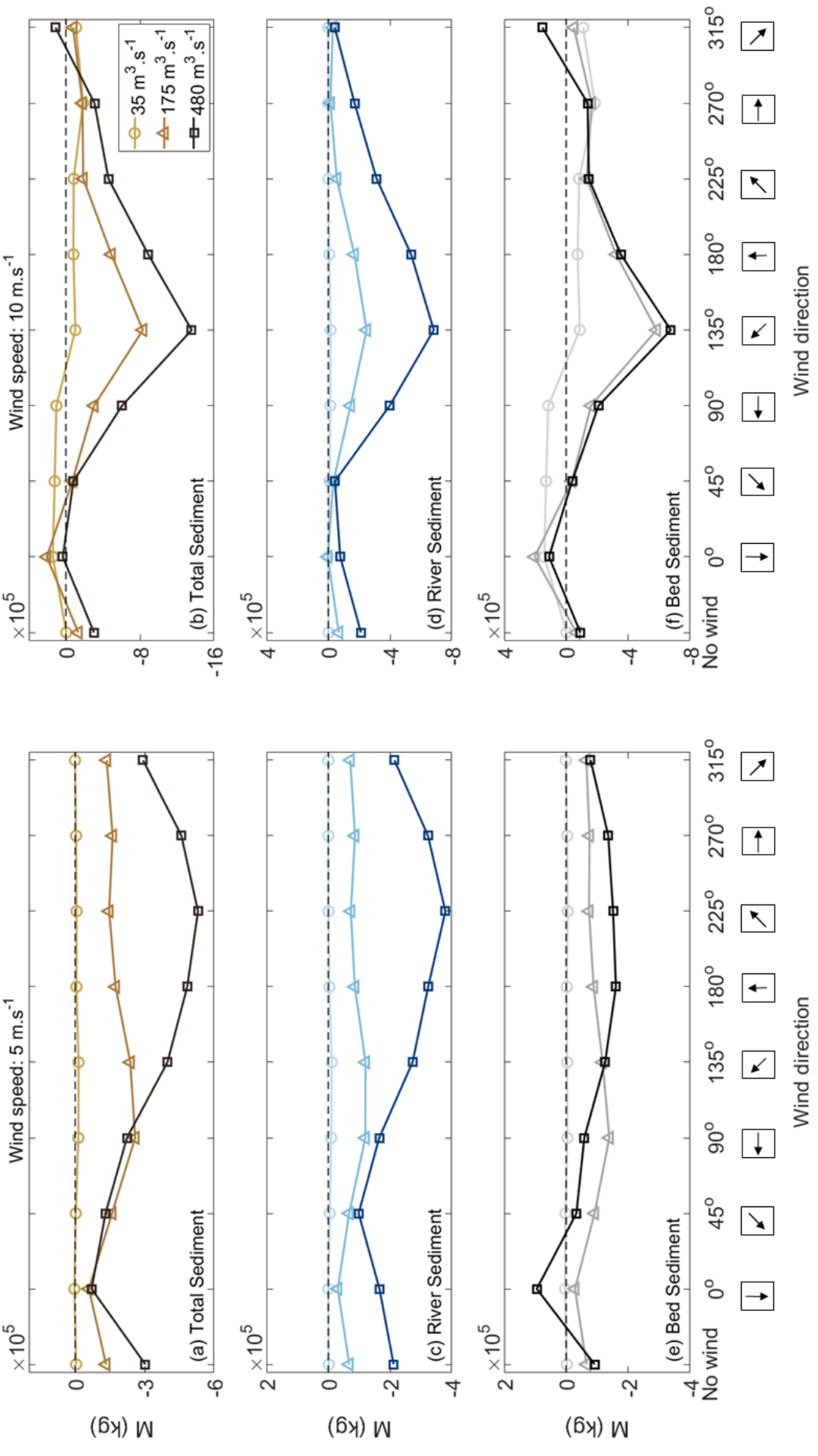

Figure 3.8: Comparison of the total (Panels a and b), riverine (Panels c and d), and bed-sourced sediment mass loads in kg (e and f) over the full transect for $35\,\mathrm{m^3.s^{-1}}$ (lighter shade, circles), $175\,\mathrm{m^3.s^{-1}}$ (triangles), and $480\,\mathrm{m^3.s^{-1}}$ (darker shades, squares) discharge scenarios for wind speeds of $5\,\mathrm{m.s^{-1}}$ (Panels a, c, and e) and $10\,\mathrm{m.s^{-1}}$ (Panels b, d, and f). Positive and negative mass loads indicate sediment transport out of the forest and into the forest region, respectively. Arrows in square boxes represent the wind direction.

was directed out of the forest. For larger river flows, the maximum mass loads were directed into the forest under south-easterly winds. Additionally, while the riverine sediment transport dominated the total sediment transport in the case of $175\,\mathrm{m}^3.\mathrm{s}^{-1}$ and $480\,\mathrm{m}^3.\mathrm{s}^{-1}$ discharges, bed-sourced sediment remained the major contributor towards the total sediment transport for all the wind directions employed in the case of $35\,\mathrm{m}^3.\mathrm{s}^{-1}$ discharge.

3.4 Discussion

In this paper, we studied the sediment transport patterns resulting from the interaction of a buoyant river plume with mangrove vegetation. We addressed the impact of various forcings (discharges and wind velocities) on the river plume by quantifying sediment fluxes into the forest using an idealized 3-D model. Our numerical model demonstrates that as the river debouches into the coastal waters, the plume undergoes various dynamical changes in the alongshore direction, in a similar manner to the observations of Horner-Devine et al. (2015). Consequently, fluxes of riverine sediments into the forest were highly dependent on the individual regions of the river plume in our simulations, and the distance over which they extended.

Closer to the river mouth, results indicate the river expanded laterally and pushed riverine sediment into the forest region irrespective of the discharge applied in our model simulations. The lateral spreading of sediments and formation of residual currents has been observed in locations without vegetation (see Leonardi et al. (2013), who studied the effects of tides on the evolution of mouth bars); however, drag from vegetation further enhances the deposition of sediment in this near-field forested region, which occurred across all stages of the tidal cycle. While the directional trends remained similar in the case of non-vegetated simulations (not shown), the magnitudes of the riverine sediment mass loads increased significantly in the absence of vegetative drag

(increased velocity). In the mid-field region (transition region between the near- and far-field region of the river plume), a small portion ($\sim$ 15%) of the sediment delivered by the river exited the forest.

The impact of vegetation varied on the bed-sourced sediment based on the river discharge employed in our model simulations. In particular, while the total sediment deposition was higher in the presence of vegetation for low discharge runs (0 - 105 $m^3.s^{-1}$), however in the cases of higher discharge ($\geq$ 140 $m^3.s^{-1}$), the bed-sourced sediment deposition was found to be larger in the case of non-vegetated runs. This difference in trends can be attributed to the coupled impact of the high bottom shear stresses (generated by vegetation) and high near-field turbulence (see MacDonald et al., 2007). In the case of low discharge events (0 - 105 $m^3.s^{-1}$), during the flood stage, a major part of the bed-sourced sediment is lifted off the bed due to enhanced bed-shear stresses (generated by the vegetative drag), and consequently, during the ebb stage, as the tide recedes, the sediment lifted off the bed now settles. Interestingly, in the case of high discharge events, while the mechanism of bed-sourced sediment transport remains similar during the flood stage, during the ebb stage; however, the presence of high-intensity turbulent eddies generated within the river plume keeps the sediment in suspension until the next flood stage. This result is consistent with Norris et al. (2019) who using field techniques with the mangrove forest in the lower Mekong Delta, Vietnam, found that the presence of mangrove pneumatophores enhances the net turbulent mixing near the bed.

Furthermore, in the case of large river flow events, the riverine dynamics dominate the transport along the entirety of the transect with a only modest tidal impact on the sediment transport. The reduced relative influence of tides can be seen in our study wherein the flood-averaged sediment mass load magnitudes were significantly lower in comparison to that of the ebb-averaged sediment mass loads. These results are consistent with field results from the

Apalachicola Delta, Florida, USA, by Leonardi et al. (2015) who established that, in the presence of high riverine discharge, reduction in tidal flow leads to a unidirectional outflow and an entirely river-dominated system. Similarly, results from laboratory experiments show periodic variations in the width of the plume structure under oscillatory discharge conditions leads to altered riverine transport either in the across-shore or along-shore transport directions (Yuan et al., 2018).

Horizontal advection in a river plume is controlled by plume buoyancy, mixing, and transport (Horner-Devine et al., 2015). Garvine (1995) previously identified limiting cases of offshore plume behavior based on the Kelvin number at the river mouth, defined as the ratio of the source width and the baroclinic deformation radius: $K = \frac{W}{\left(\frac{\sqrt{g'h}}{f}\right)}$, where W is the width of the river mouth g$'$ is the reduced gravity, h is the depth at the river mouth, and f is the Coriolis frequency (0.875 x $10^{-4}\,s^{-1}$ at -37° latitude). They suggested that plumes with $K \gg 1$ indicate linear dynamics, coupled with high flows, and exhibit a geostrophic balance in the across-shore directions. Conversely, plumes with $K \ll 1$ demonstrate sharp frontal boundaries and non-linear flow dynamics, while plumes with $K \sim 1$ were classified as intermediate cases.

We evaluated the tidal mean Kelvin numbers inside the river plume at a latitudinal distance of $\sim 1\,km$ (Figure 3.1a) for our simulations, which indicated a change in plume behavior regimes from small to large discharges. For river plumes of $35\,m^3.s^{-1}$ - $245\,m^3.s^{-1}$ Kelvin numbers ranged from ~ 0.20 to ~ 0.78, while for discharges $280\,m^3.s^{-1}$ - $350\,m^3.s^{-1}$ could be considered intermediate-sized plumes ($0.85 \leq K \leq 1.05$). For flows greater than $\geq 385\ m^3.s^{-1}$, Kelvin numbers range from ~ 1.2 - ~ 1.35 corresponding to different dynamics in the region. Cole and Hetland (2016) using numerical experiments found that increase in freshwater discharge alters the net mixing response within a river plume due to enhanced shear mixing in the near-field region in a rotating envi-

ronment. This increased mixing in the near-field region can explain the similar sediment loads recorded in the case of model runs with large discharges owing to reduced mixing in the near-field region.

In the geostrophic far-field region, both the riverine and bed-sourced sediment transport in our study were found to be directed out of the forest, indicating an ebb-dominant asymmetry. This ebb dominance of the mangrove fringe regions (transition zones between the forest and mudflat) has been previously seen in many studies and has been attributed to friction caused by the vegetation (Mazda et al., 1995; Bryan et al., 2017).

Wind speeds of $5\,\mathrm{m.s^{-1}}$ were sufficient to change the structure of the far-field and mid-field regions of the plume. This change in the plume structure due to winds has been studied extensively (e.g. Kourafalou et al., 1996; Warrick et al., 2007). The majority of the sediment transport away from the river mouth (in the mid- and far-field region) was dominated by the direction of the wind, while closer to the river mouth, the plume retained its structure and was less sensitive to winds. This result is consistent with various previous studies conducted to study the influence of wind on the river plumes (e.g. Masse and Murthy, 1992; Münchow and Garvine, 1993).

Upon doubling the wind velocity ($10\,\mathrm{m.s^{-1}}$), in addition to increased total sediment transport mass loads, the dynamics of the river plume were significantly altered. Relative to the cases with $5\,\mathrm{m.s^{-1}}$ wind velocities, the river plume became more elongated. The presence of an elongated bulge region within a river plume under strong winds is consistent with the previous river plume studies such as Hickey et al. (1998). Within the river plume, the direction between the bottom and surface layer currents is reversed in the presence of strong winds. This result is consistent with Alekseenko and Roux (2019), who, using numerical methods, concluded that in shallow regions, strong winds

lead to enhanced stress differential and generation of bidirectional exchange of flows.

In our model simulations, wind stress was found to be one of the major controlling factors of sediment deposition in the case of $35\,m^3.s^{-1}$ river discharge scenario. This result is similar to Marques et al. (2009), who studied the dynamics of the Patos Lagoon coastal plume using 3-D numerical experiments and found that while winds become a primary contributor of the transport, the Coriolis force and bed shear stress become secondary influences in the case of low discharge plumes and vice versa. On the other hand, in our model simulations with river flows of $175\,m^3.s^{-1}$ and $480\,m^3.s^{-1}$, a combined influence of Coriolis, bed shear stress (impacted by vegetation), and turbulence (in the near-field region of the river plume) formed the principal dynamical processes controlling the sediment transport.

Analysis of total sediment fluxes along the edge of the eastern mangrove forest (not shown) revealed that while the direction of sediment fluxes remained the same, the magnitudes decreased. This decrease in sediment flux magnitudes in the eastern mangrove forest can be attributed to the reduced contribution of the riverine sediment as expected due to Coriolis (Southern Hemisphere). Interestingly, in model simulations with westerly winds, as the sediment plume was now pushed into the eastern forest (Figure 3.6), the magnitudes were only slightly increased. This modest increase to the total sediment fluxes can be explained by an increase in riverine sediment (as expected due to the surface layer wind stress); however, the presence of vertical advective fluxes during the absence of Coriolis (see Van Leeuwen and De Swart, 2002) inhibits the transport of bed-sourced sediment into the forest.

The results from this idealized model study provide insight into the effects of discharge and winds on sediment transport within a river plume in

a mangrove environment. Representing the presence of mangrove trees and roots using bottom drag enables us to capture the critical feedback mechanisms within the mangroves with higher computational efficiency (Horstman et al., 2015); however, detailed understanding of the modifications to the turbulent fields obtained using vegetative stems is neglected. The present study also neglects flocculation processes, noting that floc size has been shown to vary substantially along tidal rivers (MacDonald and Mullarney, 2015). Further work could incorporate the turbulence-induced aggregation and/or break up of flocs, which will thus affect settling velocity and transport of particles. Additionally, the effect of wind waves on the total sediment transport patterns is not incorporated.

3.5 Conclusions

We examined the response of a sediment river plume to variation in discharges and surface winds using an idealized 3-D model. Owing to elevated sediment inputs, mangrove vegetation in the Firth of Thames, New Zealand (Figure 3.9b) has rapidly expanded over recent decades in contrast to the global trend of mangrove decline. Results from this idealized study are consistent with the satellite images of this rapid progradation of mangroves closer to the river mouth (Figure 3.9b), in that sediment deposition primarily occurs in the highly dynamic near-field region close to the river mouth. The modeled river plume showed that vegetation significantly altered the riverine and bed-sourced sediment as the underlying drag influenced the net sediment transport through the transect. For very high discharge events, turbulence at the edge of the forest retains sediments in suspension, longer ebb duration, and strong plume momentum drives sediment through the forest onto the tidal flat offshore (Figure 3.9d).

This study revealed the contrasting impacts of easterly and westerly wind

directions on the dynamical properties within the river plume and found that major alterations to the wind magnitudes and direction can reverse the direction of the sediment transport. Understanding hydro-morphodynamics is crucial to restoring these ecosystems and influencing their growth. Within a mangrove forest, the interactions between the fluvial and marine processes in river flows and winds play a crucial role in controlling sediment deposition and erosion patterns. Results presented in this study can help enhance our ability to predict the evolution of mangrove vegetation by the influence of river flows and winds on the sediment supply.

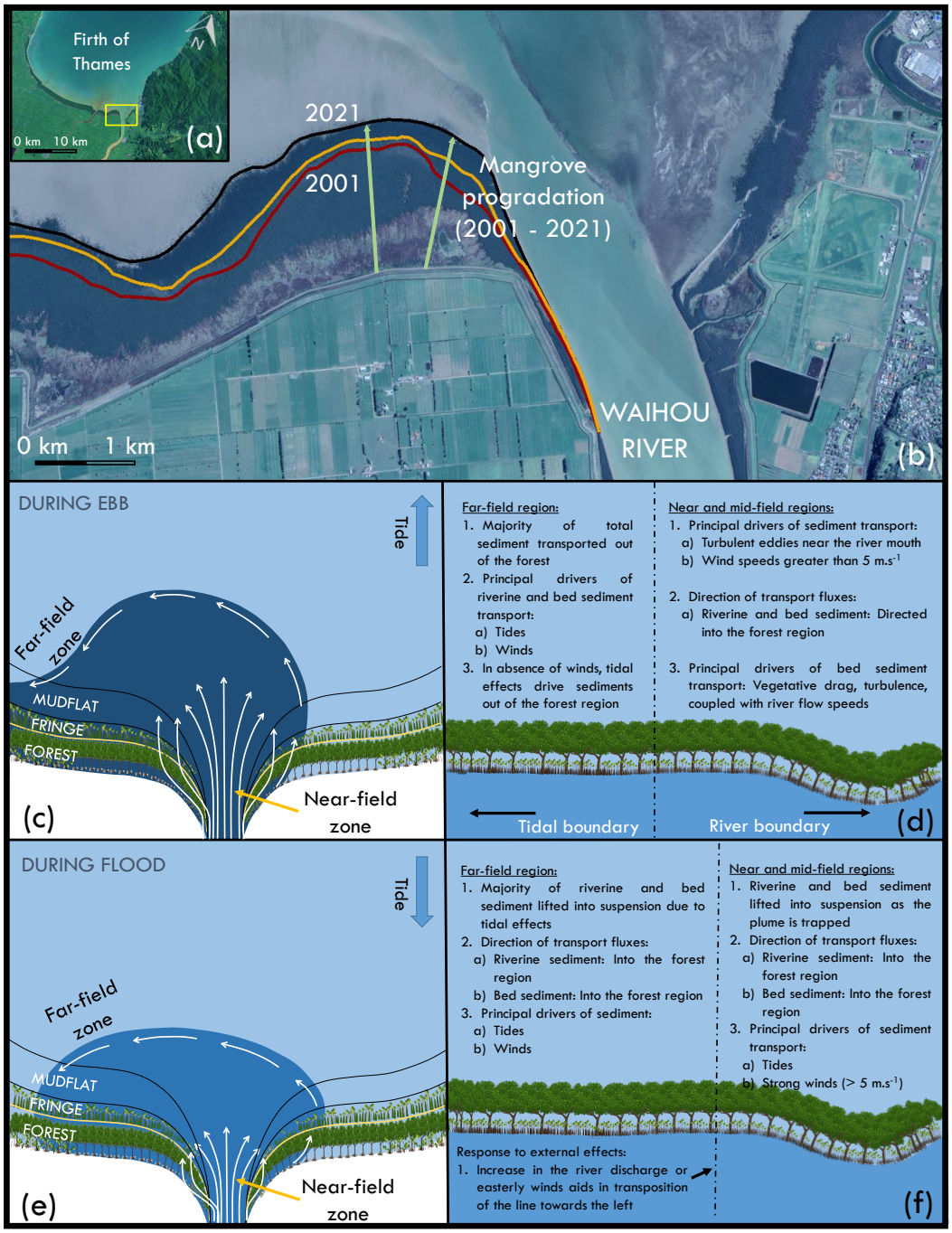

Figure 3.9: Inset (a) Firth of Thames shows the Waihou river's location (yellow rectangle). Panel (b) shows the mangrove progradation traced based on the Landsat imagery (2001 - 2021) obtained from the U.S. Geological Survey. Thick lines represent the extent of mangroves in 2001 (thick red line), 2011 (thick orange line), and 2021 (thick black line). Thick green arrows represent the direction of mangrove progradation over time. Panels (c) and (e) show the plume extent of the riverine sediment plume during the ebb and the flood stages of the tidal cycle. Panels (d) and (f) show the conceptual diagram along the transect considered in this study and the various dynamics and contributions from the external forces towards sediment transport mechanisms within the different environments of a river plume.

Chapter 4

Coalescence of buoyant river plumes and the implications for sediment transport into a coastal mangrove environment

Contribution of authors

Chapter 4 duplicates a paper of the title "Coalescence of buoyant river plumes and the implications for sediment transport into a coastal mangrove environment" by Hemanth Vundavilli, Julia C. Mullarney, and Iain T. MacDonald, which was submitted to *Estuarine, Coastal and Shelf Science* in 2022. The majority of text and figures are identical to the initially submitted version, except for the relabeling of figures, tables, equation numbers, and changes as suggested by the examiners of this thesis and the ongoing peer-review process. Along with modifying the idealized numerical model using Delft3D, I wrote MATLAB scripts to process and analyze the model data. Along with the preparation of initial and subsequent drafts, I prepared all the figures for this manuscript. My co-authors, Julia C. Mullarney and Iain T. MacDonald edited my drafts along with providing helpful comments and direction.

Abstract

We used idealized numerical experiments to investigate how the interactions of coalescing buoyant river plumes with mangrove vegetation affected sediment transport and deposition in the coastal zone. Our model system based on the Firth of Thames (FoT) in the North Island of New Zealand was designed to represent two mangrove-lined rivers debouching into a coastal bay. Sediment transport patterns into the three adjacent mangrove forest regions (central, western, and eastern) are assessed. The interactions between the buoyant river plumes resulted in a coalesced river plume mass that flowed along the central mangrove forest between the rivers. Both the rivers affect each other, and, consequently, the dominant contributors to the total sediment transport into the mangrove forests varied as a function of both the total and the relative flows through the two rivers. Aided by the Coriolis and river momentum, the eastern river dominates sediment transport and dynamics in the system for small and medium flows through the western river. Conversely, as the spatial extent of the western river plume extended for large flows, sediment associated with the western river dominated the total sediment fluxes into the mangroves. Analysis of sediment transport fluxes along the central mangrove forest revealed significant sediment accretion into the mangrove forests lining the river mouth, with modest deposition in the intermediate regions along the central forest, consistent with the satellite imagery of the FoT. Additional analysis investigating the influence of winds revealed that within the coalesced mass, as the along-shore transport of the dominant eastern river increased during easterly winds, the magnitude of total sediment fluxes into the central and eastern forest was the largest.

4.1 Introduction

Buoyant river plumes, which form when the riverine freshwater meets saline coastal waters, are a region of enhanced transfer of momentum, nutrients, and sediments (Jickells, 1998). The shape and propagation of a buoyant river plume are influenced by a river's interaction with coastal currents (e.g. Fong and Geyer, 2002), Earth's rotation (e.g. Garvine and Monk, 1974), and external factors such as the winds (e.g Fong and Geyer, 2001). Wright (1977) compared multiple river plume systems across the world and concluded that that sediment dispersal within a river plume is controlled by: (1) turbulence generated by the shear stresses within a water column, (2) buoyancy owing to the density differences; and (3) the physical properties of sediment particles. As the sediment eventually settles, these processes directly contribute to the long-term morphological evolution of coastlines and deltas (Paola, 2000).

Aquatic vegetation such as mangroves (which often line tidally influenced river banks in tropical and subtropical environments) have been found to modify velocity fields substantially (Nepf, 2012b), generate small-scale turbulence within the aquatic environments (Norris et al., 2021), and subsequently influence the overall hydrodynamics of the region. Previous studies in mangrove environments have found that the presence of mangroves can lead to both erosion and accretion in close proximity (Mullarney et al., 2017).

The width of the vegetative cover and geometry of mangroves strongly dictate the drag within the vegetation (Mazda et al., 1997) and this vegetative drag alters the tidal asymmetry within their environments by creating an imbalance in the maximum flow speeds. In particular, the forest and mudflat regions turn into flood-dominant zones owing to low ebb speeds induced by the vegetative drag; conversely, the highly turbulent fringe region (the transition zone between the forest and the intertidal flat) becomes ebb-dominant

(Mazda et al., 1995).

Using a 3-D numerical model of a mangrove-lined river debouching into a coastal bay, Vundavilli et al. (2021) explored the influence of mangrove vegetation (represented by a Chézy coefficient) on river plumes and associated sediment transport patterns. In their model, which was an idealized version of the Firth of Thames mangrove forest located in the North Island of New Zealand, they observed that while sediment deposition occurred in the forest and tidal flats region of the model domain, the fringe regions experienced erosion. In the model simulations conducted with no winds, sediment deposition in the western side of the model domain was larger than the eastern side, owing to the influence of Coriolis (Southern Hemisphere). Principal momentum balances were between the bottom shear stress (enhanced by the presence of vegetation) and baroclinic pressure gradient which largely controlled the sediment deposition in the riverine sections of the domain. Close to the river mouth, during ebb tide, the barotropic and baroclinic pressure gradients coupled with Coriolis acceleration help deliver sediment to the forest and mudflat regions. In the mid-field regions of the river plume, the magnitudes of bed elevation changes were smaller due to increased Coriolis acceleration which arrested the spreading of the river plume. In the shallow forested regions, stronger tidal influence helped deposit sediments into the forest.

In a subsequent modeling study (Chapter 3), we investigated how varying the forcing factors of riverine discharge and wind velocities influenced sediment transport in the system and consequently assessed total sediment transport and, in particular, how the relative contributions of riverine and bed-sourced (legacy) sediment varied over different sections of the mangrove forest. In their study, they found that the dominant contributors to the total sediment transport changed along the regions of the river plume: Equal contributions from the riverine and bed-sourced sediment dominated the total sediment trans-

port in the near-field region of the plume, and the sediment transport was found to be directed into the forest region, indicative of an accretionary environment. Furthermore, while the mass loads (directed into the mangrove forest) increased with an increase in riverine discharge, for the very large flow events, sediment mass loads were relatively similar as the river sediment plume carried sufficient momentum to push sediment through and out of the forest front. The presence of strong winds were able to modify sediment transport in the near-field region by overcoming the momentum carried by the river in the far-field region; however, sediment transport was controlled by both the tidal effects and wind stress. Additionally, the transport direction of the sediment plume was influenced by the strong winds.

The aforementioned studies help explain the principal underlying dynamics and quantitative estimation of sediment deposition patterns for a single riverine plume. However, river plumes in nature may often occur in close proximity. Despite observations of coalescing river plumes through remotely sensed imagery (Warrick and Fong, 2004), studies concerning the physics of river plume-to-plume interactions within specific coastal regions and the consequences of these interactions for sediment transport mechanisms are relatively less explored. As rivers form the primary mechanism through which sediment is transported to the coasts (Syvitski, 2003), it is critical to understand how plume-to-plume interactions influence sediment transport in the presence of mangrove vegetation.

In this study, using an idealized 3D numerical model, we aim to understand how the coalescence of two river plumes alters the morphological evolution of a mangrove system. In particular, we aim to investigate how coalescence alters the dynamics and the corresponding sediment deposition patterns within the adjacent mangrove forests. Section 4.2 of this manuscript describes the numerical model and the corresponding model scenarios undertaken in this

study. The dependence of sediment fluxes on the relative plume fluxes and winds is described in Section 4.3, and the implications of the results in this study are presented in Section 4.4. Lastly, conclusions are presented in Section 4.5.

4.2 Methods

4.2.1 Numerical model development

The numerical model used in this study was developed using the Delft3D modeling suite (Deltares, 2017). The Delft3D software package has been successfully applied for simulating hydrodynamics, sediment dynamics, and morphological processes (e.g. Lesser et al., 2004). The Delft3D flow module, which determines the flow characteristics by solving three-dimensional unsteady shallow-water equations under the Boussinesq assumption, is coupled to the sediment transport morphological model, which updates the bed simultaneously with the hydrodynamics (Roelvink and Van Banning, 1995).

4.2.1.1 Model setup

Numerical simulations in this study were undertaken in a model domain designed as an idealized version of the Firth of Thames located in the North Island (FoT, [S37°12′ E175°30′]) of New Zealand. The Waihou, Piako, and Waitakaruru rivers enter the FoT from the southern region and have experienced rapid colonization of mangrove vegetation (*Avicennia marina*) over the last 60 years due to sediment input associated with deforestation and land-use changes (Lovelock et al., 2010). This study focuses on the two rivers, the large river Waihou (hereafter referred to as the eastern river) and a smaller river representing the Piako (hereafter referred to as the western river), which exist in close proximity and generate persistent freshwater and sediment plumes.

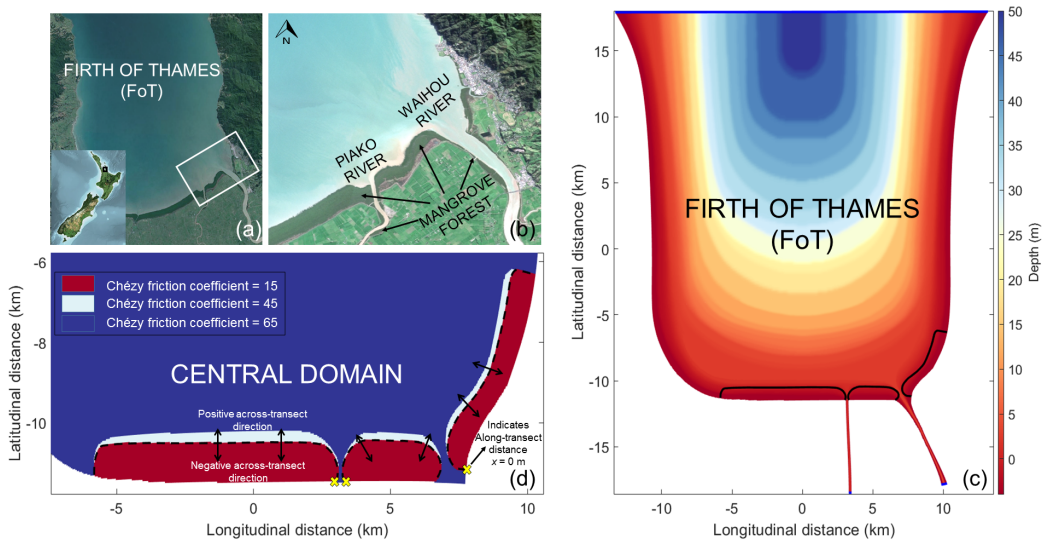

Figure 4.1: Panel (a) shows the location of the Firth of Thames (thick black box) field site on the map of New Zealand (inset), (b) satellite image of the Waihou and Piako river sediment plumes and mangroves. Panel (c) shows the idealized symmetric bathymetry, transects along the western, central, and eastern forest edge (thick black line), and (d) spatially varying Chézy coefficient used in the model central domain to represent vegetation. Thick blue lines in Panel (c) represent tidal (top) and river (bottom) boundaries. The transects are shown by thick black lines in panel (d). In panel (d), the black arrows and yellow crosses depict the across-transect directions and origin for the along-transect distances, respectively.

4.2.1.2 Model grid and bathymetry

The model used in this study retains the same outer domain as the model described in Chapter 3. However, two rivers are introduced at the eastern side of the southern end of the domain. The 3-D curvilinear grid is now decomposed into four domains to incorporate the additional river: The outer domain, which includes the tidal boundary with grid sizes varying from $\sim$ 500 m x 900 m near the tidal boundary to $\sim$ 218 m x 140 m near the domain decomposition boundary. The central domain, which encompasses the mangrove vegetation, was resolved into a grid resolution of $\sim$ 218 m x 140 m in the deeper sections of the domain to a refined resolution of $\sim$ 20 m x 15 m in the mangrove region. Lastly, the two lower domains, each encompassing the rivers, had a varying

resolution of $\sim$ 30 m x 30 m at the river boundary to $\sim$ 20 m x 15 m near the river mouth. The model was vertically resolved into five sigma layers of equal thickness (20% of the water depth). The vertical resolution of 5 sigma layers was deemed adequate to model plume coalescence following sensitivity analysis (Appendix B.1). To represent vegetation in our model simulations, a spatially varying Chézy coefficient was employed based on the literature values (Mazda et al., 1997). In the latitudinal direction from the forest to tidal flats, the Chézy coefficient varied from 15 $m^{1/2}.s^{-1}$ (corresponding to a $C_D = 0.044$) to 65 $m^{1/2}.s^{-1}$ ($C_D = 0.0023$) in the intertidal zone. A Chézy coefficient of 45 $m^{1/2}.s^{-1}$ ($C_D = 0.0048$) was used to represent the forest fringe (a $\sim$ 200-m thin transition zone between forest and intertidal zone).

4.2.2 Model parameters and boundary conditions

The Coriolis parameter in the model was set at -37° latitude in the model. The threshold depth in the model was set to 0.1 m, and the spatial discretization of momentum was set to a cyclic advection scheme. The background eddy viscosity and diffusivity were set to 1 m^2 and 0.1 m^2, respectively. All the remaining numerical parameters in this study were set to their respective Delft3D default values. To distinguish sediments (restricted to the Cohesive sediment class) and to have a detailed understanding of the sediment transport within each of the model domains, we label both the riverine (new sediments introduced at the river boundaries) and bed-sourced sediments (legacy sediments). An initial bed sediment thickness of 2 m was used. To reduce the computational time of each simulation, a Morphological Acceleration Factor (see Roelvink and Van Banning, 1995; Lesser et al., 2004) or MORFAC of 12 was used to simulate $\sim$ 3 months of morphological changes. In each of the simulations undertaken in this study, the northern tidal boundary was forced with an M2 astronomic tide of 1.3 m amplitude and a constant salinity of 31 ppt. Each of the rivers was forced with a freshwater discharge and riverine sediment. To achieve a quasi-steady state, model simulations were run for an initial spin-up

period of 7 days with freshwater input but no sediment. The model simulations were conducted for another 7-day period with the sediment input through each river boundary. A model timestep of 0.01 min was used to satisfy the Courant-Friedrichs-Lewy condition.

4.2.3 Modeled scenarios

A total of 19 modeled scenarios were undertaken for this study (Table 4.1). These were selected to encompass the range of observed river flow conditions for the western and eastern rivers in the Firth of Thames and explore how the ratio of river fluxes controls the plume and deposition patterns. For both rivers, a relationship between discharge and suspended sediment concentration was constructed based on environmental data recorded at their respective upstream boundaries at $\sim 4\,\mathrm{km}$ by the Waikato Regional Council for the period 1981 - 2022, and simulations were conducted using the 50^{th}, 90^{th}, and 99.99^{th} percentiles of the frequency distribution. An additional four simulations, with forcing equivalent to Run 11 (Table 4.1) and a continuous wind of speed of $5\,\mathrm{m.s^{-1}}$ (based on the climate data recorded for the Firth of Thames averaged over a year) were carried out for northerly, easterly, westerly, and southerly wind directions to provide an indication of how sensitive the results are to wind forcing. Modeled scenarios are listed in Table 4.1.

4.3 Results

In order to examine how the coalescence of river plumes affects sediment transport into the vegetation, we consider fluxes across three transects along the west, central, and east sides of the model domain (Figure 4.1d). The western and eastern transects defined in this study begin from the raised river banks in the river mouth and extend along the edges of the western and the eastern mangrove forests, respectively, while the central transect starts at the raised eastern river bank and extends along the edge of the central mangrove forest

Table 4.1: Model simulations undertaken in our study. Q_W, C_W, Q_E, and C_E are western riverine discharge, sediment concentration through the western river boundary, eastern riverine discharge, sediment concentration through the eastern river boundary, respectively.

		Western river		Eastern river		Winds	
	Run no.	Q_W ($m^3.s^{-1}$)	C_W ($kg.m^{-3}$)	Q_E ($m^3.s^{-1}$)	C_E ($kg.m^{-3}$)	Wind speed ($m.s^{-1}$)	Wind direction (° from)
No wind	1	7	0.4	0	0	0	-
	2	20	0.6	0	0	0	-
	3	100	1.6	0	0	0	-
	4	0	0	35	0.4	0	-
	5	0	0	60	0.5	0	-
	6	0	0	250	1.8	0	-
	7	7	0.4	35	0.4	0	-
	8	7	0.4	60	0.5	0	-
	9	7	0.4	250	1.8	0	-
	10	20	0.6	35	0.4	0	-
	11	20	0.6	60	0.5	0	-
	12	20	0.6	250	1.8	0	-
	13	100	1.6	35	0.4	0	-
	14	100	1.6	60	0.5	0	-
	15	100	1.6	250	1.8	0	-
Winds	16	20	0.6	60	0.5	5	0
	17	20	0.6	60	0.5	5	90
	18	20	0.6	60	0.5	5	180
	19	20	0.6	60	0.5	5	270

for the eastern river. Following the methodology applied in Chapter 3, we analyse the sediment fluxes for each sediment type (riverine and bed-sourced) independently in order to study the links between riverine flows, wind stress, and sediment transport in the presence of vegetation and tidal effects. We evaluate the instantaneous, time-integrated sediment transport fluxes (Q) and net mass transfer loads (M) along the western, eastern, and central transects as:

$$Q(t) = \int_0^{h(t)} c(t,z) \cdot v(t,z).dz, \tag{4.1}$$

where, $c(t,z)$ is the instantaneous sediment concentration (kg.m^{-3}), $v(t,z)$ indicates the horizontal across-transect velocity at height z and time t, and h is the height of the water column.

$$Q = \int_0^{T} Q(t).dt, \tag{4.2}$$

where, Q is the time-integrated sediment transport flux.

An integration of Q along the total length of the transect yields:

$$M = \int_0^{X} Q.dx, \tag{4.3}$$

where, X is the total length of the transect in the along-transect direction. Throughout this study, positive fluxes (Q) and mass loads (M) correspond to sediment directed out of the forest, while negative magnitudes correspond to sediment directed into the forest region.

4.3.1 Sediment plume coalescence

The effect of plume interactions on the surface layer salinity, river sediment concentration, and velocities at the peak ebb and peak flood taken inside the eastern river mouth (defined by longitudinal distance of $\sim$ 9 km and latitudinal distance of $\sim$ -11 km, Figure 4.1c) are shown in Figure 4.2 for the model runs

for Run 2 and Run 11 (Table 4.1). In our numerical model, in the cases with no flow through the eastern river (single river flow, Run 2, Table 4.1), during the peak ebb stage of the tidal cycle, the western river plume was found to be radial in shape, expanding $\sim 2\,\text{km}$ into the central domain with a salinity range of 15 - 20 ppt. As the plume debouched into the model domain, the flow vectors were oriented towards the northern tidal boundary near the river mouth and spread into the river mouth of the second river boundary (Figure 4.2a). This intrusion of river plume into the river mouth in its proximity has been seen in Gong et al. (2019), who attributed the intrusion of one river plume into the other river to the baroclinic component, which aids in intrusion and downstream transport of one river into the other. Surface flow speeds ranged from $\sim 0.6\,\text{m.s}^{-1}$ close to the river mouth to $\sim 0.3\,\text{m.s}^{-1}$ in the deeper sections of the model domain. When two rivers are considered, the spreading patterns of both the sediment plumes were altered in our model simulations. In particular, as the strongly flowing eastern river plume interacted with the western river plume, both the plumes radially spread into the coastal domain creating a region of lower salinity along the central mangrove forest, with the eastern river expanding for over $\sim 4\,\text{km}$ (Figure 4.2b). As a result of this collision of salinity fronts, the lateral sediment plume expansion for both plumes was severely inhibited along the collision boundary (also seen previously by Warrick and Farnsworth 2017).

During peak flood, plume expansion is limited by the presence of oncoming tidal currents. In the case of a single river plume system (Run 2, Table 4.1), the western river plume spreads laterally. However, in the two river case, as the lateral expansion is halted under medium flows (Run 11, Table 4.1), the two plumes no longer maintain their initial structure but instead coalesced into a single water mass with a low salinity range of 10-16 ppt resulting in accumulation of river sediment along the central forest with high sediment concentration near the edges (Figure 4.2d). The coalesced plume mass was

mostly composed of the eastern river due to the larger river flow, angled river geometry, and deflection to the left due to Coriolis (Southern Hemisphere). Analysis of river sediment concentration in the water column (not shown) across the centers of each river plume showed that the large eastern river plume occupied the surface region of the water column while the smaller western river plume was pushed to the bottom.

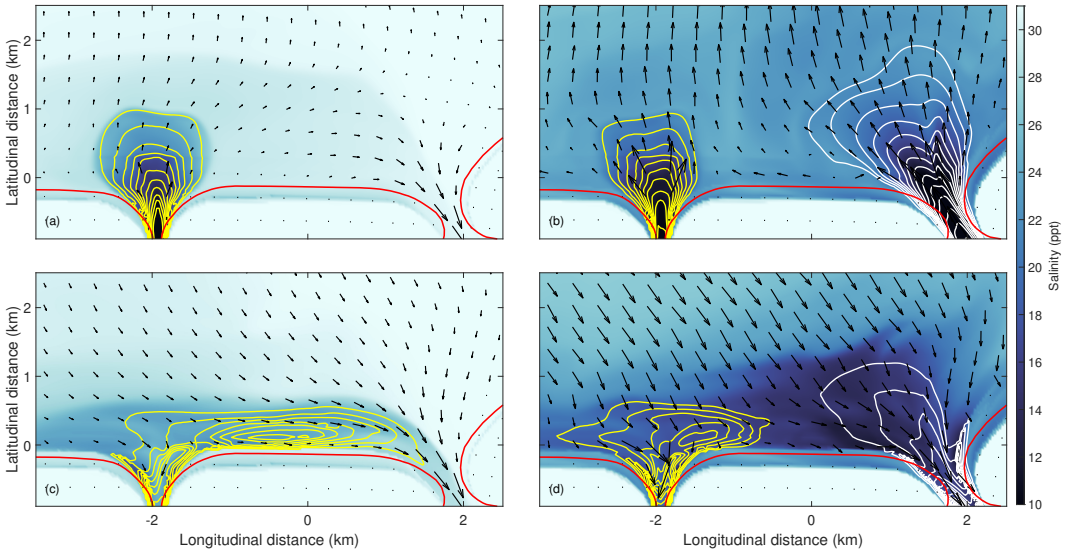

Figure 4.2: Model snapshots of surface layer riverine sediment concentration (contours), salinity (colorbar), and velocity (arrows) at different tidal stages. The single river scenario (Run 2, Table 4.1) is shown in panels (a) at peak ebb and (c) at peak flood stages of the tidal cycle. A multiple river scenario (Run 11, Table 4.1) is shown in panels (b) at peak ebb and (d) at peak flood stages. Thick yellow contour lines (contour interval: 0.02 kg.m^{-3}) and white contour lines (contour interval: 0.1 kg.m^{-3}) show the western and the angled eastern riverine sediment concentrations, respectively. The thick red lines show locations of the transects.

4.3.2 Dependence of plume coalescence on the relative river inputs

To quantify the nature of plume interactions for the model runs undertaken in this study, we introduce the tidally averaged non-dimensional plume collision index (R_P) defined as:

$$R_P = \begin{cases} 0, \text{ if } A_W \text{ or } A_E = 0 \\ \frac{A_I}{A_W + A_E}, \text{ if plumes coalesce} \\ 1, \text{ if one plume overlaps the other} \end{cases} \tag{4.4}$$

where A_W, A_E correspond to surface area of the polygon defined by the sediment plumes formed the western and the eastern river, respectively. A_I is the surface area of the polygon defined by the intersection of the plume boundaries with sediment concentrations in the surface layer greater than $0.01\,\mathrm{kg.m^{-3}}$. The non-dimensional number R_P represents the degree of plume coalescence with values ranging from 0 (no coalescence) to 1 (complete overlap of one plume over the other). An overview of the plume coalescence and corresponding plume collision indices for the surface layer is shown in Figure 4.3 for the model runs when flow rates through the rivers were greater than zero.

A comparison of plume collision indices (R_P) for low, medium, and large flows through the western river yielded positive linear relationships for flow increases through the eastern river (Figure 4.3a-g). However, in the cases with low and medium flows through the western river, the prominent bulge of the eastern river plume completely envelops the western river (i.e. $R_P = 1$; Figure 4.3f and i). Conversely, when the western river was forced with a large flow (Run 15, Table 4.1), the plume collision index (R_P, Figure 4.3c) was found to be 0.23 (decreased from 1 as noted for Runs 6 and 12), indicating influence of both plumes within the coalesced mass due to greater spatial extent of plume formed by the western river. The influence of eastern river flow on the plume coalescence was stronger than for the western river flow. For example, increasing the flow through the western river, when low (Runs 7, 10, and 13, Table 4.1) and medium flows (Runs 8, 11, and 14, Table 4.1) were forced through the eastern river led to a decrease in the plume collision indices (R_P) in comparison to those obtained when eastern river was varied (Figure 4.3a and b).

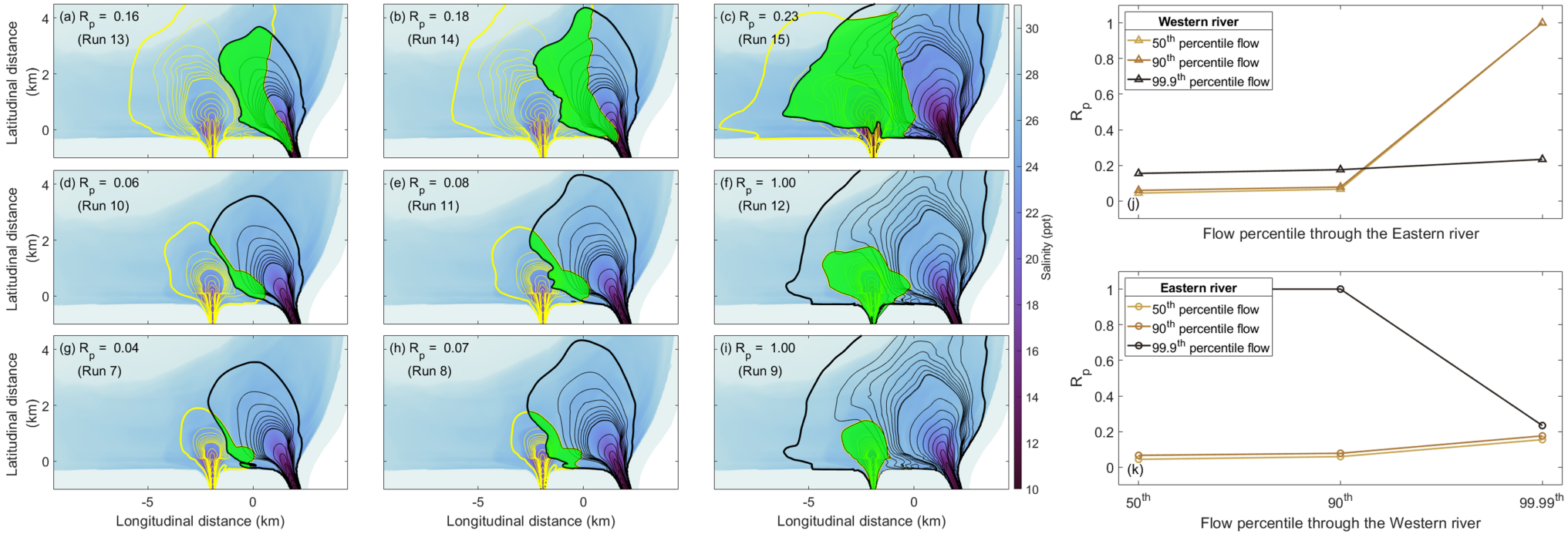

Figure 4.3: Plume collision indices (R_P, Equation 4.4) for the model Runs 13-15 (Panels a-c), Runs 10-12 (Panels d-f), Runs 7-9 (Panels g-i) for western river (yellow contours) and eastern river (black contour lines). Panel (j) and (k) show the relationship between the plume collision index and the tidally averaged flows through the eastern river (triangles) and the western river (circles), respectively. Thick yellow and black contours show the plume boundaries taken at $0.02\,\mathrm{kg.m^{-3}}$ for the western and eastern rivers, respectively. Shaded green regions show the plume interaction areas (A_I) for the respective model runs.

4.3.3 Tidally integrated sediment fluxes

The tidally integrated sediment fluxes of the river, bed sediment, and the total sediment fluxes through the central, western, and eastern mangrove forests for the Run 11 scenario (Table 4.1) are shown in Figure 4.4.

4.3.3.1 Flux through the central mangrove forest

For Run 11 (medium flows through both the rivers, Table 4.1), the relative importance of the sediment type varied along the central mangrove forest. In particular, bed sediment from the western river was the dominant contributor close to the river mouth ($0 \lesssim x \lesssim 1000\,\mathrm{m}$, Figure 4.4b) with contributions greater than the river sediment by nearly $\sim 90\%$. Farther along the central forest closer to the eastern river ($x \gtrsim 3800\,\mathrm{m}$), bed sediment from the eastern river and the Firth of Thames outer bay were the dominant contributors to the total sediment transport and were directed into the forest lining the river banks (Figure 4.4b). The directional trends along the central mangrove forest remained similar near the rivers. In particular, as the plumes debouched into the central domain, the rivers pushed sediment into the forest close to their respective river mouths, resulting in negative fluxes (Figure 4.4b). In the region between the rivers ($1000\,\mathrm{m} \lesssim x \lesssim 3800\,\mathrm{m}$), sediment transport was directed into the forest region, although the magnitudes significantly decreased (Figure 4.4b inset). For distances between $1000\,\mathrm{m} \lesssim x \lesssim 2000\,\mathrm{m}$, bed sediment from the outer bay (Firth of Thames) contributed nearly 80% of the total flux, with a further 20% resulting from central bed sediments, with negligible contributions by the river sediment carried by either rivers. In the region defined by ($2000\,\mathrm{m} \lesssim x \lesssim 3800\,\mathrm{m}$), total sediment transport was entirely dominated by the bed sediment from the Firth (Figure 4.4b inset).

4.3.3.2 Flux through the western and eastern mangrove forests

Shallow regions inside the forest represented by along-transect distances $x \gtrsim 2000\,\mathrm{m}$ remained dry throughout the model simulations for the western and eastern mangrove regions (Figure 4.4a and c). Over a tidal cycle, sediment transport close to the river mouth for western ($0 \lesssim x \lesssim 500\,\mathrm{m}$, Figure 4.4a) and eastern mangrove forests ($0 \lesssim x \lesssim 1000\,\mathrm{m}$, Figure 4.4c) was primarily directed into the forest with dominant contributions by the sediment associated with the western river and eastern river, respectively. The bed sediment was found to be the dominant contributor to the total sediment transport along the western and eastern mangrove forests. While bed sediment from the western river dominated the sediment flux along the western mangrove forest (Figure 4.4a), bed sediment from the Firth along with modest contributions from the eastern river sediment dominated the fluxes along the eastern mangrove forest (Figure 4.4c). This change of principal contributors can be attributed to the deflection of the river plumes to the left of the model domain owing to Coriolis. Due to this deflection, the magnitude of river sediment fluxes was nearly ~ 10 times larger in the western river compared to the eastern river (Figure 4.4a and c).

4.3.4 The influence of flow variations on sediment transport

A comparison of model results with varying flows through the eastern river while medium flows through the western river were forced (Runs 10, 11, and 12, Table 4.1) are presented in Figure 4.5.

Along the central mangrove forest (located between the rivers), closer to the western river mouth ($0 \lesssim x \lesssim 500\,\mathrm{m}$), total sediment transport decreased with an increase in flow through the eastern river in our model simulations (Figure 4.5a). Conversely, in the region closer to the eastern river mouth (x

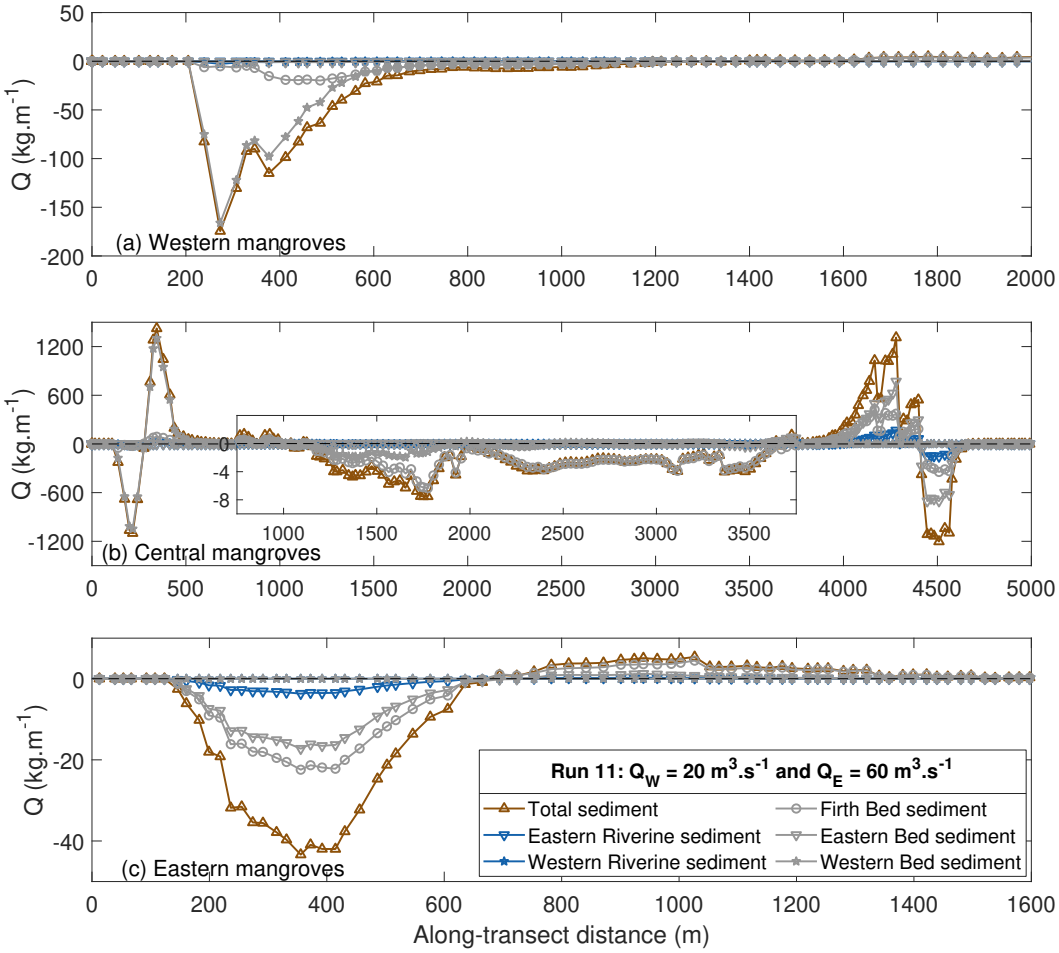

Figure 4.4: Across-transect sediment fluxes (Q) along (a) the western mangrove forest, (b) the central mangrove forest, and (c) the eastern mangrove forest for eastern river discharge and the western river discharges of $60\,\mathrm{m}^3.\mathrm{s}^{-1}$ and $20\,\mathrm{m}^3.\mathrm{s}^{-1}$ (Run 11, Table 4.1), respectively. Thick brown lines represent the total sediment flux, thick blue lines represent the corresponding fluxes for riverine sediment types, and thick grey lines represent the corresponding fluxes for bed sediment types. In our evaluations, positive and negative fluxes indicate sediment transport out and into the forest region, respectively. Along-transect distance of zero for the western and eastern mangrove forests correspond to the river mouth of the western river and eastern river, respectively. The along-transect distance of zero for the central mangrove forest corresponds to the river mouth of the western river. In our evaluations, positive and negative fluxes indicate sediment transport out of the forest and into the forest region, respectively. Inset shows the close-up of the modeled fluxes along the central mangrove forest for distances of $1000\,\mathrm{m} \leq x \leq 3500\,\mathrm{m}$.

$\gtrsim 3800\,\mathrm{m}$), the total sediment flux magnitudes increased by nearly 60% as the flow was increased from its 50^{th} percentile (low flow) to 90^{th} percentile (medium

flow). Furthermore, as the flow through the eastern river was now increased to its 99.99^{th} percentile (large flow), total sediment fluxes increased by an order of magnitude (Figure 4.5a). Total sediment fluxes were directed into the forest regions lining the river banks irrespective of the flow (Figure 4.5a). Farther away from the river mouths, sediment transport fluxes were instead found to be directed out of the forest. While the sediment transport direction out of the forest in the case of the eastern river ($3800\,\text{m} \lesssim x \lesssim 4400\,\text{m}$, Figure 4.5a) was due to the momentum carried by the eastern river, which helped push the sediment out of the forest front; on the other hand, in the case of the smaller western river ($500\,\text{m} \lesssim x \lesssim 650\,\text{m}$, Figure 4.5a), the sediment outflow can be also explained by the enhanced ebb dominance in the region.

Along the central mangrove forest, the relative importance of sediment source varied. In particular, closer to the western river ($0 \lesssim x \lesssim 500\,\text{m}$), bed sediment from the western river and the outer bay of the Firth were dominant contributors to the total sediment (Figure 4.5b and c). Interestingly, as the flow through the eastern river increased, while the river sediment contributions from the western river towards the total sediment flux decreased, whereas the bed sediment carried by the western river increased (Figure 4.5a). The contribution of bed sediment from the Firth, was found to be inversely proportional to the flow through the eastern river (Figure 4.5c). In the region midway along the central forest ($1000\,\text{m} \lesssim x \lesssim 3500\,\text{m}$), total sediment fluxes were directed into the forest for low and medium flows through the eastern river; however, overall magnitudes significantly decreased. For the low and medium flows through the eastern river, bed sediment from the Firth remained the dominant contributor to the total sediment transport (Figure 4.5a). Further increases in the flow through the eastern river (Run 8, Table 4.1), total sediment transport along the forest did not have a definitive direction.

Total sediment mass loads were integrated along the entirety of the cen-

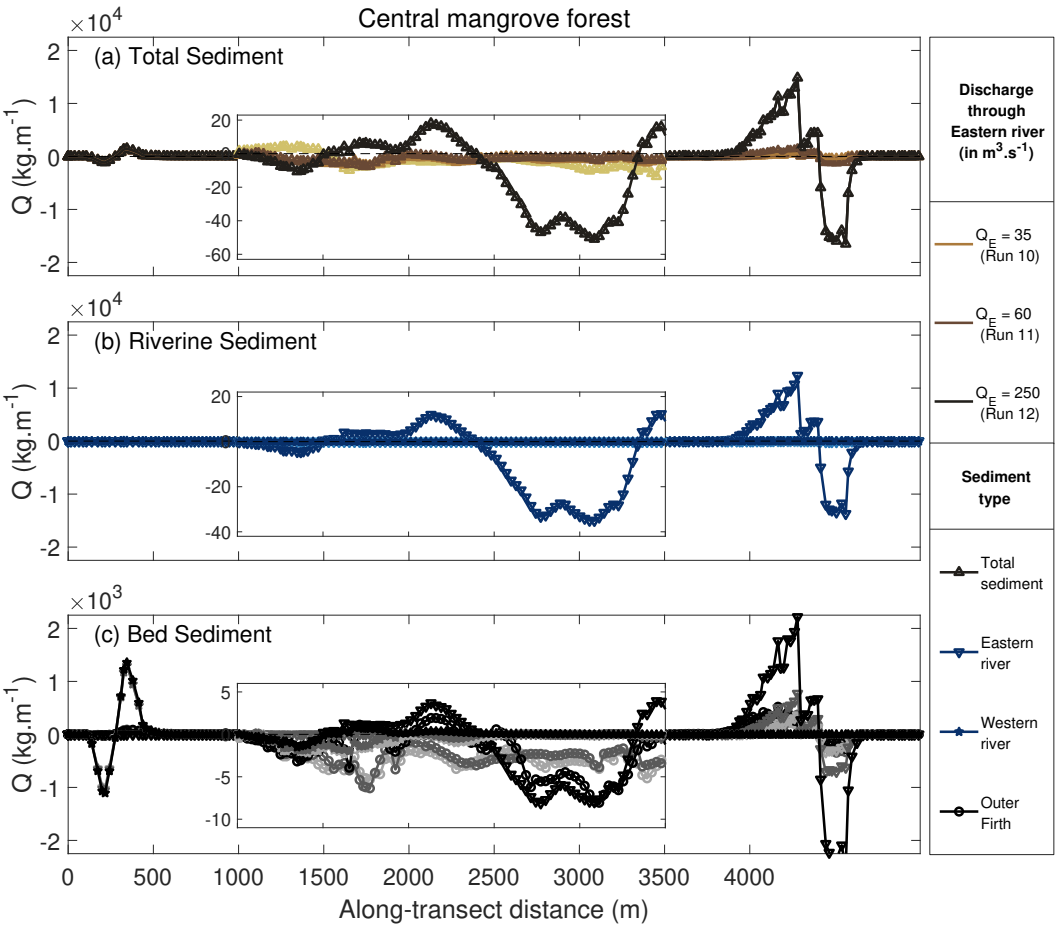

Figure 4.5: The comparison of the tidal integrated fluxes across the central mangrove forest (a) total sediment fluxes (brown lines), (b) riverine sediment fluxes (blue lines), and (c) bed sediment fluxes (gray lines) for eastern river discharge of $35\,\mathrm{m}^3.\mathrm{s}^{-1}$ (Run 10, Table 4.1), $60\,\mathrm{m}^3.\mathrm{s}^{-1}$ (Run 11, Table 4.1), and $250\,\mathrm{m}^3.\mathrm{s}^{-1}$ (Run 12, Table 4.1). Triangles, circles, and stars represent sediment associated with eastern river, Firth, and western river, respectively. Along-transect distance of zero corresponds to river mouth of the western river. In our evaluations, positive and negative fluxes indicate sediment transport out of the forest and into the forest region, respectively. Colors show individual discharge scenarios from Run 10 (lighter shades) to Run 12 (darker shades). Inset in Panel (b) shows the close-up of the modeled fluxes along the central mangrove forest for distances of $1000\,\mathrm{m} \leq x \leq 3500\,\mathrm{m}$. Note different y-axis scale in panel (c).

tral mangrove forest for Runs 10, 11, and 12 (not shown). Irrespective of the flow variations through the eastern river (Table 4.1), total sediment mass loads were directed into the mangrove forest, indicative of sediment deposition. As the flow through the eastern river increased from low to medium,

the magnitude of the total sediment mass loads through the central mangrove forest decreased by nearly $\sim 50\%$. As the flow was further increased (Run 12, Table 4.1), total mass loads increased by nearly ~ 4 times compared to that observed in the case of the medium flow rate (Run 11, Table 4.1). For small to medium discharges through the eastern river, bed-sediment from the Firth and western river were the dominant contributors to the total sediment mass loads; however, in the case of the large discharge scenario (Run 12, Table 4.1), river sediment from the eastern river dominated the total sediment mass loads with modest contributions from the remaining sediment sources employed in this study.

Tidally integrated fluxes along the western and eastern mangrove forests were directionally similar, irrespective of the flow variations employed through the eastern river (Figure 4.6a-f). The magnitude of total sediment fluxes increased for both the western (Figure 4.6a) and eastern mangrove forests (Figure 4.6b) as the flow through the eastern river increased. The magnitudes of total sediment flux were larger through the western mangrove forest than the eastern mangrove forest for low and medium river flows employed through the eastern river. The dominant sediment source contributors varied through both the western and eastern mangrove forests as the flows through the eastern river varied. In particular, bed sediment from the western river ($\sim 20\%$ of the total sediment transport) and the Firth ($\sim 80\%$ of the total sediment transport) were the major contributors to the total sediment along the western mangrove forest (Figure 4.6e). Furthermore, bed sediment from the Firth ($\sim 50\%$ of the total sediment transport) dominated total sediment transport with near similar contribution from the bed sediment transport by the eastern river ($\sim 50\%$ of the total sediment transport) along the eastern mangrove forest (Figure 4.6f). The influence of sediment from the western river on total sediment flux through the eastern mangrove forest was negligible ($\mathcal{O}(10^{-2})\,\mathrm{kg.m^{-3}}$) as the large eastern river plume arrests any movement of sediment from the western

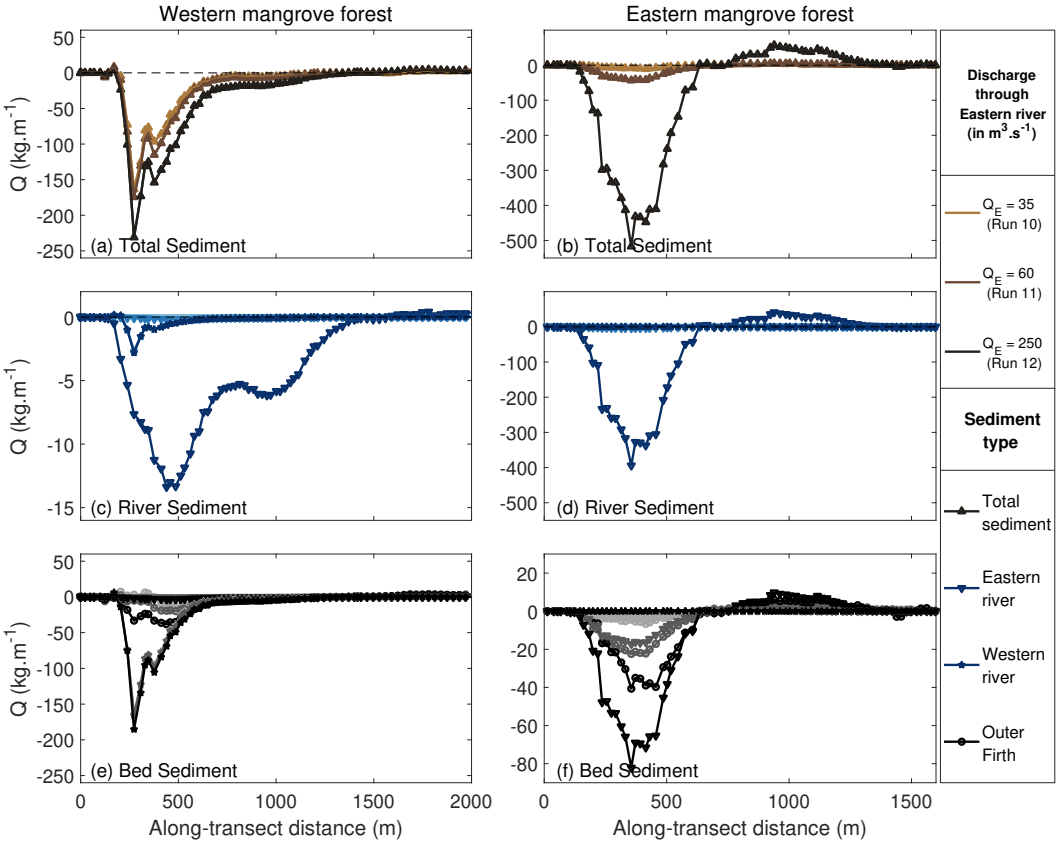

Figure 4.6: The comparison of the tidal integrated fluxes across the eastern and western mangrove forest (a) and (b) total sediment fluxes (brown lines), (c) and (d) riverine sediment fluxes (blue lines), and (e) and (f) bed sediment fluxes (grey lines) for eastern river discharge of $35\,m^3.s^{-1}$ (Run 10, Table 4.1), $60\,m^3.s^{-1}$ (Run 11, Table 4.1), and $250\,m^3.s^{-1}$ (Run 12, Table 4.1). Triangles, circles, and stars represent sediment associated with eastern river, the outer Firth, and the western river, respectively. Along-transect distance of zero for the western and eastern transects correspond to river mouth of the western river and eastern river, respectively. In our evaluations, positive and negative fluxes indicate sediment transport out of the forest and into the forest region, respectively. Colors show individual discharge scenarios from Run 10 (lighter shades) to Run 12 (darker shades). Note the change in y-axis scale between the panels.

river.

In the case of the large flow through the eastern river (Run 12, Table 4.1), river sediment carried by the eastern river dominated the river sediment flux along both the western and eastern mangrove forests (Figure 4.6c and d). The

magnitude of the river sediment through western and eastern mangrove forests increased by nearly $\sim 85\%$ and nearly 100 times, respectively. However, despite large flows through the eastern river, bed sediment from the western river and the Firth remained the dominant contributor to the total sediment transport through the western mangrove forest. Through the eastern mangrove forest, as expected, river sediment from the eastern river dominated total sediment transport (Figure 4.6b).

As the flows through the eastern river increased, total sediment mass loads (not shown) exhibited increased non-linearly. Total sediment mass loads along the western forest decreased by nearly $\sim 38\%$ when flow through the eastern river was increased from low to medium. With additional increases in the flow through the eastern river (Run 12, Table 4.1), the total sediment mass loads increased by $\sim 15\%$. Alternatively, as the flow through the eastern river increased, total sediment mass loads through the eastern mangrove forest increased, with dominant contributions from the river sediment carried by the eastern river and bed sediment carried by the Firth and river. This increase in total sediment mass loads can be explained by the increase in the plume collision indices (R_P) evaluated for runs 10, 11, and 12, indicating an increase of the eastern river's influence on the overall sediment dynamics of the system.

4.3.5 Plume coalescence under the influence of wind

The presence of $5\,\mathrm{m.s^{-1}}$ winds had varying effects on the river plumes in our model simulations (Figure 4.7). In particular, compared to the eastern river, the western river plume no longer retained its near-field structure as winds influenced the plume outflow (Figure 4.7a-e). On the other hand, as the momentum carried by the eastern river was sufficiently large, the wind had a minimal effect in the near-field region of the eastern river. Along the mid- and the far-field regions ($1\,\mathrm{km} \lesssim y \lesssim 2\,\mathrm{km}$ in the latitudinal direction), winds of $5\,\mathrm{m.s^{-1}}$ altered the structure of both plumes.

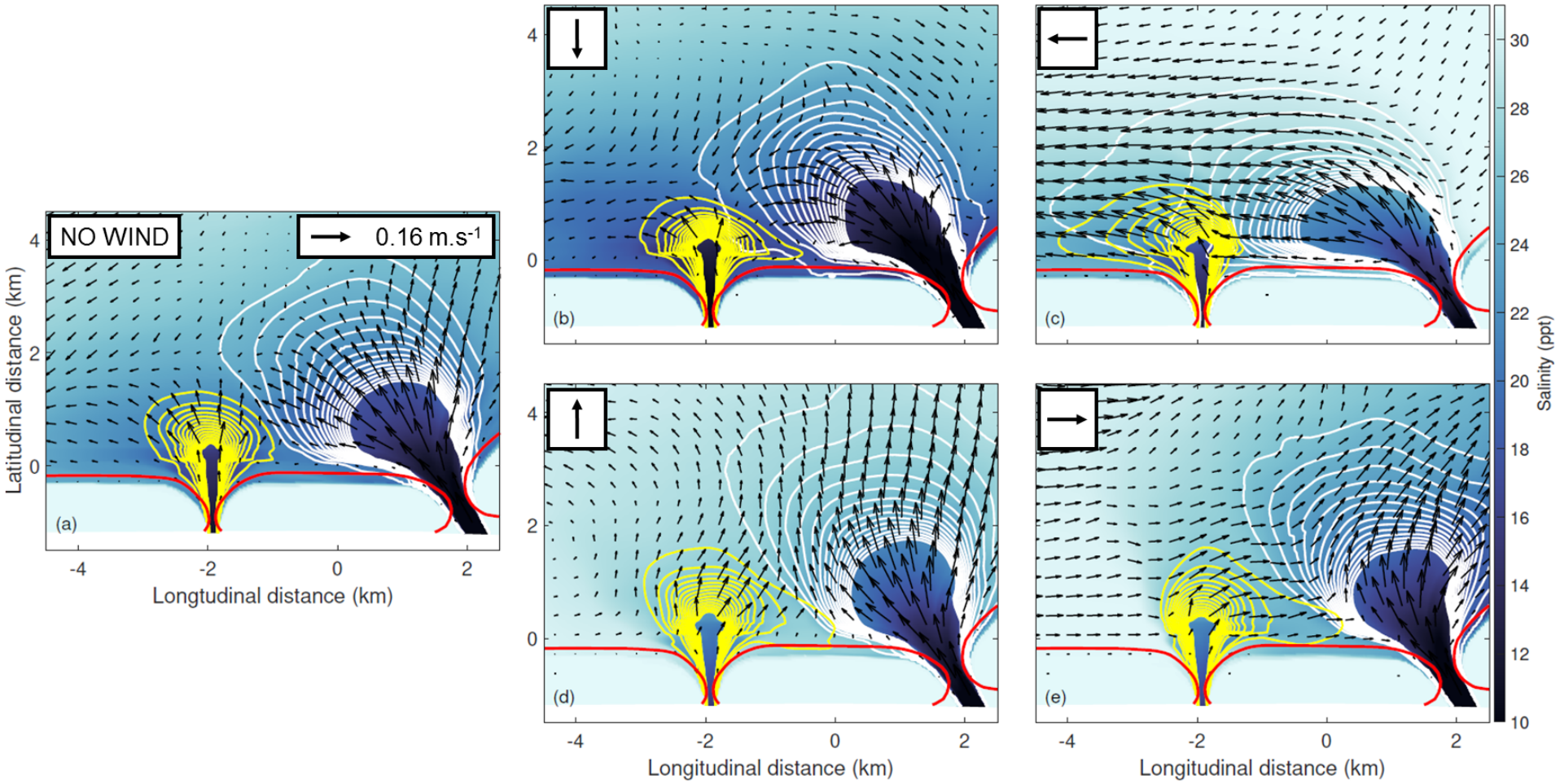

Figure 4.7: Comparison of the surface layer salinity, sediment concentration, and horizontal velocities averaged over a tidal cycle under the influence of wind (Runs 16-19, Table 4.1). Insets show wind direction (b) Northerly (0°), Panel (c) Easterly (90°), Panel (f) Southerly (180°), and Panel (h) Westerly (270°). Black arrows show the surface layer residual velocities. Thin contours show $0.02\,\mathrm{kg.m^{-3}}$ for western river (yellow) and eastern (white) rivers. The corresponding no-wind scenario is shown in Panel (a). The thick red lines show the location of the transects. Colorbar represents salinity in ppt.

Compared to the no-wind scenario, northerly winds arrested the movement of the river plumes (Figure 4.7a and b). The surface current residuals in the regions away from the river mouths were primarily directed into the central forest (Figure 4.7b). Easterly (90°) and westerly (270°) winds were dominant in enhancing the plume coalescence in our model simulations (Figure 4.7c and e). In particular, as winds blow from the east, the eastern river was further pushed towards the left (previously aided by Coriolis), enhancing the sediment plume interactions in the central domain while eclipsing the weaker western river plume (Figure 4.7c). Winds blowing from the west (270°, Figure 4.7e) of $5\,\mathrm{m.s^{-1}}$ were sufficient to overcome the influence of Coriolis and deflect the far-field regions of both the river plumes towards the right compared to the no-wind scenario (Figure 4.7e). Lastly, southerly winds (180°, Figure 4.7d) pushed both plumes towards the northern tidal boundary with residual velocity vectors (specifically in the far-field region of the river plumes) oriented almost perpendicular to the longitudinal axis (Figure 4.7d).

4.3.6 The influence of wind on sediment transport

To understand the influence of wind on sediment transport, the total, river, and bed sediment transport fluxes are analyzed across the central mangrove forest (Figure 4.8). A detailed description of the influence of wind on sediment transport fluxes in the case of a single river scenario can be found in Chapter 3.

Along the central mangrove forest, the presence of $5\,\mathrm{m.s^{-1}}$ wind velocities had varying effects. In particular, in the regions closer to the river mouth, while the directions of sediment transport remained, modest changes in magnitudes were observed. The impact of wind on the smaller western river plume was larger in comparison to that of the large angled river plume (Figure 4.8a-c). Closer to the river mouth of the smaller western river ($0 \lesssim x \lesssim 500\,\mathrm{m}$), southerly winds (270°) resulted in the largest sediment flux, with the magni-

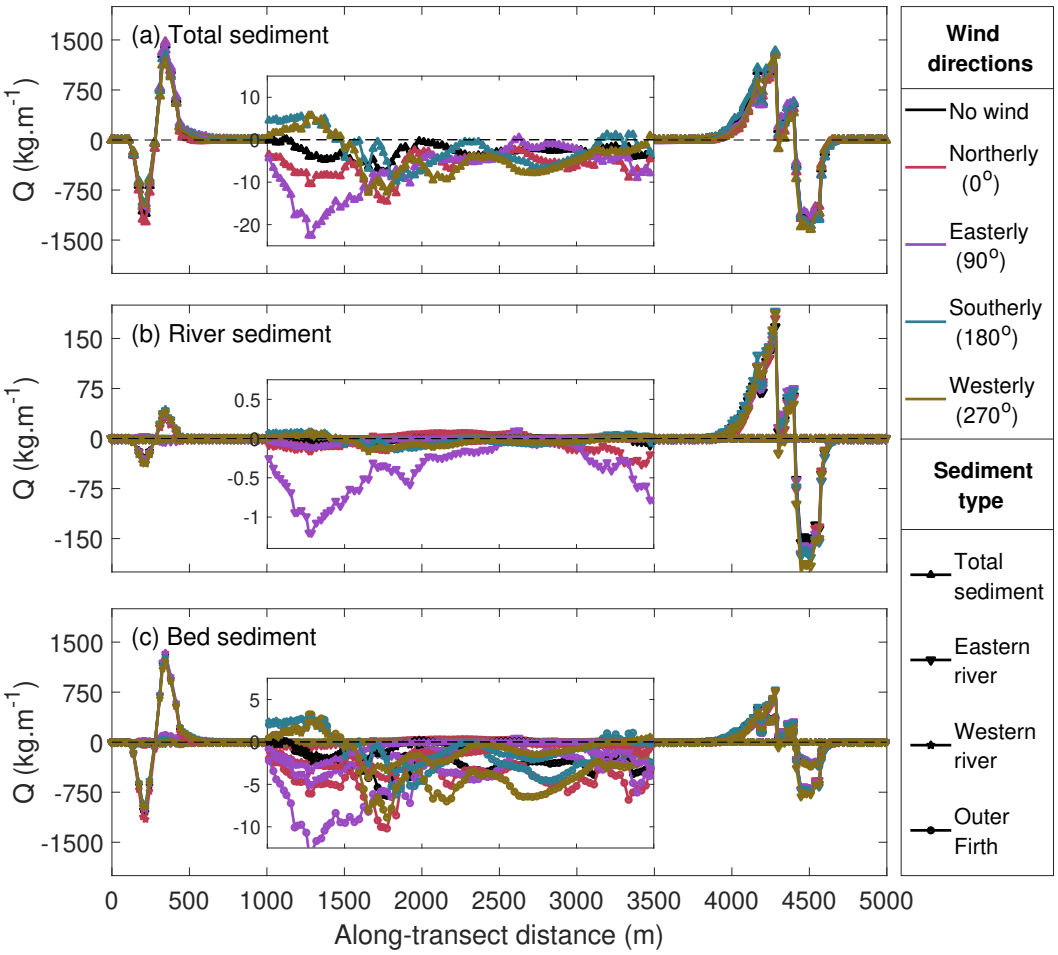

Figure 4.8: Tidally integrated across-transect fluxes for simulations involving winds (Runs 16-19, Table 4.1) along the central mangrove forest. Panels (a) total sediment flux, (b) riverine sediment flux, and (c) bed-sourced sediments. Triangles, circles, and stars represent sediment associated with eastern river, from outer Firth, and the western river, respectively. Along-transect distance of zero corresponds to river mouth of the western river. In our evaluations, positive and negative fluxes indicate sediment transport out of the forest and into the forest region, respectively. Insets show the close-up of the modeled fluxes along the central mangrove forest for distances of $1000\,\mathrm{m} \leq x \leq 3500\,\mathrm{m}$. Note different y-axis scale in panel (b).

tude of the total sediment flux greater by nearly $\sim 16\%$ compared to the no wind scenario. On the other hand, a dominant easterly wind direction (90°) wind produced the largest fluxes.

A significant effect of wind direction on total sediment transport was noted in the region between the river plumes along the central forest (Figure 4.8a,

inset). In particular, in the region $1000\,\mathrm{m} \lesssim x \lesssim 1500\,\mathrm{m}$, while the easterly and northerly winds enhanced sediment transport into the forest similar relative to the no-wind scenario, on the contrary, southerly and westerly winds resulted in sediment transport out of the forest (Figure 4.8c, inset). The magnitude of sediment fluxes in the case of easterly winds was found to be the highest, with an increase in sediment flux by nearly $\sim 80\%$ compared to the no-wind scenario. In the region defined by $x \gtrsim 3800\,\mathrm{m}$, closer to the eastern river mouth (Figure 4.8a), owing to higher riverine momentum, wind driven sediment transport was negligible.

In the presence of $5\,\mathrm{m.s^{-1}}$ wind velocities, the total sediment transport fluxes closer to western and eastern river mouths were directed into the forest along the western and eastern mangrove forests, irrespective of the wind direction (Figure 4.9a-f). Total sediment fluxes along the western (Figure 4.9a) and eastern mangrove forests (Figure 4.9b) were largest in the case of easterly (90°, magnitudes larger by nearly $\sim 40\%$ in comparison to the no-wind scenario) and southerly (180°, magnitudes larger by nearly $\sim 65\%$ in comparison to the no-wind scenario) wind directions, respectively. While the bed sediment contributions dominated total sediment transport along both the western and eastern mangrove forests, the sediment types varied. In particular, along the western mangrove forest, while sediment transport was primarily dominated by bed sediment carried by the western river (nearly $\sim 80\%$ of total sediment). On the other hand, bed sediment carried by the eastern river (nearly $\sim 40\%$ of total sediment) and from the Firth ($\sim 60\%$ of total sediment) were the dominant sediment contributors along the eastern forest, with the highest magnitudes during southerly winds (270°, Figure 4.9b, d, and f). Farther along the eastern mangrove forest ($x \gtrsim 400\,\mathrm{m}$), total sediment fluxes were directed out of the forest for all the wind directions except for northerly, where instead, sediment fluxes were directed into the forest.

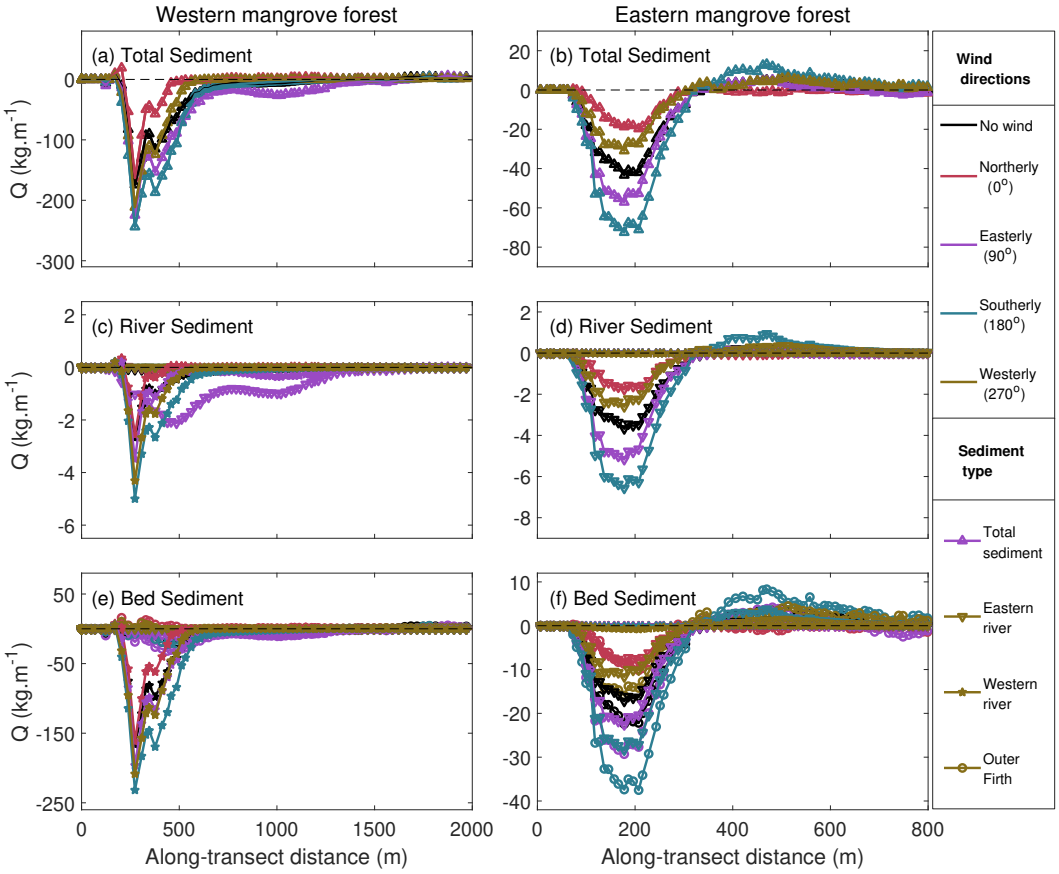

Figure 4.9: Tidally integrated across-transect fluxes for simulations involving winds (Runs 16-19) along the western and eastern mangrove forest. Panels (a) and (b) are total sediment fluxes, (c) and (d) are fluxes of riverine sediments, and (e) and (f) show bed-sourced sediments. Triangles, circles, and stars represent sediment associated with the eastern river, Firth, and western river, respectively. The along-transect distance of zero for the western and eastern transects correspond to river mouth of the western river and eastern river, respectively. In our evaluations, positive and negative fluxes indicate sediment transport out of the forest and into the forest region, respectively.

4.4 Discussion

We investigated how the interactions of two buoyant river plumes in a mangrove environment affected sediment transport and deposition into adjacent mangrove forests. Using numerical experiments conducted over an idealized domain, we address the impact varying riverine flows have on a nearby mangrove forested region by quantifying sediment fluxes into the edge of the forest.

Model simulations with a single river flow showed the formation of a typical radially shaped bulge around the river mouth with a slight deflection towards the right side of the model domain during peak ebb (also seen in Chant et al. 2008; Horner-Devine 2009). During peak flood, the presence of oncoming tidal currents thins the plume expansion along with an acquired westward velocity due to Coriolis (also noted in Kourafalou et al. 1996), establishing a strong alongshore jet along the western mangrove forest (Figure 4.2c). The presence of an adjacent river plume altered the spreading patterns of both plumes. In particular, during low flow events, one river plume's expansion impeded the expansion of the other. This result is similar to Gong et al. (2019) who using numerical studies in the Pearl River Estuary, found that the presence of secondary river plumes in the vicinity of a primary river plume can significantly impact the transport dynamics in the region. They attributed this impact on transport to the barotropic component, which helps limit the spatial extent of the river plume, and the baroclinic component, which aids in decreasing the plume stratification. Furthermore, the plumes coalesced, forming a single plume entity that flowed along the central forest (Figure 4.3). The evidence of river plume coalescence closer to the river mouths in the vicinity has been previously reported in multiple remote sensing studies such as Mertes and Warrick (2001).

For the low flow scenarios, the river-associated sediment fluxes were the largest closer to the river mouths. In the region between the rivers (midway along the forest), bed sediment from the Firth was the major contributor to the sediment transport. In the central forest between the two rivers, sediment fluxes were primarily directed into the forest. The magnitudes of fluxes were highest for eastern river-associated sediment, followed by the western river-associated sediment and, bed sediment from the Firth of Thames outer bay. This variable deposition pattern is consistent with the satellite imagery of the Firth of Thames field site (Figure 1.3). In our study, as the flows

through a river were kept constant and varied through the other, the corresponding spreading patterns altered the sediment fluxes, particularly in the central forested region between the two rivers. As the flow through one river increased, fluxes associated with the second river decreased, and vice versa. This result is similar to that presented by Mendes et al. (2016), who using numerical studies, studied the interactions of the Douro and Minho river plumes in the Western Iberian Peninsula and noted that the spreading of a large river plume adjacent to a smaller plume suppresses the offshore spreading of the small river plumes.

The plume patterns and the corresponding dominant contributors to the total sediment transport changed due to the presence of Coriolis (Southern Hemisphere). For example, the induced turning and rotation of the river plumes due to Coriolis aided the transport into the western mangrove forest; however, the river plumes deflected away from the eastern mangrove forest, and the transport flux magnitudes were reduced. This effect of Coriolis on river plume transport has been recorded in multiple studies (e.g. Wells, 2009). In our study, the rivers in their vicinity dominated sediment deposition along the mangrove forests that lined the shoreline. In particular, for low and medium flow rates through each river, sediment transport was primarily dominated by the angled eastern river along the eastern forest and the western river along the western forest. For each river, as the plumes debouched into the central domain, the lateral expansion within the near-field region of the plumes helped push sediments brought in by the river into the nearby forest region, while the drag associated with vegetation helped deposit this sediment. This sediment deposition close to the river mouth has been seen previously in many studies (e.g. Van Maren, 2007; Fagherazzi et al., 2015; Vundavilli et al., 2022).

In this study, along the eastern and western forested regions, variation of flows through either river altered the sediment transport fluxes. In particular,

the plume waters from the larger eastern river dominated sediment transport through the central and eastern mangrove forests when the discharge through the western river remained equal to or below its medium flow rate. This result agrees with previous studies (e.g. Gong et al., 2019; Mendes et al., 2016), who noted that the presence of a large river plume suppresses the offshore spreading of small river plumes in the vicinity while enhancing the downstream transport of the former. However, in the case of large flow discharge through the western river, owing to the larger plume extent, sediment from the western river dominated sediment transport across the central, western, and eastern forests. In the regions away from the river mouth, sediment transport along the western and eastern forest was dominated by the bed sediment from the coastal bay and was directed out of the forest for all the model runs employed. This sediment outflow along the edge of the mangrove forest can be attributed to the ebb-tidal asymmetry (previously seen in many studies; e.g., Bryan et al. 2017).

The effect of $5\,\mathrm{m.s^{-1}}$ winds modified the coalesced river plume mass in our model simulations (also seen in Warrick and Farnsworth 2017). In our study, sediment transport fluxes were largest through the central and western mangrove forests in the case of easterly winds. The easterly winds, in combination with the Coriolis, helped transport a significant part of sediment from the eastern river into the central forested region. These plume deflections and the corresponding enhanced transport in the presence of winds are consistent with various river plume studies (Masse and Murthy, 1992). In the case of eastern mangrove forests, total sediment flux magnitudes were largest in the case of southerly winds. This increase in the total sediment flux can be attributed to the suppression of the plume bulge, which helped push the plume bulge into the eastern mangrove forest. This reversal of plume transport due to winds has been previously reported in many studies (e.g. Schiller et al., 2011).

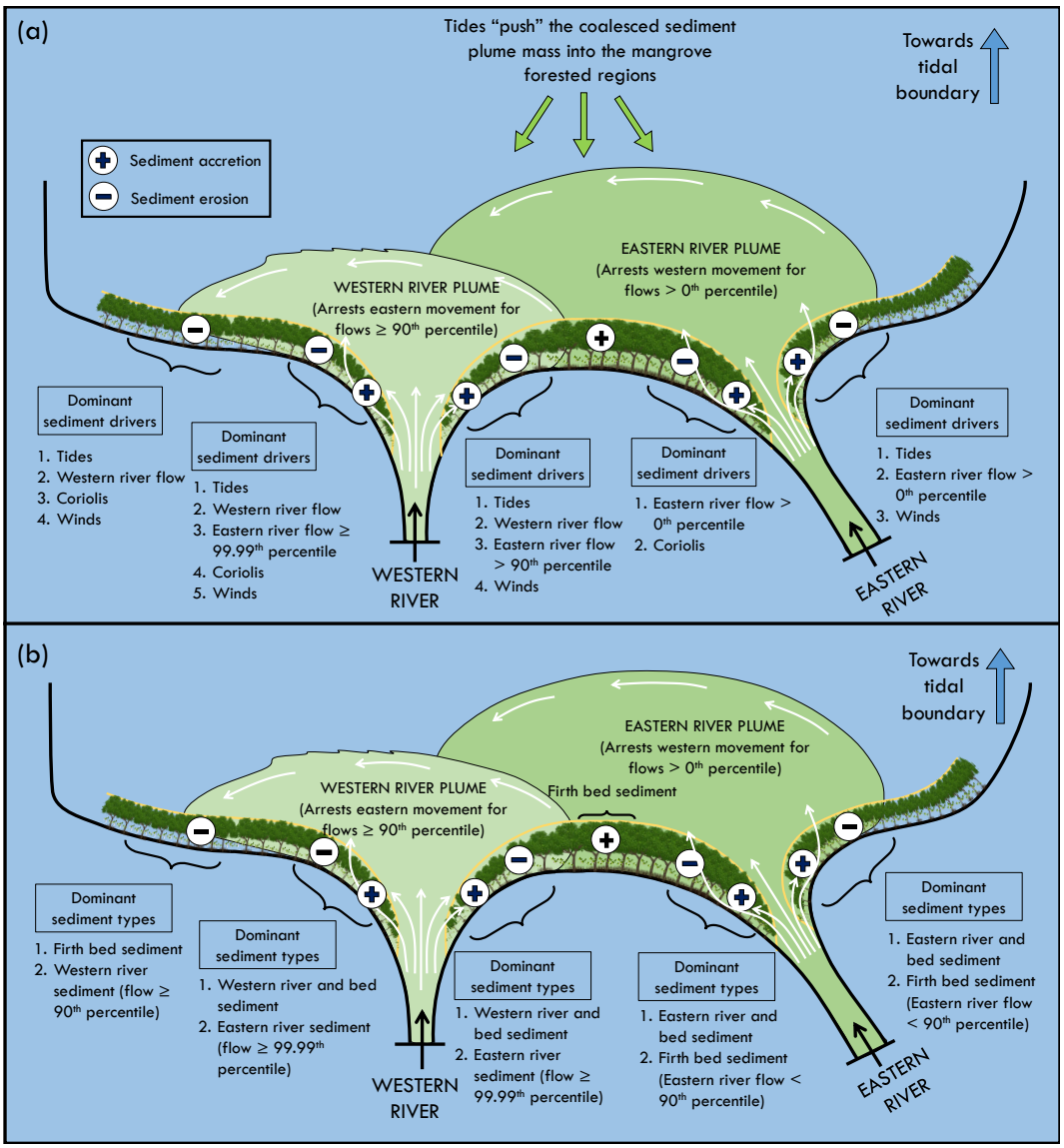

Figure 4.10: Schematic representation of the dominant sediment dynamics within the Firth of Thames (FoT). Panel (a) shows the plume interactions and Panel (b) shows the dominant contributors towards the total sediment transport fluxes within the FoT system.

4.5 Conclusions

This study examines the influence of two river plumes on sediment dynamics and the morphological evolution of a mangrove system. A three-dimensional Delft3D morphological model based on the Firth of Thames mangrove forest is used to conduct a series of numerical experiments. The results obtained in this study are summarized in Figure 4.10 have yielded the following insights into

sediment transport patterns owing to interactions between two river plumes:

1. The sediment plumes formed from each river are well developed and coalesced to a varying degree for each model run. Due to intense mixing within the coalesced sediment plume mass, deposition between the river mouths decreased (midway along the central forest).

2. When large flows were forced through either river, sediment from the river was transported into the other river suppressing the downstream transport of the latter plume (Figure 4.10b). The presence of Coriolis (Southern-hemisphere) helped transport a significant amount of sediment into the western side of the model domain. Along the central mangrove forest, sediment from the large river (located to the east, Figure 4.10a) was deflected due to Coriolis resulting in higher sediment fluxes.

3. Coalescence of the plumes increased with northerly and easterly winds leading to higher transport fluxes through the central and the western mangrove forests (Figure 4.10a). Alternatively, as southerly winds push the mid-field and far-field regions of the eastern river into the eastern mangrove forest, sediment transport fluxes were largest, compared to other wind directions. As the rivers carried sufficient momentum to overcome wind speeds or sediment was advected away from the forests, the directions of sediment transport in the near-field region of the rivers remained unaltered (Figure 4.10b).

While our study captures many dominant sediment transport processes within riverine and coastal mangrove environments, other critical processes such as waves are not included in the present study. Nevertheless, the numerical experiments revealed insights into sediment transport and depositional patterns within mangroves forests upon interactions with coalescing river plumes, which has received insufficient attention. The results in this study demonstrate that even modest changes to the forcing parameters change the overall

sediment deposition characteristics. The deposition patterns observed in our study suggest that over longer-timescales, an on-shore directed supply of sediment from rivers exists, which can help in seaward extension of mangroves (Woodroffe et al., 2016). Furthermore, as Coriolis, flow, and the river mouth geometry aid in transporting large amounts of the eastern river sediment, mangrove progradation may be closer to the eastern river, which may induce sediment feedback and changes to circulation in the lower Firth of Thames.

Chapter 5

General conclusions

5.1 Review of major concepts

This thesis addresses the interactions of river plumes with mangroves and the consequences for the resultant hydro-morphodynamics and sediment transport patterns. Idealized numerical simulations are used to address the research questions stated in Section 1.4 and the main conclusions are given below. Additionally, a visual summary of the findings is presented in Figure 5.1.

1. How does the presence of vegetation alter the river plume dynamics and associated sediment transport patterns within various regions of the mangrove forest? Specifically, what are the principal momentum contributors that influence the transport of sediment within the forest, fringe, and the tidal flat of a mangrove forest?

Chapter 2 of this thesis explored the sediment transport patterns resultant from the interaction of buoyant river plumes with vegetation using idealized three-dimensional numerical experiments. The model of a single river debouching into a mangrove-lined coastal bay was designed as an idealized version of the Firth of Thames mangrove forest, located in the North Island of New Zealand. Results from the numerical model showed that vegetative drag influenced sediment patterns as the underlying dynamics were substantially altered

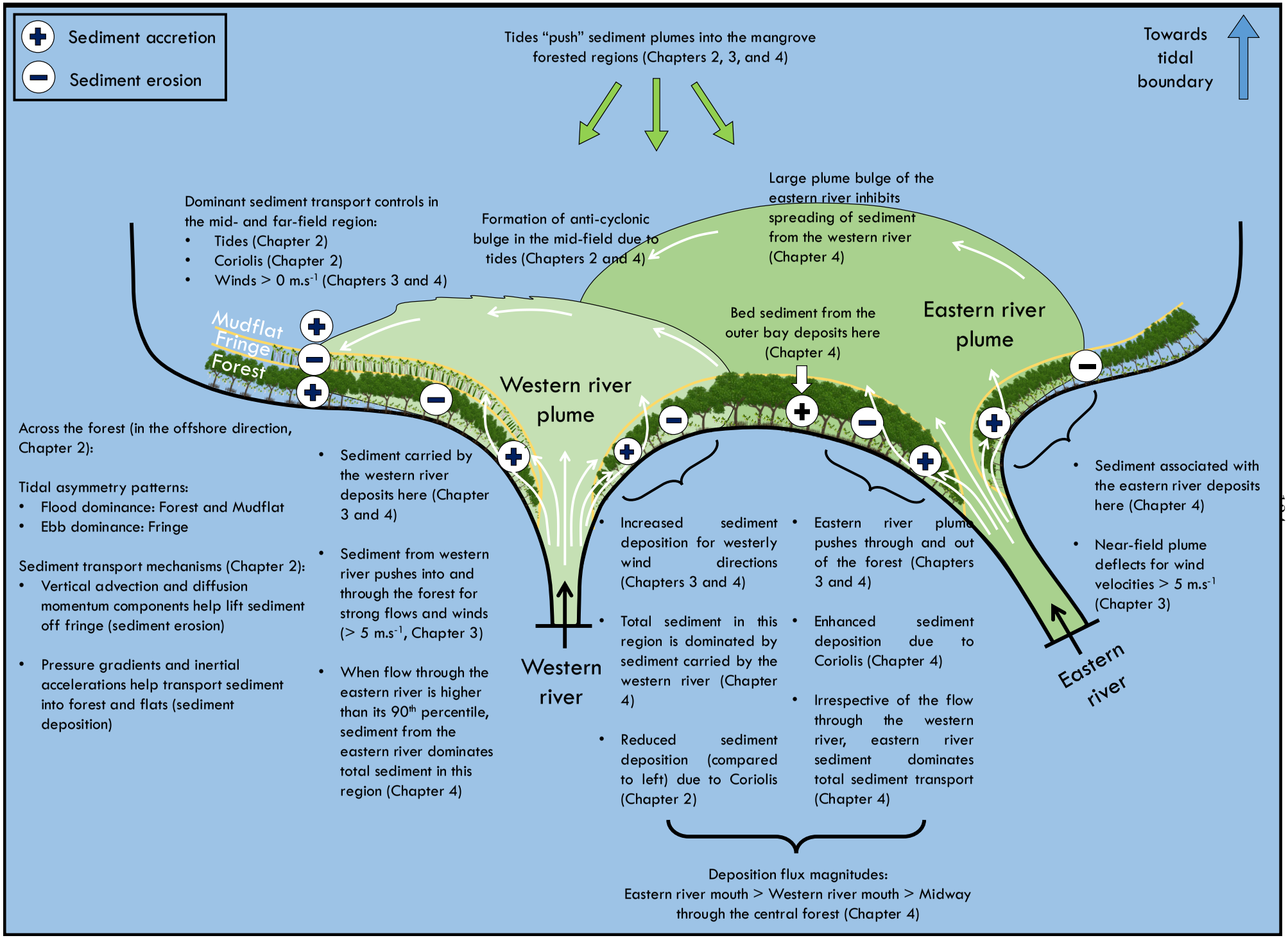

Figure 5.1: Schematic representation of the key findings from this investigation of river plume interactions with mangrove vegetation.

relative to model simulations without vegetation. The analysis of sediment deposition in the model runs with spatially varying roughness (vegetated runs) in the along-shore direction showed that while sediment deposition occurred inside the forest and tidal flats, sediment erosion occurred in the fringe region. Alternatively, for the non-vegetated runs, sediment deposition occurred throughout the model domain. Within the vegetated regions, the influence of friction enhanced the slack water tidal asymmetry. In particular, in the shallow forested and the tidal flat regions, slack water tidal asymmetry patterns were found to flood dominant, while the fringe regions were found to be ebb-dominant. The evaluation of momentum balances across various regions of the river plume (near-, mid-, and far-field regions) showed that vegetation altered the underlying dynamics due to vegetative drag. Closer to the river mouth (near-field region), the principal balance between the baroclinic pressure gradient and the enhanced bottom shear stress due to vegetation controlled the sediment transport into the forest. Evaluations of momentum balances in the far-field region of the river plume showed that the force balance between the barotropic pressure gradient and inertial acceleration remained on the surface layer. In the bottom layer, the bottom shear stress in the across and alongshore momentum balances indicated that vegetative drag was pivotal in inhibiting sediment movement in the offshore direction. Coriolis acceleration momentum components in the mid- and far-field regions deflected the river plume to the left (Southern Hemisphere), which helped explain the increased sediment deposition in the western side of the model domain relative to the eastern side. The across and alongshore force balances in the fringe region of the mangroves exhibited more complexities than the forest and flat regions. The presence of vertical diffusion and advection components in the momentum balances in the fringe indicated a mechanism through which the bed-sourced sediment was uprooted into the water column during the flood stage of the tidal cycle and distributed into the forest and flat region during the ebb.

2. How does the change in freshwater discharge and the presence of winds influence the sediment transport patterns?

Dynamics within a river plume system are altered under varying river flows (e.g. Horner-Devine et al., 2015) and winds (e.g. Fong and Geyer, 2001), which can modify the overall sediment transport patterns. Using the idealized model employed in Chapter 2, Chapter 3 of this thesis focused on the influences of river discharges and wind velocities on sediment transport patterns and the relative contributions of the river- and bed-sourced sediment along the edge of the western mangrove forest. The results from the idealized numerical experiments revealed that riverine sediment fluxes into the forest depended on the individual regions of the river plumes and the distance over which the zones extended. Furthermore, the numerical experiments revealed two zones of sediment transport directional trends: (i) a near-field depositional zone close to the river mouth and (ii) a far-field sediment erosion zone. In the depositional zone, as the plume entered the coastal waters, irrespective of the river discharge employed, total sediment was directed into the forest, indicating an accretionary environment. The results further revealed that riverine sediment remained the major contributor to bed-sourced sediment in the depositional zone towards the total sediment transport. On the other hand, in the far-field sediment erosion zone, tidal effects and winds dominated sediment transport with little river influence. In particular, the ebb-dominance of the region assisted in transporting sediment out of the region. The investigation of sediment transport patterns under winds revealed that weak winds only modified the total sediment transport fluxes in the mid- and far-field region, as the momentum carried by the river discharge was sufficient to overcome the wind stress. However, the presence of strong winds was able to alter the sediment transport patterns within the entire plume structure. The total sediment transport patterns were most prominent, and more sediment was deposited into the forest in the case of easterly winds; alternatively, as the plume was deflected away from the forest in the case of westerly winds,

total sediment transport input into the forest was smallest. Compared to the vegetated and non-vegetated runs (represented with a spatially uniform roughness), riverine sediment fluxes yielded similar directional trends; however, the magnitudes increased in the non-vegetated case due to lack of vegetative drag. The magnitude of bed-sourced sediment fluxes was larger in the case of vegetated runs than the non-vegetated runs due to enhanced bed-shear stresses from the mangrove vegetation. The mass loads into the forest increased with an increase in river discharge for small to medium discharges employed in this study. However, these mass loads were similar to the large riverine discharges, as the sediment plume was pushed through and out of the forest front onto the adjacent mudflat due to enhanced momentum carried by the river.

This work indicates that irrespective of the river flows, vegetative drag due to mangrove vegetation helps sediment deposition closer to the river mouth, which can help explain the mangrove progradation observed through the satellite imagery of the Firth of Thames (in contrast to the decline seen in the global trends; Giri et al. 2011). Additionally, this study reveals the effect of wind of both weak and strong winds on riverine sediment transport patterns, in that strong winds, are capable of reversing sediment transport directions within a mangrove forest and consequently changing the overall depositional patterns in the vegetative environments.

3. How does the presence and coalescence of multiple nearby river plumes alter the sediment transport and deposition patterns within a coastal mangrove environment?

Warrick and Farnsworth (2017) previously proposed that for coastal regions with multiple rivers in close proximity, the spreading patterns and the fate of freshwater transport from the rivers are influenced by plume-to-plume interactions. Chapter 4 investigated the interaction of two coalescing buoyant river plumes and their effects on sediment transport and deposition patterns

in a mangrove environment. The idealized model used in Chapters 2 and 3 was modified to include two mangrove-lined rivers, and sediment transport and deposition patterns were assessed across the central (located between the two rivers), western, and eastern mangrove forests. In this investigation, the river plumes for all the numerical experiments coalesced into a single river plume mass deflected to the left due to Coriolis (Southern Hemisphere) and flowed along the edge of the central mangrove forest. As a result, sediment dynamics across each of the mangrove forests varied. In particular, the eastern river dominated the sediment dynamics along a significant portion of the central and the eastern mangrove forests. On the other hand, the western river plume dictated sediment dynamics along a small portion of the central mangrove forest and a significant part of the western mangrove forest. Additionally, along the central mangrove forest, a variable deposition pattern was noted, in that the total sediment fluxes were the largest closer to the river mouths, with smaller amounts of sediment deposited midway along the central forest, consistent with the satellite imagery of the Firth of Thames. When the flow through either river was increased, sediment fluxes into the forest associated with the nearby river decreased as the expansion of the plume bulge of the nearby river was suppressed. However, owing to the large eastern river, changes in total sediment input were relatively modest in the case of eastern mangrove forest in comparison to the central and western mangrove forests. The presence of winds enhanced the plume coalescence, thereby increasing the total sediment transport into and deposition within the mangrove forests. As the easterly winds deflected the plumes to the left, sediment deposition in the eastern and central mangrove forests was enhanced. On the other hand, in the case of southerly winds, the plume of the large eastern river was pushed into the eastern mangrove forest, resulting in increased sediment deposition in the eastern mangrove forest.

This work indicates that sediment deposition characteristics within man-

grove environments are susceptible to modest changes to hydrodynamic and meteorological changes. The presence of an additional river in the proximity of a mangrove-lined river debouching into the coastal bay can alter the resultant spreading and sediment deposition patterns. Furthermore, results suggest that the presence of winds influences sediment deposition near the river mouths and the outer bay as the dynamics within the mid- and far-field regions of the plumes are altered. Lastly, our results suggest that over longer timescales, the sediment supply from rivers can be transported into the forests, which can help explain the seaward extension of mangroves as observed in the Firth of Thames.

5.2 Recommendations for future work

The research presented in this thesis demonstrates that the presence of mangrove vegetation alters sediment transport patterns in coastal regions by providing additional flow resistance. The distribution of mangroves around the tropical and sub-tropical environments (expected to face the worst impacts of climate change) makes mangrove ecosystems highly susceptible to climate change (Gilman et al., 2008), especially sea-level rise changes in sediment and water supply. Based on the findings of this thesis, suggestions for future research focus on (a) sea level rise and (b) coastal mangrove defense and mangrove conservation.

Previous studies on the response of mangrove environments at sea level have found that sediment trapping mechanisms of mangroves aid in natural resilience (e.g. McKee, 2011). However, the potential impacts of changes in sea-level rise on mangrove environments are relatively less understood. Numerical simulations presented in Chapters 3 and 4 have shown that sediment accumulation due to sediment trapping can lead to the seaward extension of mangroves. This sediment deposition within mangroves assists these ecosys-

tems to overcome deeper inundation that arises due to the sea-level rise (SLR). For example, previous studies conducted to understand the response of mangroves to sea-level rise have found that the resilience of mangroves to sea-level rise needs to incorporate plant productivity and elevation changes (Woodroffe et al., 2016). While simpler models (Krauss et al., 2014) have previously investigated the response of salt marshes to SLR, there remains an insufficient understanding of the ecological dynamics and the morphodynamic behavior within different types of mangrove environments, especially with regard to subsurface processes. Hence, further research focused on coupling the ecological processes to the physical and sediment transport processes, would aid in a realistic prediction of mangrove response to SLR.

Various previous studies have highlighted the importance of mangroves and their role in mitigating storm-induced coastal hazards (e.g. Temmerman et al., 2013). Conceptually, mangrove efficiency depends on their ability to reduce storm surges and associated flood and erosion risks and recover from storm damage (Temmerman et al., 2023). In the recent past, nature-based solutions for mitigation of impacts of storms have been proposed (Morris et al., 2018) as a cost-effective strategy. However, mangrove functioning and persistence are determined by intrinsically site-specific processes, dynamics, and thresholds that must be defined and monitored in flood risk reduction projects (Gijsman et al., 2021). Therefore, additional investigations across a wider parameter space would promote a more complete understanding of the underlying dynamics, which would help to predict the efficacy of site-specific nature-based solutions, and the response of mangrove ecosystems to natural hazards such as storm surges.

The idealized numerical models presented in this thesis addressed the sediment transport and deposition patterns of river plume interactions with mangrove environments. However, as with all the numerical modeling studies, a

few limitations can be improved to enhance our understanding of sediment dynamics within mangrove environments.

The primary shoreward transport mechanism within the Firth of Thames mangrove system is sheet flow through the vegetation (Montgomery et al., 2018). Hence, the dynamics presented in this thesis do not apply to the broader array of coastal vegetation (e.g., seagrass), wherein creek flow dynamics dominate. Furthermore, past work suggests that vegetation changes the overall cross-shore bottom profiles within a mangrove system over longer time scales, forming concave and convex profiles (Bryan et al., 2017). In our study, as the model simulations were run for short-time scales, the sediment deposition was not large enough to substantially alter the original profiles. Numerical modeling experiments conducted over longer time-scales can help improve the prediction of cross-shore changes within the mangrove environments.

In this thesis, vegetation was represented by a spatially varying Chézy coefficient; however, variations in stem density and height are significant in natural mangrove systems. Furthermore, within mangroves, the pneumatophore density and height within the existing systems have been found to considerably alter the water levels and velocities (Horstman et al., 2018). As a result, the incorporation of vegetation characteristics may increase model accuracy. Additionally, critical processes such as waves and flocculation, which control the sediment settling velocities and movement of fine sediments in aquatic environments, have not been captured in this study but nonetheless have been shown to vary substantially along tidally influenced rivers (MacDonald and Mullarney, 2015). Thus, incorporating parameterizations of these processes into numerical and theoretical models of the system may improve our predictions for the ecogeomorphic evolution of coastal regions.

5.3 Summary

This thesis explored the dynamics of freshwater and sediment plumes interacting with vegetation. The presence of mangroves lining a river and intertidal regions strongly altered the sediment transport and deposition patterns as the river debouched into the coastal ocean. Moreover, these patterns were further modulated by variations in discharge, winds, or coalescence with a second nearby river. Furthermore, the idealized numerical experiments show that the interplay between the tides, riverine flows, and winds alter the biophysical interactions in mangrove ecosystems. The results presented in this thesis have elucidated the underlying dynamics of mangrove-lined rivers and coastal zones, and in particular, the fate of sediments. These insights will help to predict the future geomorphic evolution of these threatened coastal regions under varying climatic conditions.

Appendices

Chapter A

Non-vegetated case: Momentum balances

This appendix includes the momentum balances for the model simulations with spatially uniform roughness (non-vegetated runs) previously described in Chapter 2. Description of regions with respect to the along-transect position x for each of the transect 1 and transect 2 are summarized in Table A.1.

A.1 Dominant dynamics - Transect 1

Surface layer During the peak ebb tide, inertial acceleration (term A) and the Coriolis acceleration (term E) balanced the lateral momentum exchange (term C) and the barotropic pressure gradient (term F1) on the surface layer for this transect (Figure A.1a). Farther out on the regions corresponding to $x > 0\,\mathrm{m}$, streamwise momentum exchange ($\sim 0.5\mathrm{x}10^{-5}\,\mathrm{m.s}^{-2}$), Coriolis acceleration ($\sim 1\mathrm{x}10^{-5}\,\mathrm{m.s}^{-2}$) and inertial acceleration ($\sim 0.5\mathrm{x}10^{-5}\,\mathrm{m.s}^{-2}$) balanced the barotropic pressure gradient ($\sim$-$2\mathrm{x}10^{-5}\,\mathrm{m.s}^{-2}$). In the along-transect direction (from $x \approx$ -1000 m to $x \approx 1000\,\mathrm{m}$), the barotropic pressure gradient term is balanced by the inertial acceleration throughout transect 1 during the peak flood (Figure A.1c). There was however a small contribution of Coriolis acceleration and the vertical diffusion of momentum in the region from ($x \approx$ -500 m to $x \approx$ -400 m). In the across-transect direction, dominant

Table A.1: Description of coordinates and different regions along transect 1 and transect 2 in the case of non-vegetated simulations.

Transect number	Along-transect position along the transect (x) in m (positive eastward)	Region of plume	Model observation points in region as shown in Figure 2.6a
Transect 1	-1250 $< x <$ -100	Beginning of the transect	OP 1-3
	-100 $< x <$ 0	Center of the transect	OP 4-5
	0 $< x <$ 1000	Deep end of the transect	OP 6-7
Transect 2	-250 $< x <$ -150	Beginning of the transect	OP 1-3
	-150 $< x <$ 0	Center of the transect	OP 4-5
	0 $< x <$ 100	Deep end of the transect	OP 6-7

balance during both peak ebb and flood stages of the tidal cycles remained between the barotropic pressure gradient and the inertial acceleration throughout this transect (Figure A.2a and c).

Bottom layer During the peak ebb tide, bed shear stress (term I1) and lateral momentum exchange (term C) were balanced by the contributions from the inertial acceleration (term A), baroclinic pressure gradient (term F2), acceleration due to viscosity (term G, Figure A.1b) throughout transect 2 in the bottom layer. In the along-transect direction throughout transect 2 in the bottom layer, bed shear stress (term I1, $\sim$10x10^{-5} m.s^{-2}) balanced the inertial acceleration (term A, $\sim$-5x10^{-5} m.s^{-2}) and the barotropic pressure gradient (term F1, $\sim$-5x10^{-5} m.s^{-2}) during the peak flood (Figure A.1d).

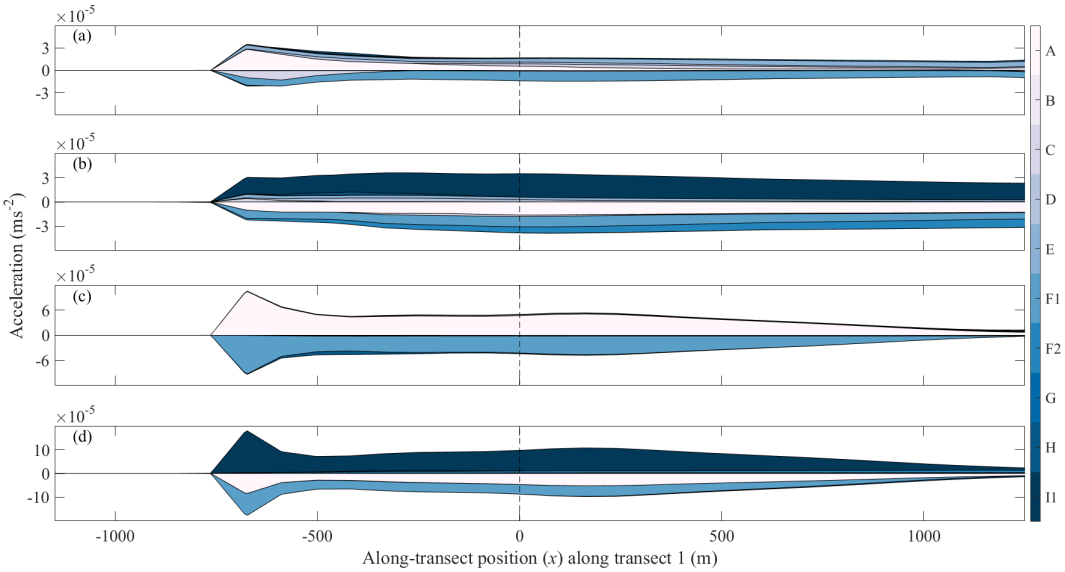

Figure A.1: Along-transect momentum balance for transect 1 observed with uniform roughness in the domain. Peak ebb of tidal cycle (a) surface layer and (b) bottom layer. Peak flood of tidal cycle (c) surface layer, and (d) bottom layer. The cumulative sum of positive and negative momentum components (colors show the individual momentum components represented in Table A.1). $x = 0$ indicates the center of this transect which corresponds to the forest fringe transition zone in the vegetated model run.

In the across-transect direction from regions $x \approx$ -1000 m to $x \approx$ -500 m, during both the peak ebb and flood tides (Figure A.2b and d), bed shear stress ($\sim$ 1.5x10^{-4} m.s^{-2}) and the inertial acceleration ($\sim$ 0.5x10^{-4} m.s^{-2}) balanced the barotropic pressure gradient ($\sim$ -1.9x10^{-4} m.s^{-2}) with a small contribution from vertical diffusion of momentum ($\sim$ -0.1x10^{-4} m.s^{-2}).

A.2 Dominant dynamics - Transect 2

Surface layer In the along-transect direction, at the beginning of this transect (from $x \approx$ -250 m to $x \approx$ -50 m), the barotropic pressure gradient balanced the inertial acceleration, lateral momentum exchange, the Coriolis accelerations during the peak ebb tide (Figure A.3a). At the center of the plume (from $x \approx$ -50 m to $x \approx$ +100 m), the Coriolis acceleration ($\sim$ 0.5x10^{-4} m.s^{-2})

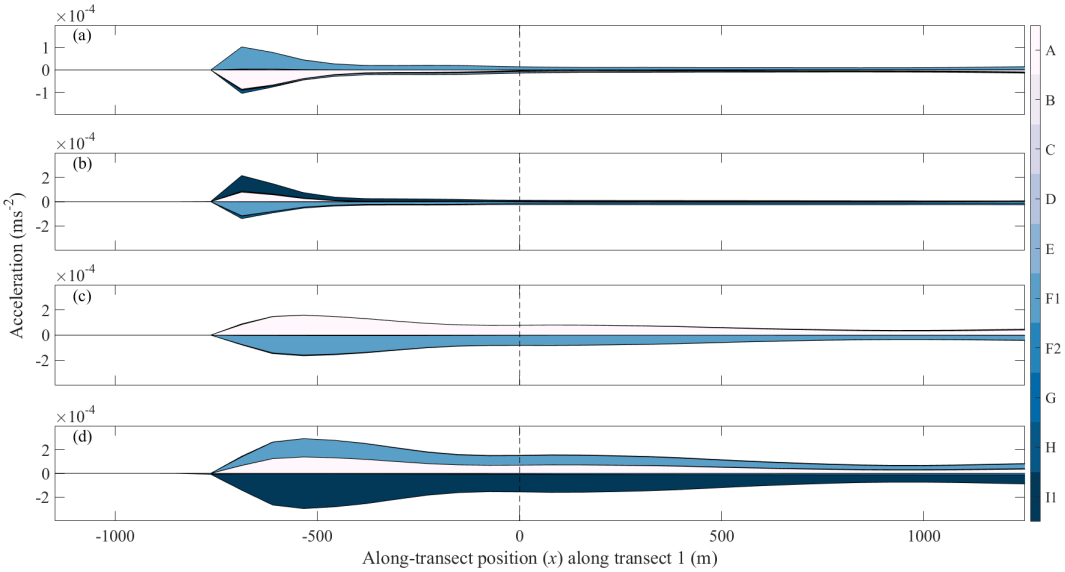

Figure A.2: Across-transect momentum balance for transect 1 observed with uniform roughness in the domain. Peak ebb of tidal cycle (a) surface layer and (b) bottom layer. Peak flood of tidal cycle (c) surface layer, and (d) bottom layer. The cumulative sum of positive and negative momentum components (colors show the individual momentum components represented in Table A.1). $x = 0$ indicates the center of this transect which corresponds to the forest fringe transition zone in the vegetated model run.

was balanced by the inertial acceleration ($\sim$-0.25x10^{-4} m.s^{-2}), the barotropic pressure gradient ($\sim$-0.10x10^{-4} m.s^{-2}), and streamwise momentum exchange($\sim$-0.15x10^{-4} m.s^{-2}) in the surface layer. A dominant balance between the inertial and the barotropic pressure gradient was observed during the peak flood tide throughout the transect 2 (from $x \approx$ -100 m to $x \approx +100$ m) with modest contributions from streamwise momentum exchange and vertical advection of momentum near center of the plume (Figure A.3c).

During both the flood and ebb stages of the tidal cycle, the dominant across-transect momentum components were the baroclinic pressure gradient, lateral momentum exchange, and vertical advection in the $+y$ direction and the inertial acceleration, streamwise momentum exchange, and the barotropic pressure gradient in the $-y$ direction throughout the transect 2 (Figure A.4a and c).

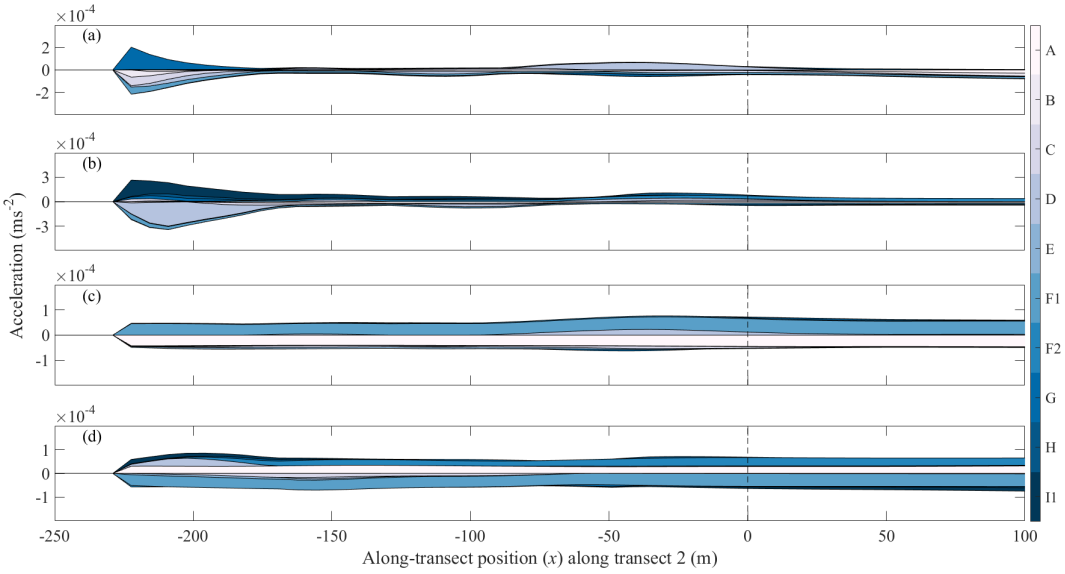

Figure A.3: Along-transect momentum balance for transect 2 observed with uniform roughness in the domain. Peak ebb of tidal cycle (a) surface layer and (b) bottom layer. Peak flood of tidal cycle (c) surface layer, and (d) bottom layer. The cumulative sum of positive and negative momentum components (colors show the individual momentum components represented in Table A.1). $x = 0$ indicates the center of this transect which corresponds to the forest fringe transition zone in the vegetated model run.

Bottom layer The dominant balances in the along-transect direction during both the peak flood and ebb stages of the tidal cycle remained the same differing only in terms of their respective magnitudes. During the peak ebb tide at the beginning of transect 2 (from $x \approx$ -250 m to $x \approx$ -50 m), bed shear stress ($\sim$2.5x10^{-4} m.s^{-2}), the baroclinic pressure gradient ($\sim$0.25x10^{-4} m.s^{-2}) and vertical diffusion of momentum ($\sim$0.25x10^{-4} m.s^{-2}) was balanced by the barotropic pressure gradient ($\sim$-2.5x10^{-4} m.s^{-2}) and the Coriolis acceleration ($\sim$-0.5x10^{-4} m.s^{-2}, Figure A.3b).

During the peak flood tide at the beginning of transect 2 (from $x \approx$ -250 m to $x \approx$ -50 m), the inertial acceleration, bed shear stress and the Coriolis acceleration balanced the barotropic pressure gradient. Farther away (from $x \approx$ -50 m to $x \approx$ +100 m), baroclinic pressure gradient ($\sim$0.5x10^{-4} m.s^{-2}) and the inertial acceleration ($\sim$0.5x10^{-4} m.s^{-2}) balanced the barotropic pressure

gradient ($\sim$-0.75x10^{-4} m.s^{-2}) and the bed shear stress ($\sim$-0.25x10^{-4} m.s^{-2}, Figure A.3d).

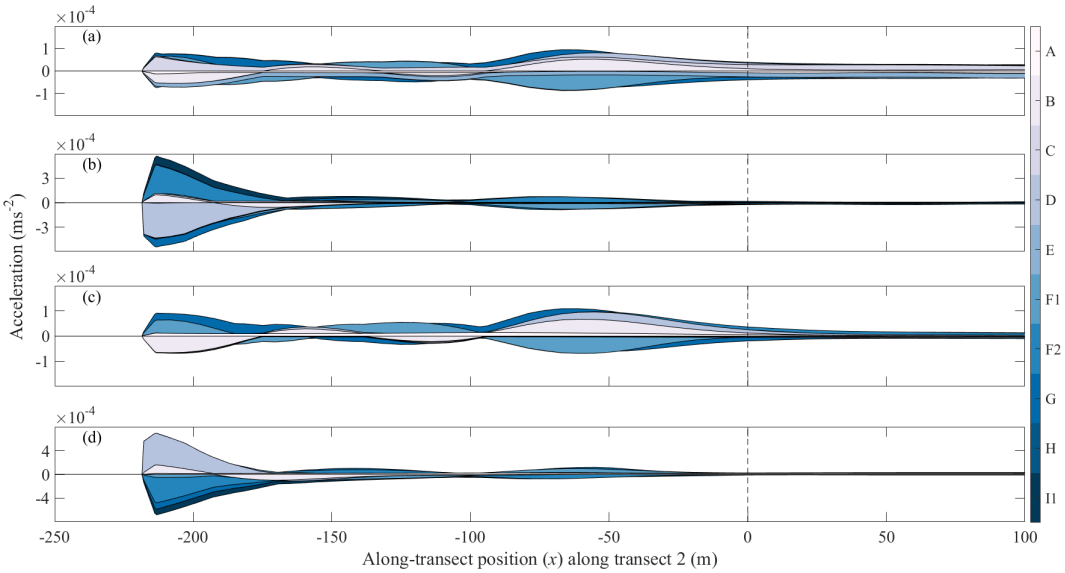

Figure A.4: Across-transect momentum balance for transect 2 observed with uniform roughness in the domain. Peak ebb of tidal cycle (a) surface layer and (b) bottom layer. Peak flood of tidal cycle (c) surface layer, and (d) bottom layer. The cumulative sum of positive and negative momentum components (colors show the individual momentum components represented in Table A.1). $x = 0$ indicates the center of this transect which corresponds to the forest fringe transition zone in the vegetated model run.

During both the peak ebb and the peak flood stages of the tidal cycles at the beginning of transect 2 (from $x \approx$ -250 m to $x \approx$ -50 m), bed shear stress (term I1), the inertial acceleration (term A) and the baroclinic pressure gradient (term F2) balanced the barotropic pressure gradient (term F1) and acceleration due to viscosity (term G, Figure A.4a) in the bottom layer. This trend continued until center of the plume ($x \approx$ -50 m), where the barotropic pressure gradient balanced the baroclinic pressure gradient (Figure A.4a).

Chapter B

Sensitivity analyses

The model results presented in this thesis are based on a single set of morphological parameters. Therefore, a rigorous sensitivity analysis was performed to analyze the effects of the most critical hydro-morphodynamic parameters: the vertical resolution of the model grid, Chézy roughness coefficient, settling velocities, and the initial bed sediment thickness employed.

B.1 Vertical resolution of the model

To investigate whether the model used in Chapter 4 of this thesis can adequately model plume coalescence, numerical model simulations with 10 and 15 σ-layers were conducted and compared with the 5 σ-layers case. In addition, each model was forced with morpho-hydrodynamics conditions as per Run 11 in Table 4.1 presented in Chapter 4.

During the peak ebb stage of the tidal cycle, as both the eastern and western rivers are at their maximum expansion, salinity plumes formed by both rivers are well formed for all the model scenarios undertaken (Figure B.1). Furthermore, the plume coalescence is well captured by all model runs, with modest changes observed as the vertical resolution of the model grid was increased. However, compared to 10 and 15 σ-layers models, the 5 σ-layers

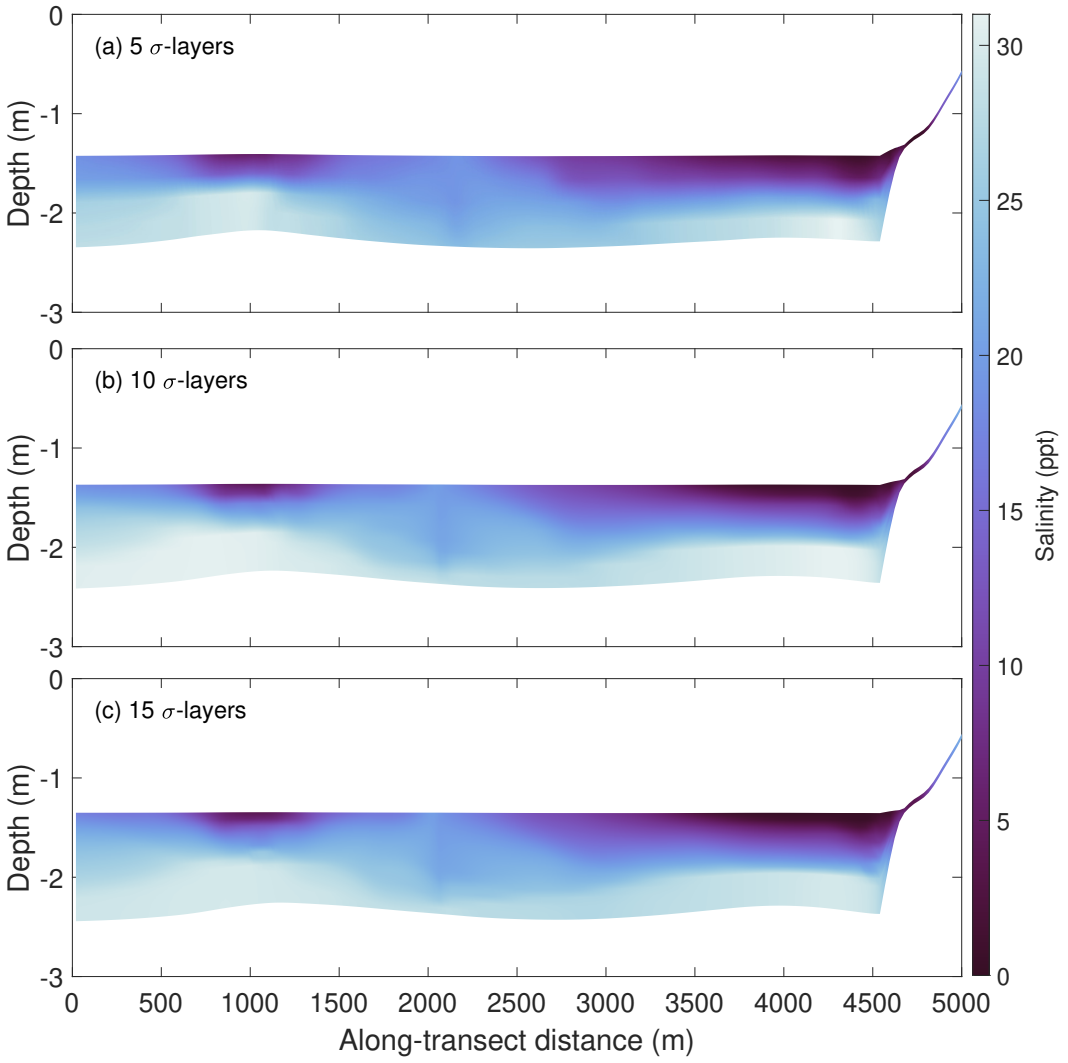

Figure B.1: Comparison of vertical salinity profiles along the central mangrove forest during the peak ebb stage of the tidal cycle with respect to (a) 5 σ-layers, (b) 10 σ-layers, and (c) 15 σ-layers. The along-transect distance of $x = 0\,\mathrm{m}$ corresponds to the river mouth of the western river.

model slightly underpredicts salinity along the central region of the transect (-1000 m $< x <$ 500 m, Figure B.1a).

In the case of our model, compared to the simulation time of the 5 σ-layer model, simulation times were nearly double and quadrupled in the case of 10 σ-layers and 15 σ-layer models. As the results do not change substantially between these vertical resolutions considered, we chose the 5 σ-layer model to investigate the plume coalescence and sediment transport patterns to minimize the computational time of our simulations.

B.2 The influence of Chézy roughness coefficient and settling velocities

Various Chézy roughness coefficients were employed to test the model performance and the influence on sediment transport and deposition patterns. In particular, we employed two additional model simulations with Chézy coefficients of 5 and 10 within the forest to evaluate the influence of Chézy roughness on the predicted sediment thickness. An additional analysis was also conducted to test the influence of sediment settling velocities of $1\,\mathrm{mm.s^{-1}}$, $3\,\mathrm{mm.s^{-1}}$, $5\,\mathrm{mm.s^{-1}}$, and $7\,\mathrm{mm.s^{-1}}$. To test the model sensitivity to Chézy roughness and the settling velocities, predicted sediment thickness was plotted for a transect considered away from the river mouth (Table 2.2). Transect 1 extends from the forest to intertidal mudflats away from the river mouth (Figure 2.2).

With a smaller Chézy coefficient (corresponding to rougher forest) in the forest region, sediment transport along the transect increased substantially, as expected (Rickenmann, 1999). In particular, relative to the model simulations with a Chézy value of 15 in the forest region, deposition in the forest region increased by nearly $\sim 80\%$ and $\sim 30\%$ for model simulations with Chézy values of 5 and 10, respectively (Figure B.2a). This trend continued along the transect, with enhanced erosion and deposition, within the forest fringe and the mudflat regions, respectively. In our model simulations, sediment transport along the transect from forest to mudflats was found to decrease substantially with an increase in sediment settling velocities (Figure B.2b). Within the forest, the most prominent deposition was noted for $0.25\,\mathrm{mm.s^{-1}}$, the smallest was noted in the case of $7\,\mathrm{mm.s^{-1}}$ model scenario. Furthermore, the magnitudes were the largest in the fringe region (Figure B.2b).

As the qualitative sediment deposition and erosion patterns across the for-

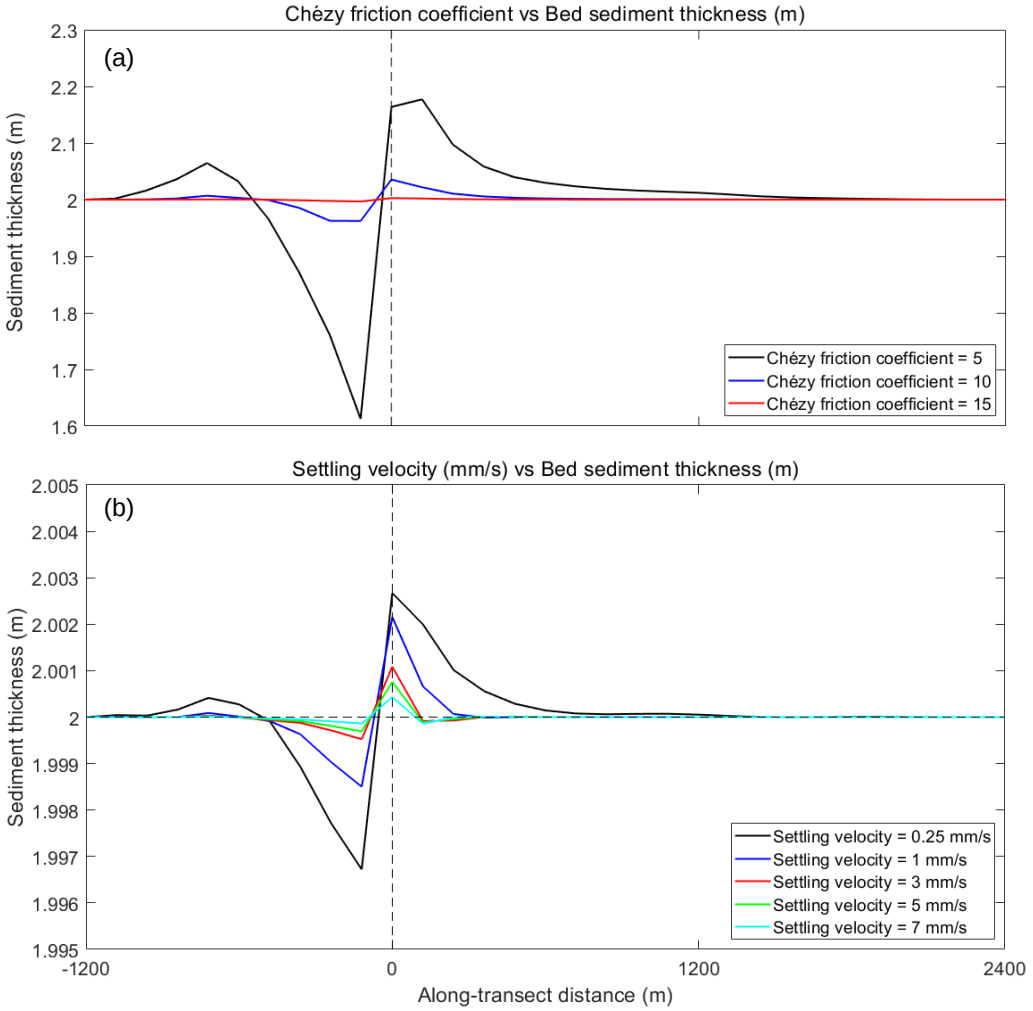

Figure B.2: Comparison of sediment deposition patterns across the forest for (a) varying Chézy bottom roughness coefficients and (b) settling velocities. $x = 0$ corresponds to the forest fringe transition zone in the vegetated model run.

est region do not change, the Chézy values and settling velocities were set to 15 and 0.01 mm.s^{-1}, respectively, based on literature values (Zhang et al., 2012; Mazda et al., 1997).

B.3 The influence of the initial bed sediment thickness

The implementation of morphology in Delft3D can be carried out using a uniformly well-mixed bed composition and a mixed bed stratigraphy (Lesser

et al., 2001). In the model simulations presented in this thesis, we used the uniformly well-mixed bed (without bed stratigraphy). In this approach, when sediment settles to the bed, the deposited sediment is assumed to uniformly integrate into bed sediment thickness, influencing the dominant contributors towards the total sediment fluxes noted in this thesis.

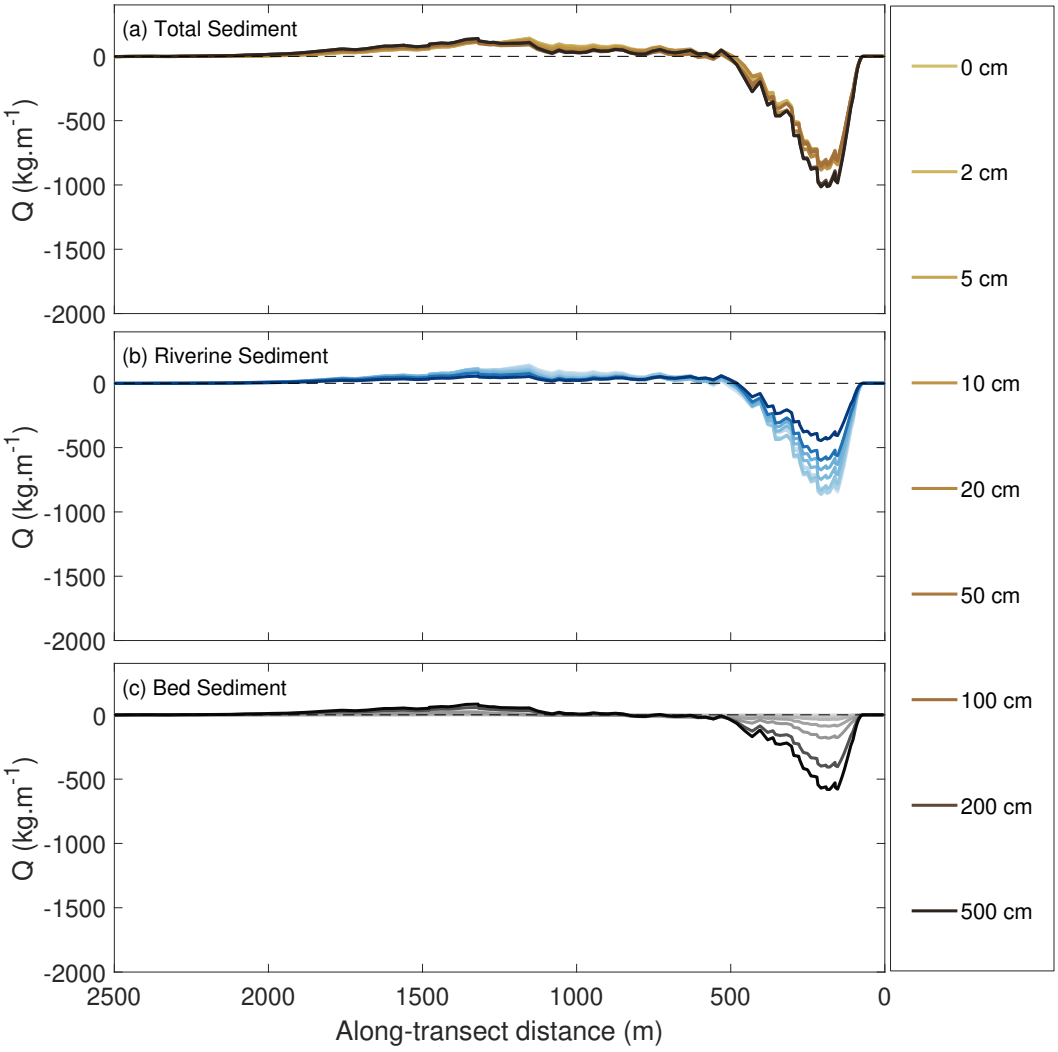

Figure B.3: Comparison of the tidal integrated across-transect (a) total sediment fluxes (brown lines), (b) riverine sediment fluxes (blue lines), and (c) bed-sourced sediment fluxes (black lines) for each of the discharge scenarios (Table 3.1, row 1) undertaken in the study. Colors show individual initial bed sediment thicknesses from low bed sediment thickness (lighter shades) to high bed sediment thickness (darker shades). In our evaluations, positive and negative fluxes indicate sediment transport out of the forest and into the forest region, respectively. Along-transect distance of $x = 0\,\mathrm{m}$ corresponds to river bank located inside the river mouth.

A sensitivity analysis was conducted to understand the influence of the initial bed sediment thickness on the overall total sediment fluxes across the eastern mangrove forest region with 175 $m^3.s^{-1}$ river discharge scenario. Using the model run with initial bed sediment thickness of 200 cm as the baseline, total, riverine, and bed-sediment fluxes were compared with model runs with initial bed sediment thickness of 2 cm, 5 cm, 10 cm, 20 cm, 50 cm, 100 cm, and 500 cm (Figure B.3). In the case of model runs with initial bed sediment thickness less than 200 cm, the riverine sediment concentrations were the dominant contributors towards the total sediment fluxes (Figure B.3b). On the other hand, for the model simulations with bed sediment thicknesses of 200 cm and 500 cm, the contribution of riverine sediment nearly halved, while the bed sediment contributions doubled (Figure B.3c). For model simulations conducted in this sensitivity analysis, total sediment transport did not show substantial differences (Figure B.3a).

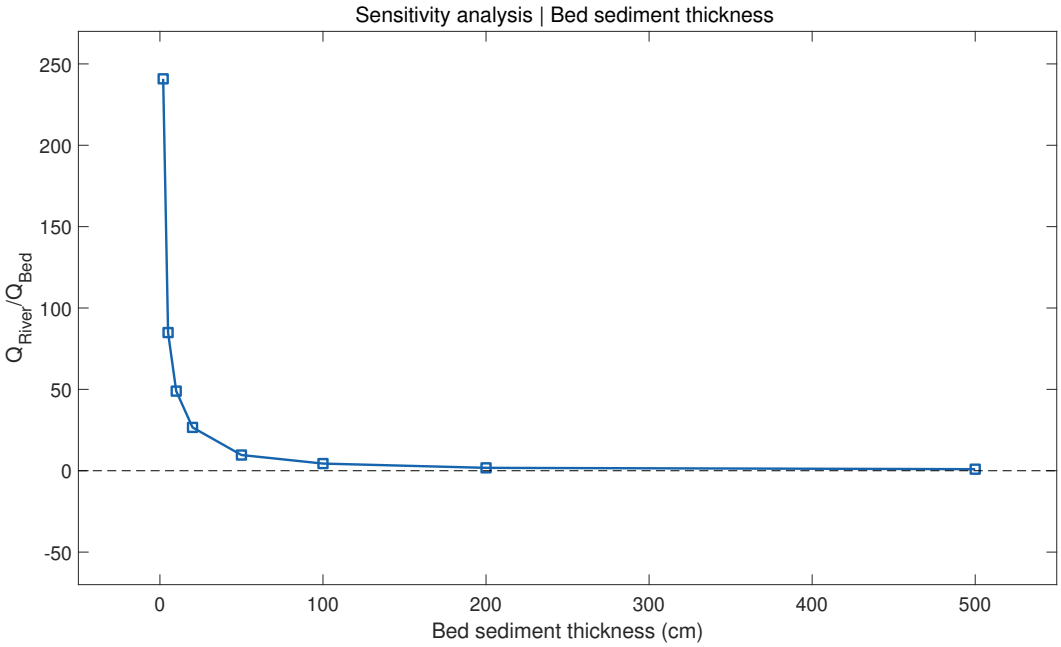

Figure B.4: Ratio of the tidally integrated riverine and bed sediment fluxes corresponding to $x = 250$ m in Figure B.3 plotted as a function of initial bed sediment thickness.

The ratio of riverine and bed sediment fluxes corresponding to the along-

transect distance of $x = 250\,\text{m}$ (Figure B.3) was plotted against varying initial bed sediment thickness used in this sensitivity analysis (Figure B.4). As expected, the ratios were found to be significantly high in the case of model simulations with initial bed sediment thickness up until 20 cm. However, for simulations with sizeable initial bed sediment thickness ($> 50\,\text{cm}$), the ratios nearly halved and substantially decreased as the sediment thickness was increased (Figure B.4).

While the total sediment fluxes (Figure B.3a) were similar for model scenarios with initial bed sediment thickness of 200 cm and 500 cm, the ratio of the riverine and bed-sourced sediment fluxes was found to be 1.775 and 0.9533, respectively (Figure B.4). While using a 200 cm initial bed sediment thickness in this modeling study is realistic in the real-world scenario, the uniform mixing throughout the bed layer is not. Thus, this representation of the mixing process leads to an underprediction of the relative contributions of riverine sediment to bed sediment, particularly in cases or locations where there are substantial amounts of deposition and resuspension of riverine sediments across the tidal cycle. However, given both riverine and bed-sourced sediment sediments have identical properties (e.g., specific density, fresh and saline settling velocities, bed shear, critical erosion and sedimentation thresholds), the total fluxes are not affected by the representation of sediment mixing in the bed layers.

References

Alekseenko, E. and B. Roux (2019). Contribution to remediation of brackish lagoon: 3D simulation of salinity, bottom currents, and resuspension of bottom sediments by strong winds. *Estuarine, Coastal and Shelf Science 216*, 27–37.

Allison, M. A., M. T. Ramirez, and E. A. Meselhe (2014). Diversion of Mississippi River water downstream of New Orleans, Louisiana, USA to maximize sediment capture and ameliorate coastal land loss. *Water resources management 28*(12), 4113–4126.

Alongi, D. M. (2002). Present state and future of the world's mangrove forests. *Environmental conservation 29*(3), 331–349.

Avicola, G. and P. Huq (2002). Scaling analysis for the interaction between a buoyant coastal current and the continental shelf: Experiments and observations. *Journal of physical oceanography 32*(11), 3233–3248.

Balke, T., E. L. Webb, E. van den Elzen, D. Galli, P. M. Herman, and T. J. Bouma (2013). Seedling establishment in a dynamic sedimentary environment: A conceptual framework using mangroves. *Journal of Applied Ecology 50*(3), 740–747.

Barbier, E. B., S. D. Hacker, C. Kennedy, E. W. Koch, A. C. Stier, and B. R. Silliman (2011). The value of estuarine and coastal ecosystem services. *Ecological Monographs 81*(2), 169–193.

Bates, C. C. (1953). Rational theory of delta formation. *Aapg Bulletin 37*(9), 2119–2162.

Boon III, J. D. and R. J. Byrne (1981). On basin hyposmetry and the morphodynamic response of coastal inlet systems. *Marine Geology 40*(1-2), 27–48.

Boothroyd, J. C. and D. K. Hubbard (1975). Genesis of bedforms in mesotidal estuaries. In *Geology and Engineering*, pp. 217–234. Elsevier.

Bouma, T. J., J. Van Belzen, T. Balke, Z. Zhu, L. Airoldi, A. J. Blight, A. J. Davies, C. Galvan, S. J. Hawkins, S. P. Hoggart, et al. (2014). Identifying knowledge gaps hampering application of intertidal habitats in coastal protection: Opportunities & steps to take. *Coastal Engineering 87*, 147–157.

Bowman, M. J. and S. M. Chiswell (1982). Numerical tidal simulations within the hauraki gulf, new zealand. In *Elsevier Oceanography Series*, Volume 34, pp. 349–384. Elsevier.

Brinkman, R. M., S. R. Massel, P. V. Ridd, K. Furukawa, et al. (1997). Surface wave attenuation in mangrove forests. In *Pacific Coasts and Ports'97. Proceedings*, Volume 2, pp. 941–946.

Brown, J. and A. Davies (2010). Flood/ebb tidal asymmetry in a shallow sandy estuary and the impact on net sand transport. *Geomorphology 114*(3), 431–439.

Bryan, K. R., W. Nardin, J. C. Mullarney, and S. Fagherazzi (2017). The role of cross-shore tidal dynamics in controlling intertidal sediment exchange in mangroves in Cù Lao Dung, Vietnam. *Continental Shelf Research 147*, 128–143.

Bullock, E. L., S. Fagherazzi, W. Nardin, P. Vo-Luong, P. Nguyen, and C. E. Woodcock (2017). Temporal patterns in species zonation in a mangrove forest in the Mekong Delta, Vietnam, using a time series of Landsat imagery. *Continental Shelf Research 147*, 144–154.

Carniello, L., A. D'Alpaos, and A. Defina (2011). Modeling wind waves and tidal flows in shallow micro-tidal basins. *Estuarine, Coastal and Shelf Science 92*(2), 263–276.

Chant, R. J., S. M. Glenn, E. Hunter, J. Kohut, R. F. Chen, R. W. Houghton, J. Bosch, and O. Schofield (2008). Bulge formation of a buoyant river outflow. *Journal of Geophysical Research: Oceans 113*(C1).

Chao, S.-Y. (1988a). River-forced estuarine plumes. *Journal of Physical Oceanography 18*(1), 72–88.

Chao, S.-Y. (1988b). Wind-driven motion of estuarine plumes. *Journal of Physical Oceanography 18*(8), 1144–1166.

Chao, S.-Y. (1990). Tidal modulation of estuarine plumes. *Journal of Physical Oceanography 20*(7), 1115–1123.

Chao, S.-Y. and W. C. Boicourt (1986). Onset of estuarine plumes. *Journal of Physical Oceanography 16*(12), 2137–2149.

Chatanantavet, P. and M. P. Lamb (2014). Sediment transport and topographic evolution of a coupled river and river plume system: An experimental and numerical study. *Journal of Geophysical Research: Earth Surface 119*(6), 1263–1282.

Chen, F., D. G. MacDonald, and R. D. Hetland (2009). Lateral spreading of a near-field river plume: Observations and numerical simulations. *Journal of Geophysical Research: Oceans 114*(C7).

Chen, Z., W. Gong, H. Cai, Y. Chen, and H. Zhang (2017). Dispersal of the Pearl River plume over continental shelf in summer. *Estuarine, Coastal and Shelf Science 194*, 252–262.

Chen, Z., A. Ortiz, L. Zong, and H. Nepf (2012). The wake structure behind a porous obstruction and its implications for deposition near a finite patch of emergent vegetation. *Water Resources Research 48*(9).

Cheng, P., A. Valle-Levinson, and H. E. De Swart (2010). Residual currents induced by asymmetric tidal mixing in weakly stratified narrow estuaries. *Journal of physical oceanography 40*(9), 2135–2147.

Choi, B.-J. and J. L. Wilkin (2007). The effect of wind on the dispersal of the Hudson River plume. *Journal of Physical Oceanography 37*(7), 1878–1897.

Cole, K. L. and R. D. Hetland (2016). The effects of rotation and river discharge on net mixing in small-mouth Kelvin number plumes. *Journal of Physical Oceanography 46*(5), 1421–1436.

Deltares (2017). User Manual Delft3D FLOW.

Deltares (2021). User Manual Delft3D FLOW.

Dronkers, J. (1986). Tidal asymmetry and estuarine morphology. *Netherlands Journal of Sea Research 20*(2-3), 117–131.

Duke, N. C., J.-O. Meynecke, S. Dittmann, A. M. Ellison, K. Anger, U. Berger, S. Cannicci, K. Diele, K. C. Ewel, C. D. Field, et al. (2007). A world without mangroves? *Science 317*(5834), 41–42.

Elias, E., D. Walstra, J. Roelvink, M. Stive, and M. Klein (2001). Hydrodynamic validation of Delft3D with field measurements at Egmond. In *Coastal Engineering 2000*, pp. 2714–2727.

Ellison, J. (2009). Geomorphology and sedimentology of mangroves.

Everard, M. and A. Powell (2002). Rivers as living systems. *Aquatic Conservation: Marine and Freshwater Ecosystems 12*(4), 329–337.

Fagherazzi, S., K. R. Bryan, and W. Nardin (2017). Buried alive or washed away: The challenging life of mangroves in the Mekong Delta. *Oceanography 30*(3), 48–59.

Fagherazzi, S., D. A. Edmonds, W. Nardin, N. Leonardi, A. Canestrelli, F. Falcini, D. J. Jerolmack, G. Mariotti, J. C. Rowland, and R. L. Slingerland

(2015). Dynamics of river mouth deposits. *Reviews of Geophysics 53*(3), 642–672.

Fong, D. A. and W. R. Geyer (2001). Response of a river plume during an upwelling favorable wind event. *Journal of Geophysical Research: Oceans 106*(C1), 1067–1084.

Fong, D. A. and W. R. Geyer (2002). The alongshore transport of freshwater in a surface-trapped river plume. *Journal of Physical Oceanography 32*(3), 957–972.

Fortunato, A. B. and A. Oliveira (2005). Influence of intertidal flats on tidal asymmetry. *Journal of Coastal Research*, 1062–1067.

Fricke, A., C. Nittrouer, A. Ogston, and H. Vo-Luong (2017). Asymmetric progradation of a coastal mangrove forest controlled by combined fluvial and marine influence, Cù Lao Dung, Vietnam. *Continental Shelf Research 147*, 78–90.

Friedrichs, C. T. (2011). Tidal flat morphodynamics: A synthesis.

Friedrichs, C. T. and D. G. Aubrey (1988). Non-linear tidal distortion in shallow well-mixed estuaries: A synthesis. *Estuarine, Coastal and Shelf Science 27*(5), 521–545.

Friedrichs, C. T. and D. G. Aubrey (1994). Tidal propagation in strongly convergent channels. *Journal of Geophysical Research: Oceans 99*(C2), 3321–3336.

Furukawa, K. and E. Wolanski (1996). Sedimentation in mangrove forests. *Mangroves and salt marshes 1*(1), 3–10.

García Berdeal, I., B. Hickey, and M. Kawase (2002). Influence of wind stress and ambient flow on a high discharge river plume. *Journal of Geophysical Research: Oceans 107*(C9), 13–1.

Garvine, R. W. (1995). A dynamical system for classifying buoyant coastal discharges. *Continental Shelf Research 15*(13), 1585–1596.

Garvine, R. W. and J. D. Monk (1974). Frontal structure of a river plume. *Journal of Geophysical Research 79*(15), 2251–2259.

Geyer, W. R., J. D. Woodruff, and P. Traykovski (2001). Sediment transport and trapping in the Hudson River estuary. *Estuaries 24*(5), 670–679.

Gijsman, R., E. M. Horstman, D. van der Wal, D. A. Friess, A. Swales, and K. M. Wijnberg (2021). Nature-based engineering: A review on reducing coastal flood risk with mangroves. *Frontiers in Marine Science 8*.

Gilman, E. L., J. Ellison, N. C. Duke, and C. Field (2008). Threats to mangroves from climate change and adaptation options: A review. *Aquatic botany 89*(2), 237–250.

Giri, C., E. Ochieng, L. L. Tieszen, Z. Zhu, A. Singh, T. Loveland, J. Masek, and N. Duke (2011). Status and distribution of mangrove forests of the world using earth observation satellite data. *Global Ecology and Biogeography 20*(1), 154–159.

Giri, C., Z. Zhu, L. Tieszen, A. Singh, S. Gillette, and J. Kelmelis (2008). Mangrove forest distributions and dynamics (1975–2005) of the tsunami-affected region of Asia. *Journal of Biogeography 35*(3), 519–528.

Gong, W., L. Chen, Z. Chen, and H. Zhang (2019). Plume-to-plume interactions in the Pearl River Delta in winter. *Ocean & Coastal Management 175*, 110–126.

Hallock, Z. and G. Marmorino (2002). Observations of the response of a buoyant estuarine plume to upwelling favorable winds. *Journal of Geophysical Research: Oceans 107*(C7), 3–1.

Healy, T. (2002). Chapter fourteen muddy coasts of mid-latitude oceanic

islands on an active plate margin—new zealand. In *Proceedings in Marine Science*, Volume 4, pp. 347–374. Elsevier.

Henderson, S. M., B. K. Norris, J. C. Mullarney, and K. R. Bryan (2017). Wave-frequency flows within a near-bed vegetation canopy. *Continental Shelf Research 147*, 91–101.

Hetland, R. D. (2005). Relating river plume structure to vertical mixing. *Journal of Physical Oceanography 35*(9), 1667–1688.

Hetland, R. D. (2010). The effects of mixing and spreading on density in near-field river plumes. *Dynamics of Atmospheres and Oceans 49*(1), 37–53.

Hibma, A., H. De Vriend, and M. Stive (2003). Numerical modelling of shoal pattern formation in well-mixed elongated estuaries. *Estuarine, Coastal and Shelf Science 57*(5-6), 981–991.

Hickey, B., L. J. Pietrafesa, D. A. Jay, and W. C. Boicourt (1998). The Columbia River plume study: Subtidal variability in the velocity and salinity fields. *Journal of Geophysical Research: Oceans 103*(C5), 10339–10368.

Hickey, B. M., R. M. Kudela, J. Nash, K. W. Bruland, W. T. Peterson, P. MacCready, E. J. Lessard, D. A. Jay, N. S. Banas, A. M. Baptista, et al. (2010). River influences on shelf ecosystems: Introduction and synthesis. *Journal of Geophysical Research: Oceans 115*(C2).

Hicks, D. M., U. Shankar, A. I. McKerchar, L. Basher, I. Lynn, M. Page, and M. Jessen (2011). Suspended sediment yields from new zealand rivers. *Journal of Hydrology (New Zealand) 50*(1), 81–142.

Hill, R. (2011). Sediment management in the waikato region, new zealand. *Journal of Hydrology (New Zealand)*, 227–239.

Horner-Devine, A. R. (2009). The bulge circulation in the Columbia River plume. *Continental Shelf Research 29*(1), 234–251.

Horner-Devine, A. R., R. D. Hetland, and D. G. MacDonald (2015). Mixing and transport in coastal river plumes. *Annual Review of Fluid Mechanics 47*, 569–594.

Horner-Devine, A. R., D. A. Jay, P. M. Orton, and E. Y. Spahn (2009). A conceptual model of the strongly tidal Columbia River plume. *Journal of Marine Systems 78*(3), 460–475.

Horstman, E., M. Dohmen-Janssen, and S. Hulscher (2013). Modeling tidal dynamics in a mangrove creek catchment in Delft3D. In *Coastal dynamics*, Volume 2013, pp. 833–844.

Horstman, E. M., C. M. Dohmen-Janssen, T. J. Bouma, and S. J. Hulscher (2015). Tidal-scale flow routing and sedimentation in mangrove forests: Combining field data and numerical modelling. *Geomorphology 228*, 244–262.

Horstman, E. M., C. J. Lundquist, K. R. Bryan, R. H. Bulmer, J. C. Mullarney, and D. J. Stokes (2018). The dynamics of expanding mangroves in New Zealand. In *Threats to Mangrove Forests*, pp. 23–51. Springer.

Houghton, R., C. Tilburg, R. Garvine, and A. Fong (2004). Delaware river plume response to a strong upwelling-favorable wind event. *Geophysical Research Letters 31*(7).

Hu, K., P. Ding, Z. Wang, and S. Yang (2009). A 2D/3D hydrodynamic and sediment transport model for the Yangtze Estuary, China. *Journal of Marine Systems 77*(1-2), 114–136.

Hunt, S., K. R. Bryan, J. C. Mullarney, and M. Pritchard (2016). Observations of asymmetry in contrasting wave-and tidally-dominated environments within a mesotidal basin: Implications for estuarine morphological evolution. *Earth Surface Processes and Landforms 41*(15), 2207–2222.

Iftekhar, M. and T. Takama (2008). Perceptions of biodiversity, environmental services, and conservation of planted mangroves: A case study on Nijhum Dwip Island, Bangladesh. *Wetlands Ecology and Management 16*(2), 119–137.

Ikeda, M. (1984). Coastal flows driven by a local density flux. *Journal of Geophysical Research: Oceans 89*(C5), 8008–8016.

Jickells, T. (1998). Nutrient biogeochemistry of the coastal zone. *Science 281*(5374), 217–222.

Jones, G. R., J. D. Nash, R. L. Doneker, and G. H. Jirka (2007). Buoyant surface discharges into water bodies. I: Flow classification and prediction methodology. *Journal of Hydraulic Engineering 133*(9), 1010–1020.

Kasai, A., A. E. Hill, T. Fujiwara, and J. H. Simpson (2000). Effect of the Earth's rotation on the circulation in regions of freshwater influence. *Journal of Geophysical Research: Oceans 105*(C7), 16961–16969.

Kilcher, L. F. and J. D. Nash (2010). Structure and dynamics of the Columbia River tidal plume front. *Journal of Geophysical Research: Oceans 115*(C5).

Kilcher, L. F., J. D. Nash, and J. N. Moum (2012). The role of turbulence stress divergence in decelerating a river plume. *Journal of Geophysical Research: Oceans 117*(C5).

Kothyari, U. C., K. Hayashi, and H. Hashimoto (2009). Drag coefficient of unsubmerged rigid vegetation stems in open channel flows. *Journal of Hydraulic Research 47*(6), 691–699.

Kourafalou, V. H., L.-Y. Oey, J. D. Wang, and T. N. Lee (1996). The fate of river discharge on the continental shelf: 1. Modeling the river plume and the inner shelf coastal current. *Journal of Geophysical Research: Oceans 101*(C2), 3415–3434.

Krauss, K. W., K. L. McKee, C. E. Lovelock, D. R. Cahoon, N. Saintilan, R. Reef, and L. Chen (2014). How mangrove forests adjust to rising sea level. *New Phytologist 202*(1), 19–34.

Kumara, M., L. Jayatissa, K. Krauss, D. Phillips, and M. Huxham (2010). High mangrove density enhances surface accretion, surface elevation change, and tree survival in coastal areas susceptible to sea-level rise. *Oecologia 164*(2), 545–553.

Lee, J. K., L. C. Roig, H. L. Jenter, and H. M. Visser (2004). Drag coefficients for modeling flow through emergent vegetation in the Florida Everglades. *Ecological Engineering 22*(4-5), 237–248.

Lentz, S. J. and D. C. Chapman (2004). The importance of nonlinear cross-shelf momentum flux during wind-driven coastal upwelling. *Journal of Physical Oceanography 34*(11), 2444–2457.

Leonardi, N., A. Canestrelli, T. Sun, and S. Fagherazzi (2013). Effect of tides on mouth bar morphology and hydrodynamics. *Journal of Geophysical Research: Oceans 118*(9), 4169–4183.

Leonardi, N., A. S. Kolker, and S. Fagherazzi (2015). Interplay between river discharge and tides in a delta distributary. *Advances in Water Resources 80*, 69–78.

Lesser, G., J. Van Kester, J. Roelvink, and G. Stelling (2001). Three-dimensional morphological modelling in Delft3D-FLOW. *Paper in prep*.

Lesser, G. R., J. v. Roelvink, J. T. M. van Kester, and G. Stelling (2004). Development and validation of a three-dimensional morphological model. *Coastal engineering 51*(8-9), 883–915.

Li, L., X. H. Wang, F. Andutta, and D. Williams (2014). Effects of mangroves and tidal flats on suspended-sediment dynamics: Observational and numer-

ical study of Darwin Harbour, Australia. *Journal of Geophysical Research: Oceans 119*(9), 5854–5873.

Lin, B. B. and J. Dushoff (2004). Mangrove filtration of anthropogenic nutrients in the Rio Coco Solo, Panama. *Management of Environmental Quality: An International Journal*.

López, F. and M. H. García (2001). Mean flow and turbulence structure of open-channel flow through non-emergent vegetation. *Journal of Hydraulic Engineering 127*(5), 392–402.

Lovelock, C. E., D. R. Cahoon, D. A. Friess, G. R. Guntenspergen, K. W. Krauss, R. Reef, K. Rogers, M. L. Saunders, F. Sidik, A. Swales, et al. (2015). The vulnerability of Indo-Pacific mangrove forests to sea-level rise. *Nature 526*(7574), 559–563.

Lovelock, C. E., B. K. Sorrell, N. Hancock, Q. Hua, and A. Swales (2010). Mangrove forest and soil development on a rapidly accreting shore in New Zealand. *Ecosystems 13*(3), 437–451.

Lovett, N. (2017). Sediment transport in the Firth of Thames mangrove forest, New Zealand (Thesis, Master of Science (MSc)). *MSc Thesis*.

MacDonald, D. G., L. Goodman, and R. D. Hetland (2007). Turbulent dissipation in a near-field river plume: A comparison of control volume and microstructure observations with a numerical model. *Journal of Geophysical Research: Oceans 112*(C7).

MacDonald, I. T. and J. C. Mullarney (2015). A novel "FlocDrifter" platform for observing flocculation and turbulence processes in a Lagrangian frame of reference. *Journal of Atmospheric and Oceanic Technology 32*(3), 547–561.

Marques, W., E. Fernandes, I. Monteiro, and O. Möller (2009). Numerical modeling of the Patos Lagoon coastal plume, Brazil. *Continental Shelf Research 29*(3), 556–571.

Marsaleix, P., C. Estournel, V. Kondrachoff, and R. Vehil (1998). A numerical study of the formation of the Rhône River plume. *Journal of Marine Systems 14*(1-2), 99–115.

Masse, A. K. and C. Murthy (1992). Analysis of the Niagara River plume dynamics. *Journal of Geophysical Research: Oceans 97*(C2), 2403–2420.

Mazda, Y., N. Kanazawa, and E. Wolanski (1995). Tidal asymmetry in mangrove creeks. *Hydrobiologia 295*(1), 51–58.

Mazda, Y., D. Kobashi, and S. Okada (2005). Tidal-scale hydrodynamics within mangrove swamps. *Wetlands Ecology and Management 13*(6), 647–655.

Mazda, Y., M. Magi, Y. Ikeda, T. Kurokawa, and T. Asano (2006). Wave reduction in a mangrove forest dominated by *Sonneratia* sp. *Wetlands Ecology and Management 14*(4), 365–378.

Mazda, Y. and E. Wolanski (2009). Hydrodynamics and modeling of water flow in mangrove areas. *Coastal wetlands: An integrated ecosystem approach 8*, 231–262.

Mazda, Y., E. Wolanski, B. King, A. Sase, D. Ohtsuka, and M. Magi (1997). Drag force due to vegetation in mangrove swamps. *Mangroves and salt marshes 1*(3), 193–199.

Mazda, Y., E. Wolanski, and P. Ridd (2007). *The role of physical processes in mangrove environments: Manual for the preservation and utilization of mangrove ecosystems*. Terrapub.

Mazzini, P. L. and R. J. Chant (2016). Two-dimensional circulation and mixing in the far field of a surface-advected river plume. *Journal of Geophysical Research: Oceans 121*(6), 3757–3776.

McCabe, R. M., P. MacCready, and B. M. Hickey (2009). Ebb-tide dynamics and spreading of a large river plume. *Journal of Physical Oceanography 39*(11), 2839–2856.

McIvor, A., I. Möller, T. Spencer, and M. Spalding (2012). Reduction of wind and swell waves by mangroves. *Natural Coastal Protection Series: Report 1. Cambridge Coastal Research Unit Working Paper 40. ISSN 2050-7941.*.

McIvor, A., I. Möller, T. Spencer, and M. Spalding (2013). Mangroves as a sustainable coastal defence. In *7th International Conference on Asian and Pacific Coasts (APAC). The Nature Conservancy, University of Cambridge, and Wetlands International, Bali, Indonesia, September*, pp. 24–26.

McKee, K. L. (2011). Biophysical controls on accretion and elevation change in Caribbean mangrove ecosystems. *Estuarine, Coastal and Shelf Science 91*(4), 475–483.

Mehta, A. J. and E. Partheniades (1982). Resuspension of deposited cohesive sediment beds. In *Coastal Engineering 1982*, pp. 1569–1588.

Mendes, R., M. C. Sousa, M. deCastro, M. Gómez-Gesteira, and J. M. Dias (2016). New insights into the Western Iberian Buoyant Plume: Interaction between the Douro and Minho River plumes under winter conditions. *Progress in Oceanography 141*, 30–43.

Mertes, L. A. and J. A. Warrick (2001). Measuring flood output from 110 coastal watersheds in California with field measurements and seawifs. *Geology 29*(7), 659–662.

Mestres, M., A. Sánchez-Arcilla, and J. Sierra (2010). Modeled dynamics of a small-scale river plume under different forcing conditions. *Journal of Coastal Research* (47), 84–96.

Montgomery, J. M., K. R. Bryan, E. M. Horstman, and J. C. Mullarney (2018).

Attenuation of tides and surges by mangroves: contrasting case studies from new zealand. *Water 10*(9), 1119.

Montgomery, J. M., K. R. Bryan, J. C. Mullarney, and E. M. Horstman (2019). Attenuation of storm surges by coastal mangroves. *Geophysical Research Letters 46*(5), 2680–2689.

Morris, R. L., T. M. Konlechner, M. Ghisalberti, and S. E. Swearer (2018). From grey to green: Efficacy of eco-engineering solutions for nature-based coastal defence. *Global change biology 24*(5), 1827–1842.

Mossa, M., M. B. Meftah, F. De Serio, and H. M. Nepf (2017). How vegetation in flows modifies the turbulent mixing and spreading of jets. *Scientific reports 7*(1), 6587.

Mullarney, J. C. and S. M. Henderson (2018). Flows within marine vegetation canopies. *Advances in Coastal Hydraulics*, 1–46.

Mullarney, J. C., S. M. Henderson, B. K. Norris, K. R. Bryan, A. T. Fricke, D. R. Sandwell, and D. P. Culling (2017). A question of scale: How turbulence around aerial roots shapes the seabed morphology in mangrove forests of the Mekong Delta. *Oceanography 30*(3), 34–47.

Mullarney, J. C., S. M. Henderson, J. A. Reyns, B. K. Norris, and K. R. Bryan (2017). Spatially varying drag within a wave-exposed mangrove forest and on the adjacent tidal flat. *Continental Shelf Research 147*, 102–113.

Münchow, A. and R. W. Garvine (1993). Buoyancy and wind forcing of a coastal current. *Journal of Marine Research 51*(2), 293–322.

Naish, T. R. (1990). *Late Holocene mud sedimentation and diagenesis in the Firth of Thames: Bentonites in the making.* Ph. D. thesis, University of Waikato.

Nepf, H. (2004). Vegetated flow dynamics. *The Ecogeomorphology of Tidal Marshes. American Geophysical Union, Washington, DC*, 137–163.

Nepf, H. M. (1999). Drag, turbulence, and diffusion in flow through emergent vegetation. *Water Resources Research 35*(2), 479–489.

Nepf, H. M. (2012a). Flow and transport in regions with aquatic vegetation. *Annual review of fluid mechanics 44*, 123–142.

Nepf, H. M. (2012b). Hydrodynamics of vegetated channels. *Journal of Hydraulic Research 50*(3), 262–279.

Nepf, H. M. and E. Vivoni (2000). Flow structure in depth-limited, vegetated flow. *Journal of Geophysical Research: Oceans 105*(C12), 28547–28557.

Nikiema, O., J.-L. Devenon, and M. Baklouti (2007). Numerical modeling of the Amazon River plume. *Continental Shelf Research 27*(7), 873–899.

Nittrouer, C. A. (1999). STRATAFORM: Overview of its design and synthesis of its results. *Marine Geology 154*(1-4), 3–12.

Nittrouer, C. A., G. J. Brunskill, and A. G. Figueiredo (1995). Importance of tropical coastal environments. *Geo-Marine Letters 15*(3-4), 121–126.

Norris, B. K., J. C. Mullarney, K. R. Bryan, and S. M. Henderson (2017). The effect of pneumatophore density on turbulence: A field study in a Sonneratia-dominated mangrove forest, Vietnam. *Continental Shelf Research 147*, 114–127.

Norris, B. K., J. C. Mullarney, K. R. Bryan, and S. M. Henderson (2019). Turbulence within natural mangrove pneumatophore canopies. *Journal of Geophysical Research: Oceans 124*(4), 2263–2288.

Norris, B. K., J. C. Mullarney, K. R. Bryan, and S. M. Henderson (2021). Relating millimeter-scale turbulence to meter-scale subtidal erosion and accretion across the fringe of a coastal mangrove forest. *Earth Surface Processes and Landforms 46*(3), 573–592.

Paola, C. (2000). Quantitative models of sedimentary basin filling. *Sedimentology 47*, 121–178.

Partheniades, E. (1965). Erosion and deposition of cohesive soils. *Journal of the Hydraulics Division 91*(1), 105–139.

Pethick, J. (1994). Estuaries and wetlands: Function and form. In *Wetland management: Proceedings of the international conference organized by Institution of Civil Engineers and held in London on 2–3 June 1994*, pp. 75–87. Thomas Telford Publishing.

Phan, L. K., J. S. van Thiel de Vries, and M. J. Stive (2015). Coastal mangrove squeeze in the Mekong Delta. *Journal of Coastal Research 31*(2), 233–243.

Postma, H. (1967). Sediment transport and sedimentation in the estuarine environment. *American Association of Advanced Sciences 83*, 158–179.

Pritchard, M. and D. A. Huntley (2006). A simplified energy and mixing budget for a small river plume discharge. *Journal of Geophysical Research: Oceans 111*(C3).

Pullen, J. D. and J. Allen (2000). Modeling studies of the coastal circulation off northern California: Shelf response to a major Eel River flood event. *Continental Shelf Research 20*(16), 2213–2238.

Rajaratnam, N. (1976). *Turbulent jets*. Elsevier.

Ren, J. and J. Wu (2014). Sediment trapping by haloclines of a river plume in the Pearl River Estuary. *Continental Shelf Research 82*, 1–8.

Richards, D. R. and D. A. Friess (2016). Rates and drivers of mangrove deforestation in Southeast Asia, 2000–2012. *Proceedings of the National Academy of Sciences 113*(2), 344–349.

Rickenmann, D. (1999). Empirical relationships for debris flows. *Natural hazards 19*(1), 47–77.

Rijnsburger, S., R. P. Flores, J. D. Pietrzak, A. R. Horner-Devine, and A. J. Souza (2018). The influence of tide and wind on the propagation of fronts

in a shallow river plume. *Journal of Geophysical Research: Oceans 123*(8), 5426–5442.

Roelvink, J. (2006). Coastal morphodynamic evolution techniques. *Coastal engineering 53*(2-3), 277–287.

Roelvink, J. and G. Van Banning (1995). Design and development of Delft3D and application to coastal morphodynamics. *Oceanographic Literature Review 11*(42), 925.

Rong, Z. and M. Li (2012). Tidal effects on the bulge region of Changjiang River plume. *Estuarine, Coastal and Shelf Science 97*, 149–160.

Roskoden, R. R., K. R. Bryan, I. Schreiber, and A. Kopf (2020). Rapid transition of sediment consolidation across an expanding mangrove fringe in the firth of thames new zealand. *Geo-Marine Letters 40*(2), 295–308.

Ruddick, K., E. Deleersnijder, T. Mulder, and P. Luyten (1994). A model study of the Rhine discharge front and downwelling circulation. *Tellus A 46*(2), 149–159.

Saenger, P. (2002). *Mangrove ecology, silviculture and conservation*. Springer Science & Business Media.

Saintilan, N., K. E. Kovalenko, G. Guntenspergen, K. Rogers, J. C. Lynch, D. R. Cahoon, C. E. Lovelock, D. A. Friess, E. Ashe, K. W. Krauss, et al. (2022). Constraints on the adjustment of tidal marshes to accelerating sea level rise. *Science 377*(6605), 523–527.

Schiller, R., V. Kourafalou, P. Hogan, and N. Walker (2011). The dynamics of the Mississippi River plume: Impact of topography, wind and offshore forcing on the fate of plume waters. *Journal of Geophysical Research: Oceans 116*(C6).

Schiller, R. V. and V. H. Kourafalou (2010). Modeling river plume dynamics

with the HYbrid Coordinate Ocean Model. *Ocean Modelling 33*(1-2), 101–117.

Sheaves, M., R. Baker, I. Nagelkerken, and R. M. Connolly (2015). True value of estuarine and coastal nurseries for fish: Incorporating complexity and dynamics. *Estuaries and Coasts 38*(2), 401–414.

Speer, P. E., D. G. Aubrey, and C. T. Friedrichs (1991). Nonlinear hydrodynamics of shallow tidal inlet/bay systems. *Tidal hydrodynamics*, 321–339.

Suzuki, T., M. Zijlema, B. Burger, M. C. Meijer, and S. Narayan (2012). Wave dissipation by vegetation with layer schematization in SWAN. *Coastal Engineering 59*(1), 64–71.

Swales, A., S. J. Bentley, C. Lovelock, and R. G. Bell (2007). Sediment processes and mangrove-habitat expansion on a rapidly-prograding muddy coast, new zealand. In *Coastal Sediments' 07*, pp. 1441–1454.

Swales, A., S. J. Bentley Sr, and C. E. Lovelock (2015). Mangrove-forest evolution in a sediment-rich estuarine system: opportunists or agents of geomorphic change? *Earth Surface Processes and Landforms 40*(12), 1672–1687.

Syvitski, J. P. (2003). Supply and flux of sediment along hydrological pathways: Research for the 21st century. *Global and Planetary Change 39*(1-2), 1–11.

Talke, S. A. and M. T. Stacey (2008). Suspended sediment fluxes at an intertidal flat: The shifting influence of wave, wind, tidal, and freshwater forcing. *Continental Shelf Research 28*(6), 710–725.

Temmerman, S., T. Bouma, J. Van de Koppel, D. Van der Wal, M. De Vries, and P. Herman (2007). Vegetation causes channel erosion in a tidal landscape. *Geology 35*(7), 631–634.

Temmerman, S., T. J. Bouma, G. Govers, Z. Wang, M. De Vries, and P. Herman (2005). Impact of vegetation on flow routing and sedimentation patterns: Three-dimensional modeling for a tidal marsh. *Journal of Geophysical Research: Earth Surface 110*(F4).

Temmerman, S., E. M. Horstman, K. W. Krauss, J. C. Mullarney, I. Pelckmans, and K. Schoutens (2023). Marshes and mangroves as nature-based coastal storm buffers. *Annual Review of Marine Science 15*.

Temmerman, S., P. Meire, T. J. Bouma, P. M. Herman, T. Ysebaert, and H. J. De Vriend (2013). Ecosystem-based coastal defence in the face of global change. *Nature 504*(7478), 79–83.

Thom, B. G. (1967). Mangrove ecology and deltaic geomorphology: Tabasco, Mexico. *The Journal of Ecology*, 301–343.

Trenberth, K. E., L. Smith, T. Qian, A. Dai, and J. Fasullo (2007). Estimates of the global water budget and its annual cycle using observational and model data. *Journal of Hydrometeorology 8*(4), 758–769.

Valiela, I., J. L. Bowen, and J. K. York (2001). Mangrove forests: One of the world's threatened major tropical environments: At least 35% of the area of mangrove forests has been lost in the past two decades, losses that exceed those for tropical rain forests and coral reefs, two other well-known threatened environments. *Bioscience 51*(10), 807–815.

Van Leeuwen, S. and H. De Swart (2002). Intermediate modelling of tidal inlet systems: Spatial asymmetries in flow and mean sediment transport. *Continental Shelf Research 22*(11-13), 1795–1810.

van Maanen, B., G. Coco, and K. R. Bryan (2013). Modelling the effects of tidal range and initial bathymetry on the morphological evolution of tidal embayments. *Geomorphology 191*, 23–34.

Van Maren, D. (2007). Water and sediment dynamics in the Red River mouth and adjacent coastal zone. *Journal of Asian Earth Sciences 29*(4), 508–522.

Vundavilli, H., J. C. Mullarney, and I. T. MacDonald (2022). The influence of river plume discharge and winds on sediment transport into a coastal mangrove environment. *Submitted to Estuaries and Coasts*.

Vundavilli, H., J. C. Mullarney, I. T. MacDonald, and K. R. Bryan (2021). The interaction of buoyant coastal river plumes with mangrove vegetation and consequences for sediment deposition and erosion in a tidal environment. *Continental Shelf Research 222*, 104417.

Walling, D. (2006). Human impact on land–ocean sediment transfer by the world's rivers. *Geomorphology 79*(3-4), 192–216.

Walsh, J. and C. Nittrouer (2004). Mangrove-bank sedimentation in a mesotidal environment with large sediment supply, Gulf of Papua. *Marine Geology 208*(2-4), 225–248.

Wang, Z., M. Jeuken, H. Gerritsen, H. De Vriend, and B. Kornman (2002). Morphology and asymmetry of the vertical tide in the Western Scheldt Estuary. *Continental Shelf Research 22*(17), 2599–2609.

Warrick, J. A., P. M. DiGiacomo, S. B. Weisberg, N. P. Nezlin, M. Mengel, B. H. Jones, J. C. Ohlmann, L. Washburn, E. J. Terrill, and K. L. Farnsworth (2007). River plume patterns and dynamics within the Southern California Bight. *Continental Shelf Research 27*(19), 2427–2448.

Warrick, J. A. and K. L. Farnsworth (2017). Coastal river plumes: Collisions and coalescence. *Progress in oceanography 151*, 245–260.

Warrick, J. A. and D. A. Fong (2004). Dispersal scaling from the world's rivers. *Geophysical Research Letters 31*(4).

Webster, J. G. (1995). Chemical processes affecting trace metal transport in

the waihou river and estuary, new zealand. *New Zealand Journal of Marine and Freshwater Research 29*(4), 539–553.

Wells, J. T. (1995). Tide-dominated estuaries and tidal rivers. In *Developments in sedimentology*, Volume 53, pp. 179–205. Elsevier.

Wells, M. G. (2009). How coriolis forces can limit the spatial extent of sediment deposition of a large-scale turbidity current. *Sedimentary Geology 218*(1-4), 1–5.

Whitney, M. M. and R. W. Garvine (2006). Simulating the Delaware Bay buoyant outflow: Comparison with observations. *Journal of Physical Oceanography 36*(1), 3–21.

Wolanski, E., M. Jones, and J. Bunt (1980). Hydrodynamics of a tidal creek-mangrove swamp system. *Marine and Freshwater Research 31*(4), 431–450.

Wolanski, E., Y. Mazda, P. Ridd, et al. (1992). Mangrove hydrodynamics. *Tropical Mangrove Ecosystems. Coastal and Estuarine Studies 41*.

Woodroffe, C. (1992). Mangrove sediments and geomorphology. In *Tropical Mangrove Ecosystems*, Volume 41, pp. 7–41. American Geophysical Union.

Woodroffe, C. D. (1990). The impact of sea-level rise on mangrove shorelines. *Progress in Physical Geography 14*(4), 483–520.

Woodroffe, C. D., K. Rogers, K. L. McKee, C. E. Lovelock, I. Mendelssohn, and N. Saintilan (2016). Mangrove sedimentation and response to relative sea-level rise. *Annual review of marine science 8*, 243–266.

Wright, L. (1977). Sediment transport and deposition at river mouths: A synthesis. *Geological Society of America Bulletin 88*(6), 857–868.

Wu, H., J. Zhu, J. Shen, and H. Wang (2011). Tidal modulation on the Changjiang River plume in summer. *Journal of Geophysical Research: Oceans 116*(C8).

Xuan, J., Z. Yang, D. Huang, T. Wang, and F. Zhou (2016). Tidal residual current and its role in the mean flow on the Changjiang Bank. *Journal of Marine Systems 154*, 66–81.

Yang, W. and S.-U. Choi (2010). A two-layer approach for depth-limited open-channel flows with submerged vegetation. *Journal of Hydraulic Research 48*(4), 466–475.

Yankovsky, A. E. and D. C. Chapman (1997). A simple theory for the fate of buoyant coastal discharges. *Journal of Physical Oceanography 27*(7), 1386–1401.

Yao, H., N. Leonardi, J. Li, and S. Fagherazzi (2016). Sediment transport in a surface-advected estuarine plume. *Continental Shelf Research 116*, 122–135.

Yuan, Y., A. R. Horner-Devine, M. Avener, and S. Bevan (2018). The role of periodically varying discharge on river plume structure and transport. *Continental Shelf Research 158*, 15–25.

Zhang, K., H. Liu, Y. Li, H. Xu, J. Shen, J. Rhome, and T. J. Smith III (2012). The role of mangroves in attenuating storm surges. *Estuarine, Coastal and Shelf Science 102*, 11–23.

Zhang, X., R. D. Hetland, M. Marta-Almeida, and S. F. DiMarco (2012). A numerical investigation of the Mississippi and Atchafalaya freshwater transport, filling and flushing times on the Texas-Louisiana Shelf. *Journal of Geophysical Research: Oceans 117*(C11).

Zhang, X., N. Leonardi, C. Donatelli, and S. Fagherazzi (2019). Fate of cohesive sediments in a marsh-dominated estuary. *Advances in Water Resources 125*, 32–40.

Zhou, Z., Q. Ye, and G. Coco (2016). A one-dimensional biomorphodynamic model of tidal flats: Sediment sorting, marsh distribution, and carbon accumulation under sea level rise. *Advances in water resources 93*, 288–302.

Zong, L. and H. Nepf (2010). Flow and deposition in and around a finite patch of vegetation. *Geomorphology 116*(3-4), 363–372.

Zong, L. and H. Nepf (2012). Vortex development behind a finite porous obstruction in a channel. *Journal of Fluid Mechanics 691*, 368–391.